

Accelerated Exploration of Empty Material Compositional Space: Mg–Fe–B Ternary Metal Borides

Zhen Zhang,[†] Shiya Chen,[†] Feng Zheng,[†] Vladimir Antropov, Yang Sun,* and Kai-Ming Ho



Cite This: <https://doi.org/10.1021/jacs.4c12648>



Read Online

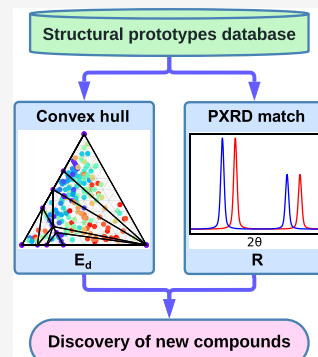
ACCESS |

Metrics & More

Article Recommendations

Supporting Information

ABSTRACT: Borides are a family of materials with valuable properties for various applications. Their diverse structures and compositions, yet disparity in the constituent chemical elements for the known compounds, give elemental substitutions for prototypes great potential for material discovery. To explore uncharted material compositional space, we develop a workflow that joins high-throughput crystal structure prediction and automated diffraction pattern matching to discover new compounds with significant prediction and synthesis hurdles. Utilizing the workflow, we explore the empty Mg–Fe–B ternary compositional space, previously uncharted largely due to the immiscibility of Mg and Fe, as a paradigm. A total of 275 ternary boride prototypes are classified, using which we predict 23 (158) stable and metastable ternary phases within 50 (200) meV/atom above the convex hull. We identify Gd₂(FeB)₇-type Mg₂Fe₇B₇ and ZrCo₃B₂-type MgFe₃B₂ to match previously unsolved experimental powder X-ray diffraction (PXRD) patterns. The discovered Mg₂Fe₇B₇ and related channeled structures feature mismatched Mg and (FeB) sublattice periods, for which we conduct structural analyses with respect to the PXRD. They are predicted to exhibit exceptionally fast superionic transport of Mg and outstanding electrochemical performance, which serve as post-Li-ion battery candidate electrode materials. This result opens a new avenue for borides' potential applications as electrode materials and fast ionic conductors. This work also portrays the map and landscape of ternary metal borides with similar chemical environments. With high efficiency, the prototype- and PXRD-assisted crystal structure prediction workflow opens a new avenue for exploring various material compositional spaces across the periodic table.



INTRODUCTION

In the contemporary landscape of materials chemistry, research focused on predicting and optimizing novel compounds through computational methods has gained increasing prominence. Borides, characterized by diverse structures, compositions, and outstanding properties, have attracted widespread attention among these materials. Boride systems not only form compounds with most metals but also exhibit a rich variety of atomic packings, encompassing isolated atoms, atomic pairs, various atomic chains, layered structures, three-dimensional (3D) grids, cage-like configurations, etc.¹ This structural diversity bestows upon borides extensive potential applications, spanning various domains such as magnetism,^{2–5} superconductivity,^{6–8} superhardness,^{9,10} electrochemistry,^{11–13} thermoelectricity,¹⁴ quantum effects,^{15,16} layered and two-dimensional (2D) materials.^{17,18}

Despite the abundance of borides with diverse structures, known borides show disparity in the constituent elements throughout the periodic table. For example, there are over 800 known RE-T-B phases,^{19,20} where RE is rare earth elements, and T is Group 4–12 transition metals. These RE-T-B compounds offer a variety of valuable applications, a crucial one being permanent magnets. For instance, Nd₂Fe₁₄B is one of today's best-performing permanent magnets.²¹ However, the mining difficulty, as well as the booming demand for RE, makes people spare no effort in searching for RE-free

magnets.^{5,22} One possible replacement of RE is Group 1–2 metal elements, A. In contrast to RE-T-B, there are scarce reports on A-T-B systems, most of which involve Ni.^{19,20,23,24} (Known compounds can be found in materials databases such as the Inorganic Crystal Structure Database (ICSD),²⁰ the Materials Project,²³ and the Open Quantum Materials Database (OQMD).²⁴) One of the works seeking new A-T-B systems is our previous predictive synthesis attempt of Mg–Fe–B ternary compounds.¹⁵ Yet, the predicted stable phase (YCrB₄-type (*Pbam* space group) MgFeB₄) has not been successfully synthesized, and the unknown phases observed¹⁵ have not been solved, making Mg–Fe–B borides elusive.

So far, no real-world Mg–Fe–B ternary compound is known. This is largely because Mg and Fe are a pair of mutually immiscible atoms in the solid or liquid state.²⁶ In the solid state, Mg and Fe do not form any binary compounds.^{20,23,24} Their binary alloys also exhibit limited solid intersolubility; for example, Mg was found to not dissolve in Fe

Received: September 11, 2024

Revised: November 10, 2024

Accepted: November 13, 2024

below 1000 °C. The immiscibility of Mg and Fe impedes the synthetic path from Mg–Fe binaries toward ternary compounds.¹⁵ On the other hand, if a third element can be introduced to stabilize a ternary compound containing an immiscible pair of elements, the immiscible elements are often separated or encapsulated by the third element, which leads to reduced dimensionalities such as one-dimensional (1D) and 2D structures.^{19,27,28} Then such a compound can offer promising candidacy for novel quantum materials,^{28,29} exfoliated layered materials,¹⁹ and intercalation-deintercalation battery materials. In particular, rechargeable Mg batteries are a promising post-Li-ion battery technology that attracts great interest. Mg is earth-abundant, cheap, and has a volumetric capacity (3830 mAh/mL) of more than four times that of graphite (anode of Li-ion batteries) and twice that of Li metal.³⁰

In light of these challenges and opportunities, a more in-depth investigation of the Mg–Fe–B system is motivated. This system serves as a paradigm for exploring empty material compositional space, especially those involving immiscible pairs of elements. It is one of the first few explored Ni-free A-T-B systems, which are rarely reported in contrast to the extensively studied RE-T-B systems. It can help demonstrate the hypothesis that A-T-B and RE-T-B systems show great structural similarities, i.e., largely isomorphic. Because *f*-electrons in RE do not significantly participate in chemical bonding, A and RE elements have very similar bonding environments in these ternary systems. Since previously unsolved experimental powder X-ray diffraction (PXRD) patterns are available, successfully solving them not only validates the theoretical methodology for accelerated materials discovery, but also leads to the discovery of new materials with potentially valuable properties.

In this work, we develop a computational workflow to facilitate materials discovery by bridging experimental data with structural prototypes. Comparing experimental PXRD patterns with simulated results of known structural types before further refinement is common among experimentalists. However, there is a lack of automated tools to speed up this process and sometimes even a lack of candidates with the correct structure. The potential of structural prototypes has not been sufficiently exploited from the following two perspectives. (1) Prevailing evolutionary structure prediction methods relying on first-principles calculations encounter difficulties for large primitive cells, e.g., more than 100 atoms, due to large or complex stoichiometries, superstructures, etc.³¹ In contrast, numerous prototypes with more than 100 atoms are measured by experiments. On the other hand, stable phases found after intensive structure search can be basic structural types. Trial prototypes in advance can be more straightforward and inexpensive. (2) The efficiency and great potential of PXRD solution using prototypes have been reported in a related work.³²

RESULTS AND DISCUSSION

Prototype- and PXRD-Assisted Crystal Structure Prediction Workflow.

Driven by these ideas, we implement a workflow combining crystal structure prediction using prototypes and high-throughput screening of PXRD data. High-throughput stability and property studies have frequently been conducted for other families of functional materials, such as oxides, but rather scarcely for borides. Also, previous studies often do high-throughput elemental substitutions for fixed one

or several prototypes. Here, instead, we do high-throughput prototype screening for a fixed ternary system. Computational details on the crystal structure prediction utilizing prototypes can be found in the Methods. Known 1466 ternary metal borides are classified into 275 structural prototypes, which are provided in Table S3 of the Supporting Information and serve as a boride prototypes database for this and future works. Figure 1 exhibits the convex hull of Mg–Fe–B obtained with

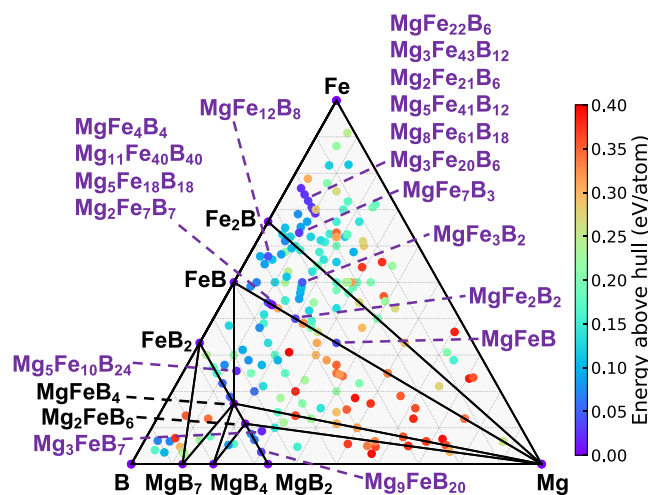


Figure 1. Convex hull ($T = 0$ K) of Mg–Fe–B. Black and purple labels indicate stable compounds and metastable compounds within 50 meV/atom above the convex hull, respectively.

these prototypes. We successfully capture two stable ternary phases, YCrB₄-type²⁵ (*Pbam* space group) MgFeB₄ and Y₂ReB₆-type³³ (*Pbam* space group) Mg₂FeB₆. The MgFeB₄ was previously identified as a stable phase coupled with Van Hove singularities (VHS).¹⁵ Thus, MgFeB₄ was selected for experimental synthesis.¹⁵ Further mutual validation between theory and experiment is crucial. As in the case of MgFeB₄, the experimental *in situ* PXRDs do not match the simulated one. The unsuccessful synthesis of a theoretically stable compound was likely to be caused by the complex interplay between thermodynamics and kinetics.^{34,35} It also reflects the challenges of synthesizing compounds containing elements with immiscibility and mismatched synthetic temperatures. More detailed discussions on these challenges and potential solutions for novel borides can be found in previous studies.^{15,19,36} Interestingly, using the hydride method (MgH₂ + Fe + B), two unknown Mg–Fe–B ternary phases were observed experimentally,¹⁵ which calls for the reexamination of other promising compounds.

The high-throughput screening calculations provide a comprehensive compositional space for ternary Mg–Fe–B compounds, as shown in Figure 1. The color of the dots manifests as the thermodynamic stability (E_d) of each stoichiometry. If more than one phase has the same stoichiometry, i.e., occupying the same position in the compositional space, then the one with the lowest E_d is shown. By using a threshold of 200 meV/atom³⁷ to filter unstable phases, we obtain a total of 158 stable and metastable phases. As a matter of fact, some ternary metal borides with a prediction of $E_d = 210$ meV/atom have been successfully synthesized.^{19,36} To select the most promising compounds suitable for synthesis, we subsequently consider a convex hull tolerance of $E_d < 50$ meV/atom as metastable phases,

Table 1. Mg–Fe–B Ternary Compounds within 50 meV/Atom above the Convex Hull

no.	E_d (meV/atom)	compounds	prototypes	references	space groups	number of atoms per primitive cell
1	0	MgFeB ₄	YCrB ₄	25	Pbam	24
2	0	Mg ₂ FeB ₆	Y ₂ ReB ₆	33	Pbam	36
3	8.4	MgFeB ₄	ThB ₄ Mo	41	Cmmm	12
4	10.8	Mg ₂ Fe ₇ B ₇	Gd ₃ (FeB) ₇	42	Pccn	128
5	15.6	Mg ₅ Fe ₁₈ B ₁₈	Nd ₅ (FeB) ₁₈	42–44	Pccn	164
6	17.2	Mg ₁₁ Fe ₄₀ B ₄₀	Sm ₁₁ (CoB) ₄₀	45	P $\bar{4}2_1$ c	182
7	18.6	Mg ₃ FeB ₇	Er ₃ CrB ₇	46	Cmcm	22
8	21.6	Mg ₅ Fe ₁₀ B ₂₄	U ₅ (B ₁₂ Mo ₅) ₂	47	Pmmm	78
9	22.5	MgFe ₂₂ B ₆	In(Ni ₁₁ B ₃) ₂	48	F $\bar{4}3$ m	29
10	24.0	Mg ₃ Fe ₂₀ B ₆	Ga ₃ (Ni ₁₀ B ₃) ₂	48	Fm $\bar{3}$ m	29
11	26.0	Mg ₃ Fe ₄₃ B ₁₂	Ni ₄₃ (GeB ₄) ₃	49 ⁽²³⁾	Fm $\bar{3}$ m (R3m)	(58)
12	26.8	Mg ₅ Fe ₄₁ B ₁₂	Al ₅ Ni ₄₁ B ₁₂	50 ⁽²³⁾	Fm $\bar{3}$ m (R3m)	(58)
13	27.8	MgFe ₂₂ B ₆	In(Ni ₁₁ B ₃) ₂	48	Fm $\bar{3}$ m	29
14	28.1	Mg ₈ Fe ₆₁ B ₁₈	Zr ₈ Ni ₆₁ B ₁₈	51,52 ⁽²³⁾	Fm $\bar{3}$ m (P $\bar{3}$ m1)	(87)
15	29.5	Mg ₂ Fe ₂₁ B ₆	Ga ₂ (Co ₇ B ₂) ₃	53	Fm $\bar{3}$ m	29
16	31.2	MgFe ₇ B ₃	ErNi ₇ B ₃	54	I4 ₁ /amd	44
17	33.8	Mg ₉ FeB ₂₀	LiMg ₉ B ₂₀	55 ⁽²³⁾	P6/mmm (P $\bar{1}$)	(30)
18	33.8	MgFe ₂ B ₂	Al(FeB) ₂	56	Cmmm	5
19	37.9	MgFe ₄ B ₄	Nd(CoB) ₄	57–60	P4 ₃ /n	18
20	38.4	MgFeB	TaNiB	61	Cmcm	6
21	44.3	MgFe ₁₂ B ₈	Al(Ni ₃ B ₂) ₄	62	Cmce	126
22	46.6	MgFe ₃ B ₂	MgNi ₃ B ₂	63,64	P6 ₄ 22	18
23	55.2	MgFe ₃ B ₂	ZrCo ₃ B ₂	65 ⁽⁶⁶⁾	R3 (R $\bar{3}$ m)	(18)

accounting for approximate temperature effects and errors arising from DFT functional. Any compound satisfying this condition is considered to have significant synthesis potential in experiments. A critical tolerance with comparable values for the convex hull has also been embraced in other high-throughput studies.^{38–40} This way, we obtain 23 phases (2 stable +21 metastable) with $E_d < 50$ meV/atom. These phases, their prototypes, E_d , and the number of atoms per primitive cell are listed in Table 1.

There are some notes regarding Table 1. ZrCo₃B₂-type^{65,66} MgFe₃B₂ with E_d slightly higher than 50 meV/atom is also shown since it matches the experimental PXRD, as will be discussed later. All prototypes' chemical formulas are in line with those listed in the computational database, the Materials Project.²³ The space group of each prototype and the corresponding references are also shown. For most of the prototypes, the space group listed in the Materials Project²³ is consistent with that reported in the original experimental papers. In this case, only one space group is given. There are a few prototypes (No. 11, 12, 14, and 17), for which two space groups are listed. Those outside the parentheses are reported by the original experimental papers as having partial occupancy for some sites. Those inside the parentheses are obtained from the Materials Project,²³ which applied techniques, e.g., to generate derivative structures with full occupancy usable for first-principles calculations. For ZrCo₃B₂, once the experimental structure,⁶⁵ R $\bar{3}$, is relaxed by DFT, a higher symmetry, R $\bar{3}$ m, can be obtained.⁶⁶ This computational structure is also adopted by the Materials Project.²³ For these cases, computational structures, i.e., those listed in the parentheses were used in our calculations. For MgNi₃B₂, an earlier study⁶⁴ reported a P6₄22 space group. The latest study⁶³ reported that the P6₄22 space group gave the best indexes for the measurements. Thus, the P6₄22 space group is in the computational database and was used in this work. For In(Ni₁₁B₃)₂, two structural models (Fm $\bar{3}$ m and F $\bar{4}3$ m) were discussed.⁴⁸ The number of atoms per

primitive cell corresponds to the cell used in the DFT calculations in this work.

To provide an accurate prediction for synthesis, combining experimental PXRD with theoretical crystal structure predictions, such as elemental substitutions for prototypes and evolutionary algorithms, is desired. However, this task is highly nontrivial, and the field of crystal structure prediction is only beginning to take into account realistic experimental conditions. Some recent work on high-throughput inorganic materials prediction and autonomous synthesis is attracting great attention.⁶⁸ The debate on the challenges⁶⁹ of the automated Rietveld refinement implemented⁶⁸ urges the development of related techniques. It is also of great interest and significance in developing experimental PXRD-assisted crystal structure prediction⁷⁰ to facilitate materials discovery. Therefore, we implement a high-throughput automated tool to match simulated PXRD with experimental ones in the Methods and obtain a list of the goodness of match factors, R. With E_d and R in hand, we determine the best-performing candidates for the discovered compounds. Since the E_d can be prepared and stored in a database and R does not involve first-principles quantum mechanical calculations, the workflow can be applied almost “on the fly” at the synchrotron or diffraction beamline.

To summarize our workflow, it mainly consists of three steps: (1) Classification of known structures and construction of prototypes database. (2) Elemental substitutions, DFT structural relaxations, DFT total energy calculations, and ternary convex hull construction. (3) PXRD pattern matching with consideration of thermal expansion within a reasonable value range. The workflow can be applied either before or after the exploratory synthesis and acts as a continuous feedback loop between theory and experiment. Existing powder analysis programs, such as Match!,⁷¹ are useful in pattern matching with known materials. These programs are only relevant to our step (3) in part. The novelty of our workflow lies in steps (1)

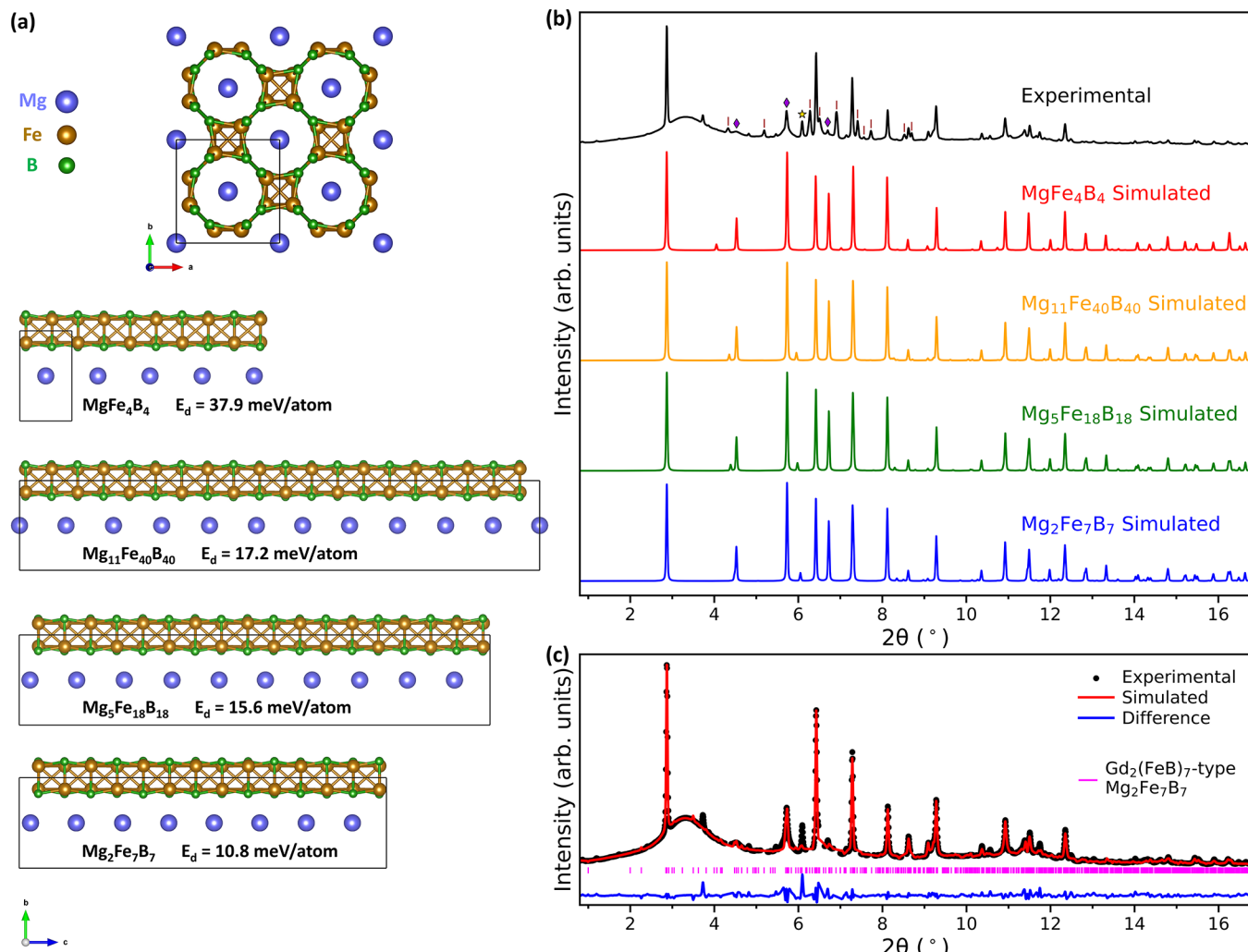


Figure 2. (a) Structures found to match the experimental PXRD ($\lambda = 0.2411 \text{ \AA}$) at $741 \text{ }^\circ\text{C}$.¹⁵ (b) Experimental (black) and simulated (colorful) PXRDs. Brown ticks label the measured peak tails of identified major phases at other temperature ranges. Purple diamonds label the measured peaks of which the strength is greatly reduced compared to the simulated ones due to the preferred orientation of the powder for these needle-like structures. Yellow star labels the measured peak that has offset from the simulated PXRDs. (c) Rietveld refinement for $\text{Gd}_2(\text{FeB})_7$ -type $\text{Mg}_2\text{Fe}_7\text{B}_7$. Fitting errors $wR_p = 0.0619$ and $R_p = 0.0406$, where wR_p and R_p are the weighted and unweighted profile R-factors, respectively.

and (2) and the consideration of thermal expansion in step (3). When studying a new ternary system, the construction of a high-quality database including DFT-optimized structures without omissions or redundancies, as performed in steps (1) and (2), is a prerequisite for successfully utilizing the pattern-matching functions in existing programs. Consideration of thermal expansion within a reasonable value range based on DFT-optimized structures, as performed in step (3), also guarantees the pattern matching is physical, which is especially important for analyzing *in situ* data collected at high temperatures. Moreover, the high-throughput PXRD pattern matching scheme can interface with not only the structure prediction by prototypes in this work, but also the other structure prediction methods by evolutionary algorithms, such as the genetic algorithm.^{31,72} This alternative PXRD-assisted crystal structure prediction method will be implemented in our future work.

Landscape of Mg–Fe–B Ternary Borides. According to Figure 1, phases in the Mg-rich region are high-energy and mostly unstable. Stable and metastable phases are distributed in approximately three regions: B-rich, B–Fe-intermediate, and

Fe-rich regions. Also, an interesting phenomenon is that low-energy phases tend to cluster along a specific path, i.e., a line segment in the compositional space. It implies a potential series of successful syntheses if managing to enter any of these paths.

The complete structural search allows us to examine the Mg–Fe–B phase regions in detail. In the B-rich region, the aforementioned two stable phases and other metastable phases reside along or near the FeB_2 – MgB_2 path. MgB_2 is a superconductor.^{6,7} Two metastable phases are situated along this path, Th B_4 Mo-type⁴¹ ($Cmmm$ space group) MgFeB_4 and Li Mg_9B_{20} -type^{23,55} ($P\bar{1}$ space group) $\text{Mg}_9\text{FeB}_{20}$. Like their MgB_2 endmember, these four low-energy ternary phases all have a layered structure consisting of alternating metal and boron layers. Calculations for YCr B_4 -type MgFeB_4 unveiled VHS resulting from the dimerization of Fe atoms.¹⁵ Such VHS can potentially induce various quantum states, rendering it a material of considerable interest.

The First Observed Ternary Phase. The B–Fe-intermediate region is occupied by metastable phases along or near the FeB – Mg path. An exemplified metastable phase

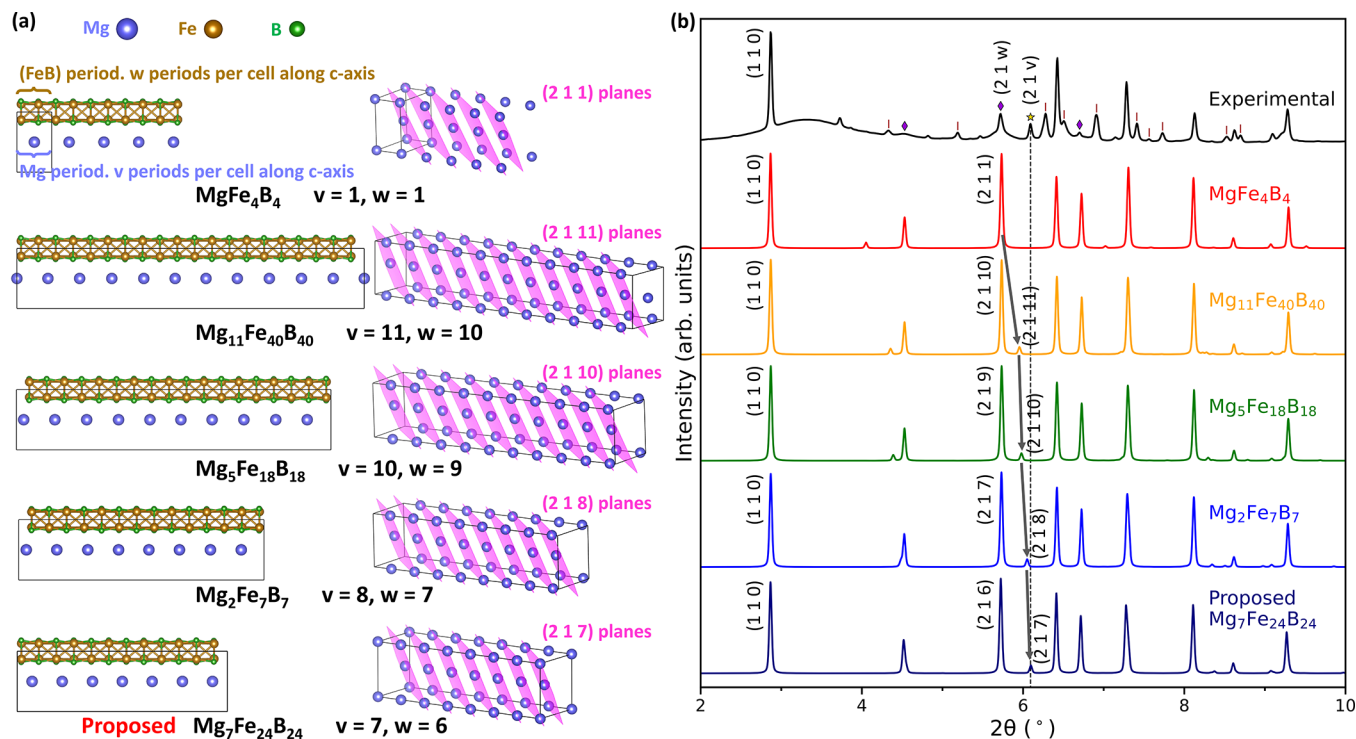


Figure 3. (a) Demonstration of the Mg repeat period and (FeB) repeat period along the c -axis for the series of $Mg_x(FeB)_4$ phases. v and w are the numbers of such periods along the c -axis per unit cell for Mg and (FeB), respectively. The right column shows the (2 1 v) lattice planes, the Bragg diffractions from which are due to the Mg atoms. The last row shows the proposed $P42_1c$ $Mg_7Fe_{24}B_{24}$ structural model. (2) The indexes of the first three strong peaks in the experimental PXRD,¹⁵ (1 1 0), (2 1 w), and the proposed (2 1 v).

along it is Nd(CoB)₄-type^{57–60} ($P4_2/n$ space group) $MgFe_4B_4$, which is depicted in Figure 2a. Fe and B atoms form a (FeB) backbone along the c -axis. Neighboring (FeB) backbones are connected with each other to form a (FeB) framework. Large hollow space through the (FeB) framework forms a channel along the c -axis. Within each channel, a single chain of Mg atoms takes form. Neighboring Mg chains are arranged in a face-centered square lattice in the c -axis projection.

Apart from $MgFe_4B_4$, there are also Sm₁₁(CoB)₄₀-type⁴⁵ ($P42_1c$ space group) $Mg_{11}Fe_{40}B_{40}$, Nd₅(FeB)₁₈-type^{42–44} ($Pccn$ space group) $Mg_5Fe_{18}B_{18}$, and Gd₂(FeB)₇-type⁴² ($Pccn$ space group) $Mg_2Fe_7B_7$ sharing great similarities with $MgFe_4B_4$. Stoichiometrically, they can all be denoted as $Mg_x(FeB)_4$ and are located very close to each other in the compositional space (Figure 1). Structurally, they are all commensurate superstructure variants of $MgFe_4B_4$, forming (FeB) backbones and Mg chains with mismatched sublattice periods along the c -axis (Figure 2a). Energetically, they are all low-energy metastable compounds with $E_d < 50$ meV/atom (Figure 2a). As more and more Mg atoms are intercalated into the Mg channels in the sequence of $MgFe_4B_4$, $Mg_{11}Fe_{40}B_{40}$, $Mg_5Fe_{18}B_{18}$, and $Mg_2Fe_7B_7$, their corresponding E_d decrease monotonically.

Notably, the simulated PXRDs of this series of structures match the best in our workflow one of the experimental PXRDs ($\lambda = 0.2411 \text{ \AA}$) at a characteristic temperature of 741 °C,¹⁵ which are displayed in Figure 2b. The degree of agreement is good enough to distinguish this series of phases from all other phases without ambiguity. Considering the E_d of these phases are all low and close to each other, any of them could be stabilized by temperature effects and exist. Since $Mg_2Fe_7B_7$ has the lowest E_d , 10.8 meV/atom, it is the most promising discovered compound among them. It is worth

mentioning that $Mg_{11}Fe_{40}B_{40}$, $Mg_5Fe_{18}B_{18}$, and $Mg_2Fe_7B_7$ all have more than 100 atoms per primitive cell. These uncommon stoichiometries and large primitive cells make prevailing structure prediction methods impractical to capture them.³¹

Since the crystals for this series of compounds are needle-like, their powder is very likely not to orient randomly. Thus, the preferred orientation of the powder explains the under-represented peaks labeled by purple diamonds in Figure 2b. So far, only one peak with significant intensity in the experimental PXRD has offset from the simulated PXRDs, which is labeled by the yellow star in Figure 2b. This peak is likely to be associated with the Mg–Mg distance along the chain of Mg atoms, as discussed later. $Mg_2Fe_7B_7$ yields the closest peak position to the experimental one. Therefore, both the E_d and diffraction pattern manifest $Mg_2Fe_7B_7$ as the most promising phase. Rietveld refinement for $Mg_2Fe_7B_7$ is exhibited in Figure 2c. The one-dimensionality of the (FeB) channel and Mg chain reaffirms our previous statement that materials containing immiscible elements often exhibit reduced dimensionalities.^{19,27,28} Furthermore, considering the relatively far distance from a Mg atom to another or the (FeB) framework, Mg is weakly bonded in the channel, and further intercalation of Mg is possible. The observed peak labeled by the yellow star might indicate further intercalation of Mg beyond $Mg_2Fe_7B_7$.

Before diving deeper into this issue, we note that this series of $Mg_x(FeB)_4$ phases resemble the Nowotny chimney ladder phases.⁷³ The latter phases are generally tetragonal and composed of two separate sublattices. The first is a tetragonal array of transition metal atoms, contained within which is a second array of main-group atoms. The mismatched periods

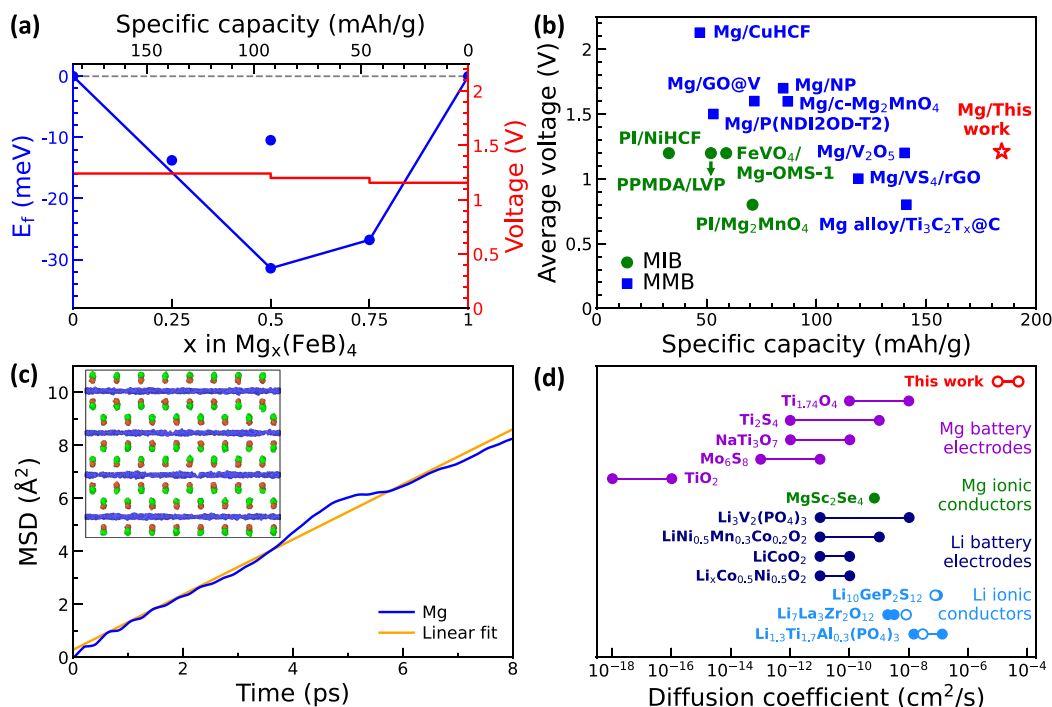


Figure 4. (a) Formation energy convex hull (blue) and voltage profile (red) for $Mg_x(FeB)_4$. (b) Electrochemical performance, including average voltage and specific capacity, compared to literature experimental values (discharge).^{74–85} MMB and MIB stand for Mg metal batteries and Mg-ion batteries, respectively. (c) Mean square displacement (MSD) of Mg in the AIMD simulations for the 288-atom $MgFe_4B_4$ at 300 K (blue) and its linear fit (orange). Insert: trajectories of atoms (Mg, Fe, and B in blue, brown, and green, respectively) viewed along the direction perpendicular to the 1D channel. (d) Diffusion coefficient compared to literature values at room temperature for Mg and Li battery electrode^{86–94} and ionic conductor^{95–104} materials. Solid symbols represent experimental values, and hollow symbols represent computational values by AIMD.

between the two arrays of atoms can form large commensurate superstructures or even incommensurate phases. The stoichiometric ratio and the c lattice constant ratio of the two sublattices are rational (irrational) numbers for a commensurate (incommensurate) structure. Here, the $Mg_x(FeB)_4$ phases show some similarities. $Mg_x(FeB)_4$ phases are tetragonal or tetragonal-like. $P4_2/n$ $MgFe_4B_4$ and $\bar{P}4_21c$ $Mg_{11}Fe_{40}B_{40}$ are tetragonal. Although $Pccn$ $Mg_3Fe_{18}B_{18}$ and $Mg_2Fe_7B_7$ are orthorhombic, their a and b are numerically degenerate within negligible errors from DFT optimizations. A chain of Mg atoms is contained within the (FeB) channel walls. A previous study detailed two methods, commensurate and incommensurate refinements, to solve for the main-group to transition metal atoms stoichiometric ratio and lattice constants from the PXRD for the Nowotny chimney ladder phases.⁷³ In the same spirit, we used a similar and simpler method to address this issue for the $Mg_x(FeB)_4$ phases.

We demonstrate the repeating periods of Mg atoms and (FeB) channel walls along the c -axis in Figure 3a. Then, we define the number of periods per unit cell along the c -axis as v and w for Mg and (FeB), respectively. By this definition, the chemical formula before simplification is $Mg_{2v}(FeB)_{8w}$ per unit cell for these phases. The indexes of the first three strong peaks in the experimental PXRD are demonstrated in Figure 3b. By comparison with the four phases' simulated PXRDs, the first two experimental peaks are readily indexed by (1 1 0) and (2 1 w). The (2 1 w) peak is caused by the diffraction from the (FeB) sublattice. The peak labeled by the yellow star can be attributed to the (2 1 v) peak, which results from diffraction from the Mg sublattice. As the Mg content increases, this peak gets closer and closer to the observed peak, which strengthens our confidence in it. The (2 1 v) lattice planes formed by Mg

atoms, which cause such reflections, are displayed in Figure 3a. For $MgFe_4B_4$ with matched Mg and (FeB) sublattices, $v = 1$ and $w = 1$. Correspondingly, the (2 1 w) and (2 1 v) peaks overlap with each other. The rest three phases, $Mg_{11}Fe_{40}B_{40}$ ($v = 11$, $w = 10$), $Mg_3Fe_{18}B_{18}$ ($v = 10$, $w = 9$), and $Mg_2Fe_7B_7$ ($v = 8$, $w = 7$) have mismatched sublattices. The mismatched Mg and (FeB) sublattices with different lattice plane distances diffract X-ray differently. Thus, the (2 1 v) peak splits from the (2 1 w) peak.

Here, we solve for the Mg to (FeB) stoichiometric ratio from the first three strong experimental peaks, (1 1 0), (2 1 w), and (2 1 v). The rest of the peaks serve as a verification for our solution. (Note that no other strong peak is associated with the Mg–Mg distance and is usable for solving for v .) According to Bragg's law, a ($= b$) can be obtained from the (1 1 0) peak position. Next, w/c and v/c can be obtained from the (2 1 w) and (2 1 v) peak positions, respectively. Then, $v/w = (v/c)/(w/c)$. This way, the incommensurate Mg to (FeB) stoichiometric ratio is accurately determined as $[Mg]/[(FeB)] = (2v)/(2w) = 0.2915$. By restricting the numerators and denominators of rational numbers to integers within 100, the approximate commensurate ratio is $7/24 = 0.2917$. Based on this commensurate ratio, we propose a $Mg_7Fe_{24}B_{24}$ stoichiometry, for which $v = 7$, $w = 6$. To further confirm it, we construct a structural model based on the same space group for $Mg_{11}Fe_{40}B_{40}$, $\bar{P}4_21c$. We note that when v is an odd number, it is practical to use the $\bar{P}4_21c$ space group; when v is an even number, it is practical to use the $Pccn$ space group (the one for $Mg_3Fe_{18}B_{18}$ and $Mg_2Fe_7B_7$). After DFT structural relaxation, we surprisingly find out the E_d of the proposed $Mg_7Fe_{24}B_{24}$ is merely 8.7 meV/atom, which is slightly smaller than that of $Mg_2Fe_7B_7$, 10.8 meV/atom. This further

corroborates our previous hypothesis that more Mg can be intercalated beyond $Mg_2Fe_7B_7$. The simulated PXRD pattern for $Mg_7Fe_{24}B_{24}$ is shown in Figure 3b, which matches the observed peak labeled by the yellow star. To facilitate future refinement with respect to the experimental data, the proposed structural model is provided in Table S1 of the Supporting Information.

Note that the proposed new structural model does not invalidate our workflow or the old structural model of $Gd_2(FeB)_7$ -type $Mg_2Fe_7B_7$. For $Mg_2Fe_7B_7$, $[Mg]/[(FeB)] = 0.2857$, which is close to that solved from the PXRD, 0.2915. Energies of $Mg_2Fe_7B_7$ and $Mg_7Fe_{24}B_{24}$ also only differ by ~ 2 meV/atom. It is using the workflow that this little-known series of superstructures with mismatched sublattices is uncovered. Based on the old models, the new model is proposed by analyzing the experimental data, which is the typical process for discovering a new material. Both models are useful for refinements with respect to future higher-quality experimental data. This study brings this series of phases to attention and provides insights for similar analyses in the future.

Considering the limited resolution of the available PXRD for superstructures or incommensurate structures, images showing satellite reflections are desired to distinguish different structures more clearly and finally determine the experimentally observed structure. Thus, we also simulate the single-crystal diffraction and exhibit the diffraction patterns for view directions along [001], [100], and [110] in Figures S1, S2, and S3 of the Supporting Information, respectively. When viewing along [100] and [110] directions, satellite reflections are observable for $Mg_{11}Fe_{40}B_{40}$, $Mg_5Fe_{18}B_{18}$, and $Mg_2Fe_7B_7$, which correspond to the mismatched sublattice periods between Mg and (FeB) along the *c*-axis. In contrast, $MgFe_4B_4$, which has matched sublattices, does not show satellite reflections. The difference in the diffraction patterns among these four phases is discernible, as compared in Figure S4 of the Supporting Information. We hope these simulations will be useful for comparison with and analysis of future experimental measurements.

Seeking novel electrode materials is crucial in improving battery performance for the next-generation Mg batteries. The 1D intercalation-deintercalation mechanism of Mg in the (FeB) channel enables possibly good electrochemical performance and fast ionic transport. To check this, voltage vs Mg/Mg²⁺ is derived from the formation energy convex hull calculations for the Mg-deintercalated $Mg_x(FeB)_4$, which is shown in Figure 4a. The $MgFe_4B_4$ cell is used since the other three stoichiometries have over 100 atoms per primitive cell, making simulations impractical. It exhibits a flat voltage platform with an average value of 1.2 V, a typical voltage for Mg batteries, which is compared to literature discharge values for both Mg metal batteries (MMB) and Mg-ion batteries (MIB) in Figure 4b.^{74–85} Mg batteries generally have lower voltage than Li-ion batteries due to the divalent nature of Mg. Notably, $MgFe_4B_4$ has an outstanding specific capacity, 184 mAh/g, which is greater than most known literature values. Note that such theoretical capacity is expected to be close to the realistic value since, as suggested by experimental observations, further intercalation of Mg beyond $MgFe_4B_4$ is feasible. We estimate feasible upper limits for Mg intercalation, $Mg_{1.5}Fe_4B_4$ ($E_d = 25$ meV/atom), and the corresponding theoretical capacity, 265 mAh/g, for this series of compounds.

Their ionic dynamics are studied by *ab initio* molecular dynamics (AIMD) at room temperature. While the (FeB)

framework maintains a periodic crystalline lattice, the Mg exhibits a 1D superionic behavior in the channel (insert of Figure 4c), leading to large ionic mobility along that direction. The diffusion coefficient (*D*) of Mg is obtained by the linear fitting of its mean square displacement (MSD) and is shown in Figure 4c. Typical literature values for *D* of Mg and Li battery materials are $< 10^{-8}$ cm²/s, which are summarized in Figure 4d.^{86–94} The spreading *D* value is believed to be due to electrostatic repulsion; the higher the intercalated atom's concentration in the host lattice, the lower the diffusivity.⁸⁶ Remarkably, *D* of $Mg_x(FeB)_4$ is 5×10^{-5} to 1×10^{-5} cm²/s, evaluated from the stoichiometrically constraining $MgFe_4B_4$ and $Mg_2Fe_7B_7$, respectively. Therefore, $Mg_x(FeB)_4$ has an exceptionally high *D*, which is at least 3 orders of magnitude higher than typical electrode values, making it a crystalline fast ionic conductor⁹⁵ of Mg, $\sigma = 14$ to 3 S/cm. The outstanding electrochemical performance and ionic transport property, as well as the metallic nature of $Mg_x(FeB)_4$, make it a promising cathode material for Mg batteries. On the other hand, the metallic nature of this material suggests it might not be suitable for solid-state electrolytes, which require predominant ionic conduction and negligible electronic conduction. Nevertheless, it serves as a candidate superionic conductor material with the 1D diffusion chain/channel⁹⁵ for study.

Diffusion is a complex behavior involving concerted motions of atoms, and AIMD is the most appropriate computational method for obtaining *D*. However, due to relatively slow diffusion in conventional electrodes at room temperature, long simulation time and large simulation scale are required to sufficiently capture the diffusion events, which are impractical for AIMD based on current computational capability. Nevertheless, it is prevailing to use AIMD to study materials with relatively fast diffusion, e.g., ionic conductors.^{95,96} Ionic conductors suitable for solid-state electrolytes differ from electrodes mainly due to their insignificant electronic conductivity. To demonstrate the validity of AIMD in predicting *D*, literature values for *D* of Mg and Li ionic conductor materials at room temperature are also summarized in Figure 4d.^{96–104} Available *D* values obtained by AIMD⁹⁶ for commonly seen Li ionic conductors, such as $Li_{10}Ge_2S_{12}$ (LGPS), $Li_7La_3Zr_2O_{12}$ (LLZO), and $Li_{1.3}Ti_{1.7}Al_{0.3}(PO_4)_3$ (LATP), are all in good agreement with experimental ones.^{98–104} For the $Mg_x(FeB)_4$ system studied here, the visible superionic behavior and high *D* value indicate the use of AIMD for studying diffusion is appropriate.

Moreover, some implications for this channeled structure can be made based on this work. Mg may be replaced by other Group 1–2 elements to study other types of battery materials. Fe may be replaced by other transition metals to tune the channel capacity and the intercalated atoms' diffusivity. The rich known materials inventory of this structure containing rare earths (see Table S2 of the Supporting Information) may also be used to study the diffusion, capture/release, and recycle/purification of rare earths.

The series of $Mg_x(FeB)_4$ phases also have apparent uniaxial symmetry, which is the structural fundament of large magnetic anisotropy. However, calculations show magnetic moment to be, on average, merely 0.86 μ_B /Fe for $MgFe_4B_4$, $Mg_{11}Fe_{40}B_{40}$, 0.82 μ_B /Fe for $Mg_5Fe_{18}B_{18}$ and $Mg_2Fe_7B_7$, which is relatively small for ideal permanent magnets. Another metastable phase residing on the FeB-Mg path worth mentioning is Al(FeB)₂-type⁵⁶ (*Cmmm* space group) $MgFe_2B_2$, which has a moment of 0.99 μ_B /Fe. $MgFe_2B_2$ does not take a similar form to the

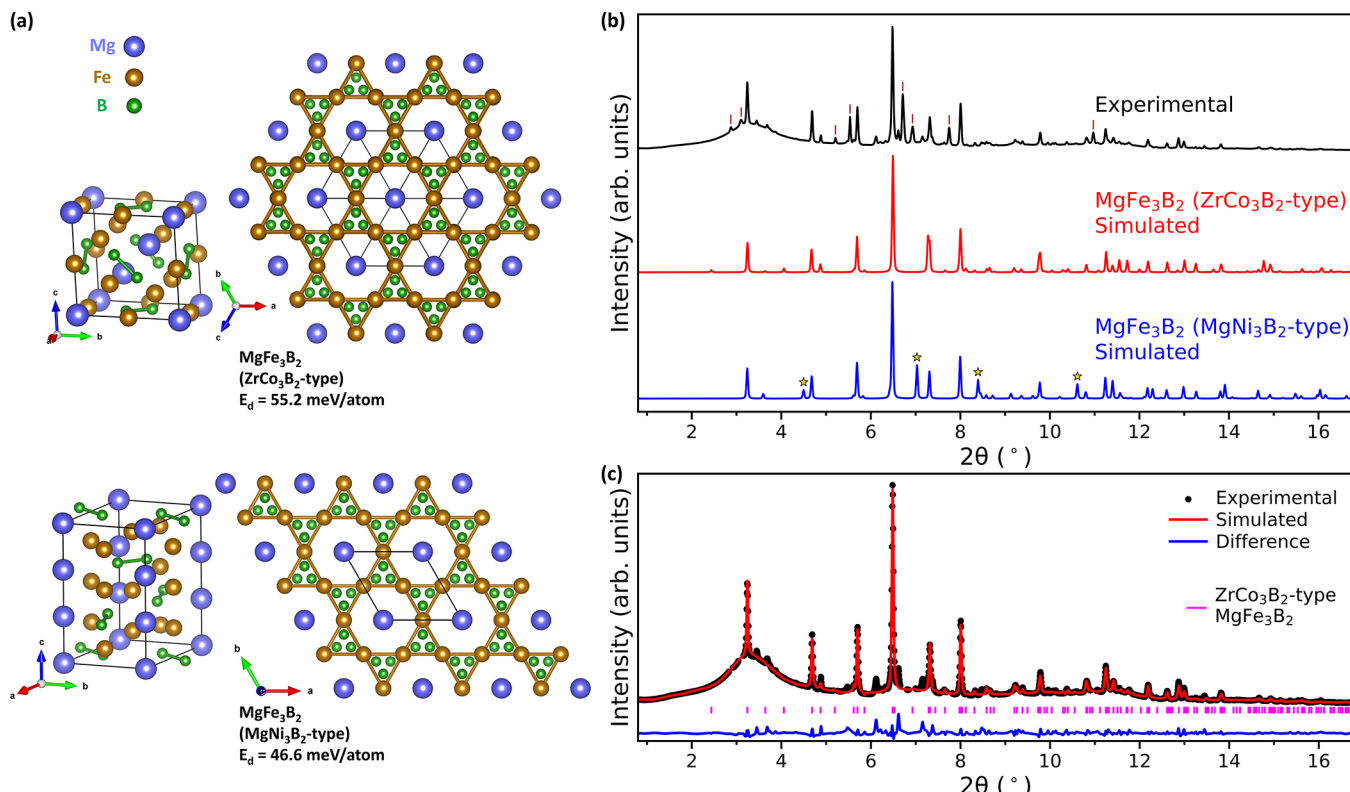


Figure 5. (a) Structures found to match the experimental PXRD ($\lambda = 0.2411 \text{ \AA}$) at 621°C .¹⁵ (b) Experimental (black) and simulated (colorful) PXRDs. Brown ticks label the measured peak tails of identified major phases at other temperature ranges. Yellow stars label the simulated peaks that do not show in the measured PXRD. (c) Rietveld refinement for ZrCo_3B_2 -type MgFe_3B_2 . Fitting errors $wR_p = 0.0604$ and $R_p = 0.0377$, where wR_p and R_p are the weighted and unweighted profile R-factors, respectively.

previous $\text{Mg}_x(\text{FeB})_4$. $\text{Al}(\text{FeB})_2$ is known to have a magneto-caloric effect.⁵⁶ The magnetic and chemically similar MgFe_2B_2 is also expected to have similar properties.

The Second Observed Ternary Phase. Another metastable phase in the B–Fe-intermediate region is MgFe_3B_2 (Figure 1), which is off the FeB–Mg path. There are two low-energy MgFe_3B_2 phases, ZrCo_3B_2 -type^{65,66} ($\bar{R}\bar{3}m$ space group) and MgNi_3B_2 -type^{63,64} ($P\bar{6}_4\bar{2}2$ space group). ZrCo_3B_2 -type MgFe_3B_2 has a slightly higher E_d , 55.2 meV/atom , than that of MgNi_3B_2 -type MgFe_3B_2 , 46.6 meV/atom . Note that there are four other types of MgFe_3B_2 : ZnNi_3B_2 -type¹⁰⁵ ($C\bar{1}2/m\bar{1}$ space group) with $E_d = 66.0 \text{ meV/atom}$, CeCo_3B_2 -type¹⁰⁶ ($P\bar{6}/mmm$ space group) with $E_d = 117.6 \text{ meV/atom}$, CrFe_3B_2 -type²³ (only computational $Fmm2$ space group is available) with $E_d = 199.2 \text{ meV/atom}$, and MnRe_3B_2 -type^{23,107} (experimental $Fddd$ and computational $F2\bar{2}2$ space groups) with $E_d = 230.4 \text{ meV/atom}$. These phases are not considered here due to their higher energies and mismatched PXRDs. The ZrCo_3B_2 -type structure has a rhombohedral primitive cell, while the MgNi_3B_2 -type structure has a hexagonal one, both of which contain 18 atoms, as shown in Figure 5a. Projections along the rhombohedral [111] and hexagonal c -axis, respectively, reveal great similarity between them. Both of them consist of alternating MgB_2 layers and Fe layers. Each Fe layer forms a rumpled Kagome lattice. The difference between the two structures is the arrangement of Mg atoms and B dimers within a MgB_2 layer.⁶³

These two MgFe_3B_2 phases also distinguish themselves from the rest of the structures without ambiguity for generating PXRDs in good agreement with one of the experimental

PXRDs at a characteristic temperature of 621°C ,¹⁵ which are displayed in Figure 5b. The ZrCo_3B_2 -type MgFe_3B_2 has calculated PXRD in excellent agreement with the experimental one. In contrast, although MgNi_3B_2 -type MgFe_3B_2 has calculated PXRD in general agreement with the measurement, its peaks labeled by yellow stars in Figure 5b do not appear in the experimental PXRD. Hence, despite having a slightly higher E_d , the ZrCo_3B_2 -type structure is expected to be stabilized by thermodynamics or correction for DFT errors and adopted by MgFe_3B_2 instead of the MgNi_3B_2 -type structure. Rietveld refinement for ZrCo_3B_2 -type MgFe_3B_2 is exhibited in Figure 5c.

Kagome lattice is a fascinating 2D network where many exotic quantum phenomena are expected.¹⁰⁸ Here, a closer examination of the Fe Kagome lattice in both types of MgFe_3B_2 indicates the Fe layers are not sufficiently separated by the MgB_2 layer, resulting in roughly the same out-of-plane and in-plane Fe–Fe bond lengths. The Fe network is thereby 3D and can be categorized as a linked Kagome lattice.¹⁰⁹ Their corresponding Kagome electronic bands are distorted by strong interlayer interactions, and typical 2D Kagome properties such as Dirac cone and flat band do not exist in these phases. Nevertheless, the seeming two-dimensionality here once again echoes that immiscible elements can potentially induce reduced dimensionalities.^{19,27,28} Calculations show magnetic moment to be 1.48 (1.55) μ_B/Fe for $2/3$ of the Fe atoms and 2.13 (2.24) μ_B/Fe for $1/3$ of the Fe atoms in ZrCo_3B_2 -type (MgNi_3B_2 -type) MgFe_3B_2 .

Moving forward to the Fe-rich region, there is a noticeable series of metastable phases residing on the same path in the

compositional space (Figure 1). They are $\text{In}(\text{Ni}_{11}\text{B}_3)_2$ -type⁴⁸ ($Fm\bar{3}m$ and $F43m$ space groups) $\text{MgFe}_{22}\text{B}_6$, $\text{Ni}_{43}(\text{GeB}_4)_3$ -type^{23,49} (experimental $Fm\bar{3}m$ and computational $R3m$ space groups) $\text{Mg}_3\text{Fe}_{43}\text{B}_{12}$, $\text{Ga}_2(\text{Co}_7\text{B}_2)_3$ -type⁵³ ($Fm\bar{3}m$ space group) $\text{Mg}_2\text{Fe}_{21}\text{B}_6$, $\text{Al}_5\text{Ni}_{41}\text{B}_{12}$ -type^{23,50} (experimental $Fm\bar{3}m$ and computational $R3m$ space groups) $\text{Mg}_5\text{Fe}_{41}\text{B}_{12}$, $\text{Zr}_8\text{Ni}_{61}\text{B}_{18}$ -type^{23,51,52} (experimental $Fm\bar{3}m$ and computational $P3m1$ space groups) $\text{Mg}_8\text{Fe}_{61}\text{B}_{18}$, and $\text{Ga}_3(\text{Ni}_{10}\text{B}_3)_2$ -type^{23,48} ($Fm\bar{3}m$ space group) $\text{Mg}_3\text{Fe}_{20}\text{B}_6$. Stoichiometrically, they can all be denoted as $\text{Mg}_x\text{Fe}_{23-x}\text{B}_6$, and x gradually increases in this particular sequence. Structurally, they are all derived from the Cr_{23}C_6 -type¹¹⁰ ($Fm\bar{3}m$ space group) structure. Cr_{23}C_6 -type borides are generally soft magnets. This series of phases is also related to the metastable Fe–B binary phase, $Fm\bar{3}m$ Fe_{23}B_6 ,¹¹¹ which is often identified as an intermediate phase precipitating during Fe-based metallic glass materials' annealing and crystallization processes.¹¹² There is also a metastable ErNi_3B_3 -type⁵⁴ ($I4_1/AMD$ space group) MgFe_7B_3 phase off this path with structural anisotropy. We have checked ferromagnetism for these Fe-rich ternary compounds, and they are all strongly magnetic with moment $\sim 2 \mu_B/\text{Fe}$. All the predicted low-energy phases in this study show great promise for future experimental syntheses and characterizations.

Significance of High-Throughput Sampling of Compositional Space in Exploring Unknowns. Our high-throughput sampling of compositional space provides a feasible way to explore desired physical properties with target elements and structures totally unknown. For each ternary system to be screened, we can obtain some clues by carefully observing the trends of certain properties as the composition varies in the compositional space. For example, the location where fragile magnetism happens may be approached by observing the trend of magnetism in the compositional space. Fragile magnetism is a magnetic state easily disrupted or altered by external parameters such as magnetic field, pressure, temperature, and chemical doping. Fragile magnetic states are often in the vicinity of quantum criticality and can be tuned to transit to novel quantum magnetic or superconducting states. Take the present Mg–Fe–B, for instance. Ternary phases in the Fe-rich region generally have strong magnetic moments $\sim 2 \mu_B/\text{Fe}$, and those in the B–Fe-intermediate region generally have well-defined moments $\sim 1 \mu_B/\text{Fe}$. Thus, the B-rich region becomes our target compositional space for seeking fragile magnetism, especially the FeB_2 – MgB_2 path, along or near which many low-energy phases are located. Note that MgB_2 is a well-known superconductor. We have shown that MgFeB_4 and the isomorphic YCrB_4 -type compounds exhibit Van Hove singularities in their electronic band structures.¹⁵ Some of these YCrB_4 -type compounds have been predicted to be dimerized quantum magnets near the quantum critical point for Bose–Einstein condensation of magnetic excitations.¹⁶ The other predicted stable ternary compound near MgFeB_4 , Mg_2FeB_6 , is nonmagnetic, according to our calculations. Our analysis of the trend of magnetism has helped us find a novel magnetism in ternary metal borides. It would be even more remarkable if other fragile magnetic phenomena could be found in this region or if other unknowns could be discovered in boride systems.

CONCLUSIONS

To venture into unexplored material compositional space and accelerate the discovery of functional materials with significant prediction and synthesis challenges, we have outlined a

workflow that combines high-throughput crystal structure prediction utilizing prototypes and high-throughput automated PXRD matching. The efficiency of the workflow is demonstrated in a representative ternary metal boride system that has no previously known ternary phase, Mg–Fe–B. Using 275 ternary boride prototypes classified, 23 (158) stable and metastable ternary phases with $E_d < 50$ (200) meV/atom are predicted. $\text{Gd}_2(\text{FeB})_7$ -type $\text{Mg}_2\text{Fe}_7\text{B}_7$ and ZrCo_3B_2 -type MgFe_3B_2 are identified to be the first experimentally observed Mg–Fe–B ternary compounds using the workflow. $\text{Mg}_2\text{Fe}_7\text{B}_7$ and its related $\text{Mg}_x(\text{FeB})_4$ phases have a channeled structure. The 1D chain of Mg atoms within the channel has a mismatched sublattice period with that of the (FeB) channel walls. We bring this series of superstructures to attention and provide insights for analyses of their incommensurate and commensurate $[\text{Mg}] / [(\text{FeB})]$ ratios with respect to the PXRD. This series of phases also has Mg's 1D diffusion and intercalation-deintercalation mechanism. They are predicted to exhibit exceptionally fast superionic transport of Mg and outstanding charge capacity, which make them promising next-generation Mg battery cathode materials. This discovery enables potential applications of borides as electrode materials, fast ionic conductors, and other related functional materials. This work also portrays the map and landscape of a typical ternary metal boride system, which is of certain transferability to other ternary metal boride systems with similar chemical environments, such as A – T – B and RE – T – B . The outlined prototype- and PXRD-assisted crystal structure prediction workflow opens a new route for materials discovery in the complex ternary and multinary compositional spaces across the periodic table. It is expected to instruct researchers to select and analyze promising syntheses almost “on the fly” at the beamline and bridge the gap between theories and experiments.

METHODS

High-Throughput Crystal Structure Prediction Utilizing Prototypes. Structures of all ternary borides are extracted from the Materials Project.²³ By the time this study is conducted, there are 2556 ternary borides X–Y–B throughout the periodic table. Considering metal elements' vastly different chemical environments from F, Cl, Br, I, O, S, N, P, C, and H, we exclude phases containing these elements and obtain 1466 ternary borides. They are further categorized into 275 structural prototypes according to their stoichiometry (e.g., AB_2C_3), space group, and Wyckoff site occupancies.³² For these prototypical X–Y–B structures, we substitute X and Y with Mg and Fe and then swap Mg and Fe, which yields 550 distinct Mg–Fe–B ternary phases. The extraction of prototypes greatly decreases the high-throughput computational load by $\sim 80\%$ and enhances the transferability of the workflow to other ternary systems. Then, density-functional theory (DFT) calculations are conducted for these 550 phases.

Spin-polarized DFT calculations are performed using VASP employing the Perdew–Burke–Ernzerhof generalized gradient approximation (PBE-GGA) and the projector augmented wave method (PAW). A plane-wave-basis set is used with a kinetic energy cutoff of 520 eV. The convergence thresholds are 10^{-5} eV for electronic self-consistency and 0.01 eV \AA^{-1} for ionic relaxation. The Brillouin zone is sampled by the Monkhorst–Pack scheme with a k-point grid of $2\pi \times 0.033 \text{\AA}^{-1}$ in the structural optimization and with a denser k-point grid of $2\pi \times 0.022 \text{\AA}^{-1}$ in the static calculation. The formation energy with respect to the three elemental ground-state bulk phases of the constituent elements, i.e., Mg, Fe, B (denoted as E_f), and the formation energy with respect to the three reference phases forming the Gibbs triangle on the convex hull (denoted as E_d) are then computed. Apart from the three elemental phases, six

known^{23,24} binary ground-state phases, Fe_2B ,¹¹³ FeB ,¹¹⁴ FeB_2 ,¹¹⁵ MgB_2 ,¹¹⁶ MgB_4 ,¹¹⁷ and MgB_7 ,¹¹⁸ are included to construct the convex hull. If a ternary phase has E_f below the convex hull, then the convex hull is reconstructed to include the ternary phase's E_f . After the stabilities of all ternary phases are evaluated and the convex hull is finalized, $E_d = 0$ indicates a stable phase part of the convex hull, and $E_d > 0$ indicates the distance above the convex hull.

High-Throughput Automated Diffraction Pattern Matching. Here, we implement an automated tool to compare the diffraction patterns of new phases with the experimental measurement. Diffraction patterns are simulated using pymatgen¹¹⁹ for the fully relaxed structures by DFT. Peaks are then smeared as pseudo-Voigt. The integrated calculated peak intensities, $\sum_{\text{peaks}} I_{\text{cal}}^2$, are normalized with respect to the experimental one, $\sum_{\text{peaks}} I_{\text{exp}}^2$. The goodness of the match, also known as the *R* factor, is then obtained as $\frac{\sum_{\text{peaks}} (I_{\text{cal}} - I_{\text{exp}})^2}{\sum_{\text{peaks}} I_{\text{exp}}^2}$ ³²

³² Since the experimental PXRDs in this study were obtained *in situ* at high temperatures, we consider a series of volumes with isotropic thermal expansion to simulate its PXRD for each phase. Here, thermal expansivity serves as a numerical parameter to solve the issue of offsets between DFT-calculated ground-state and measured finite-temperature volumes and the corresponding peaks. The constant thermal expansivity is limited up to $25 \times 10^{-6} \text{ K}^{-1}$, a typical value for magnesium and approximately twice the value for iron. This value is a confident upper limit for any Mg–Fe–B ternary compounds' thermal expansivity. Then, the lowest *R* among all volumes is assigned to this phase for the final sort of all phases. This strategy effectively minimizes the *R* for a matched pattern but not for a mismatched pattern, which provides a better numerical resolution. A previous work³² used a different strategy addressing the offset between experimental and calculated peaks, which pairs them together if they are within 0.15° from each other. Both strategies are capable of numerically dealing with the issue of PXRD matching due to DFT errors, zero-point motion, and temperature effects. Finally, we select the lowest-*R* structures as matches and solutions. The difference between a match and a mismatch can be told unambiguously since a mismatch almost always has an *R* factor more than 0.2 above the lowest *R* found.

Electrochemical Performance and Diffusion Coefficient. The battery voltage vs Mg/Mg²⁺ of $\text{Mg}_x(\text{FeB})_4$ ($0 \leq x \leq 1$) is simulated with a 36-atom $1 \times 1 \times 2$ supercell of MgFe_4B_4 . (The voltage platform shown in Figure 4a is flat, and the gradient is tiny. Thus, larger simulation cells are not needed.) The relative stability of $\text{Mg}_x(\text{FeB})_4$ polymorphs at each Mg composition *x* is evaluated by

$$E_f = E(\text{Mg}_x(\text{FeB})_4) - [xE(\text{Mg}(\text{FeB})_4) + (1-x)E((\text{FeB})_4)] \quad (1)$$

where *E* is the calculated total energy for a given structure. The *E_f* at different compositions forms a convex hull. Then, the voltage vs Mg/Mg²⁺ is calculated for the convex hull phases as¹²⁰

$$V = -\frac{E(\text{Mg}_{x_2}(\text{FeB})_4) - E(\text{Mg}_{x_1}(\text{FeB})_4) - (x_2 - x_1)E(\text{Mg})}{2(x_2 - x_1)e} \quad (2)$$

where *x₂* and *x₁* are the Mg composition before and after the Mg extraction from the host structure, respectively, and 2 is the valence electron number of Mg.

The maximum specific capacity is calculated as¹²⁰

$$C = \frac{2x_{\max}F}{M} \quad (3)$$

where 2 is the valence electron number of Mg, *x_{max}* is the maximum concentration of Mg in the electrode, *F* is the Faraday constant, and *M* is the molar mass of the electrode.

To calculate the diffusion coefficient, AIMD simulations are performed using the PAW PBE as implemented in VASP. The electronic temperature was set the same as the ionic temperature using the Mermin functional. MgFe_4B_4 is simulated with a 288-atom 2

$\times 2 \times 4$ supercell. $\text{Mg}_2\text{Fe}_7\text{B}_7$, having a large primitive cell already, is simulated with a 128-atom $1 \times 1 \times 1$ supercell. Both Brillouin zones are sampled by the Γ k-point. Simulations are conducted in the NVT ensemble at 300 K controlled by Nosé thermostat. Each simulation runs for over 16 ps after thermal equilibration, with a time step of 1 fs.

The diffusion coefficient is calculated as⁹⁵

$$D = \frac{1}{2bN} \lim_{t \rightarrow \infty} \frac{d}{dt} \left[\sum_{i=1}^N \sum_{k=1}^M (\Delta \vec{r}_{i,k}(t))^2 \right] \quad (4)$$

where *b* is the dimensionality factor, *N* is the number of mobile ions, *M* is the total number of steps that the mobile ions traveled, and $\Delta \vec{r}$ is the displacement of the mobile ions. Here, since Mg atoms only travel in 1D, *b* = 1. In practice, *D* is obtained by a linear fitting of the MSD(*t*) and dividing the slope by a factor of 2. The MSD of Mg in the MgFe_4B_4 at 300 K is displayed in Figure 4c. The MSD of Mg in the $\text{Mg}_2\text{Fe}_7\text{B}_7$ at 300 K is displayed in Figure S7 of the Supporting Information.

The ionic conductivity is linked to the diffusion coefficient by the Nernst–Einstein relation⁹⁵

$$\sigma = \frac{nq^2}{k_B T} D \quad (5)$$

where *n* is the number of ions per unit volume, and *q* is the ionic charge.

In addition, both the non-spin-polarized and spin-polarized electronic band structures show a metallic nature of MgFe_4B_4 (see Figure S5 of the Supporting Information). The intercalation and deintercalation of Mg should not modify its metallicity significantly.

Extraction of Experimental *In Situ* PXRDs and Rietveld Refinements. In the experimental waterfall *in situ* PXRDs,¹⁵ the broad peak sustaining at $2\theta \sim 3^\circ$ is attributed to the amorphous boron with an excess amount. The temperature profile of the sharp diffraction peaks categorizes the PXRDs into different temperature ranges. At each temperature range, the PXRDs are dominated by peaks of major phase(s) of this temperature range, though peak tails of identified major phases at other temperature ranges may still exist. To minimize the impact of peak tails of other temperature ranges, we select representative PXRD with the sharpest peaks of each temperature range's major phase(s). Two representative PXRDs at 741 and 621 °C, respectively, are selected. These two temperatures are the characteristic temperature of two temperature ranges, respectively, with low-angle peaks and most likely ternary phase.

To further confirm the two discovered ternary phases, Rietveld refinements are carried out using the GSAS package and the EXPGUI interface. The broad peak at $2\theta \sim 3^\circ$ attributed to amorphous boron is treated as background. Rietveld refinements are conducted at 741 °C for $\text{Gd}_2(\text{FeB})_7$ -type $\text{Mg}_2\text{Fe}_7\text{B}_7$ and 621 °C for ZrCo_3B_2 -type MgFe_3B_2 , respectively. At each temperature, peak tails of identified major phases at other temperature ranges are excluded. Unidentified peaks are not excluded and contribute to the fitting errors.

ASSOCIATED CONTENT

Supporting Information

The Supporting Information is available free of charge at <https://pubs.acs.org/doi/10.1021/jacs.4c12648>.

Simulated single-crystal diffraction patterns, electronic band structures of Nd(CoB)₄-type MgFe_4B_4 and ZrCo₃B₂-type MgFe_3B_2 , MSD of Mg in the $\text{Gd}_2(\text{FeB})_7$ -type $\text{Mg}_2\text{Fe}_7\text{B}_7$ at 300 K, proposed structural model $\text{Mg}_7\text{Fe}_{24}\text{B}_{24}$, materials inventory of the 1D channeled structure, and categorization of 1466 ternary borides into 275 structural prototypes (PDF)

AUTHOR INFORMATION

Corresponding Author

Yang Sun – Department of Physics, Xiamen University, Xiamen 361005, China; orcid.org/0000-0002-4344-2920; Email: yangsун@xmu.edu.cn

Authors

Zhen Zhang – Department of Physics and Astronomy, Iowa State University, Ames, Iowa 50011, United States; orcid.org/0009-0001-0810-8054

Shiya Chen – Department of Physics, Xiamen University, Xiamen 361005, China

Feng Zheng – School of Science, Jimei University, Xiamen 361021, China

Vladimir Antropov – Department of Physics and Astronomy, Iowa State University, Ames, Iowa 50011, United States; Ames National Laboratory, U.S. Department of Energy, Ames, Iowa 50011, United States

Kai-Ming Ho – Department of Physics and Astronomy, Iowa State University, Ames, Iowa 50011, United States

Complete contact information is available at:

<https://pubs.acs.org/10.1021/jacs.4c12648>

Author Contributions

[†]Equal contribution

Notes

The authors declare no competing financial interest.

ACKNOWLEDGMENTS

The work at Iowa State University was supported by the U.S. Department of Energy Established Program to Stimulate Competitive Research (EPSCoR) Grant DE-SC0024284. The Ames National Laboratory is operated for the U.S. Department of Energy by Iowa State University under Contract DE-AC02-07CH11358. The work at Xiamen University was supported by the National Natural Science Foundation of China (Grant T2422016), the Natural Science Foundation of Xiamen (Grant 3502Z202371007), and the Fundamental Research Funds for the Central Universities (Grant 20720230014). The work at Jimei University was supported by the National Natural Science Foundation of China (Grant 12404077), the Natural Science Foundation of Xiamen Municipality (Grant 3502Z202372015), and the Research Foundation of Jimei University (Grant ZQ2023013). We would like to thank Jingyi Zhuang (Columbia University), Hongjin Wang (Columbia University), and Chenxing Luo (Columbia University) for the technical support for the single-crystal diffraction simulations.

REFERENCES

- (1) Akopov, G.; Yeung, M. T.; Kaner, R. B. Rediscovering the Crystal Chemistry of Borides. *Adv. Mater.* **2017**, *29*, 1604506.
- (2) Scheifers, J. P.; Zhang, Y.; Fokwa, B. P. T. Boron: Enabling Exciting Metal-Rich Structures and Magnetic Properties. *Acc. Chem. Res.* **2017**, *50*, 2317–2325.
- (3) Fokwa, B. P. T.; Samolyuk, G. D.; Miller, G. J.; Dronskowski, R. Ladders of a Magnetically Active Element in the Structure of the Novel Complex Boride $Ti_9Fe_2Ru_{18}B_8$: Synthesis, Structure, Bonding, and Magnetism. *Inorg. Chem.* **2008**, *47*, 2113–2120.
- (4) Brgoch, J.; Goerens, C.; Fokwa, B. P. T.; Miller, G. J. Scaffolding, Ladders, Chains, and Rare Ferrimagnetism in Intermetallic Borides: Electronic Structure Calculations and Magnetic Ordering. *J. Am. Chem. Soc.* **2011**, *133*, 6832–6840.

(5) Shankhari, P.; Janka, O.; Pöttgen, R.; Fokwa, B. P. T. Rare-Earth-Free Magnets: Enhancing Magnetic Anisotropy and Spin Exchange Toward High-T_C $Hf_2MIr_5B_2$ ($M = Mn, Fe$). *J. Am. Chem. Soc.* **2021**, *143*, 4205–4212.

(6) Nagamatsu, J.; Nakagawa, N.; Muranaka, T.; Zenitani, Y.; Akimitsu, J. Superconductivity at 39 K in Magnesium Diboride. *Nature* **2001**, *410*, 63–64.

(7) Kortus, J.; Mazin, I. I.; Belashchenko, K. D.; Antropov, V. P.; Boyer, L. L. Superconductivity of Metallic Boron in MgB₂. *Phys. Rev. Lett.* **2001**, *86*, 4656.

(8) Chen, S.; Wu, Z.; Zhang, Z.; Wu, S.; Ho, K.-M.; Antropov, V.; Sun, Y. High-Throughput Screening for Boride Superconductors. *Inorg. Chem.* **2024**, *63*, 8654–8663.

(9) Yeung, M. T.; Mohammadi, R.; Kaner, R. B. Ultracompressible, Superhard Materials. *Annu. Rev. Mater. Res.* **2016**, *46*, 465–485.

(10) Akopov, G.; Yeung, M. T.; Turner, C. L.; Mohammadi, R.; Kaner, R. B. Extrinsic Hardening of Superhard Tungsten Tetraboride Alloys with Group 4 Transition Metals. *J. Am. Chem. Soc.* **2016**, *138*, 5714–5721.

(11) Pu, Z.; Liu, T.; Zhang, G.; Liu, X.; Gauthier, M. A.; Chen, Z.; Sun, S. Nanostructured Metal Borides for Energy-Related Electrocatalysis: Recent Progress, Challenges, and Perspectives. *Small Methods* **2021**, *5*, 2100699.

(12) Park, H.; Zhang, Y.; Scheifers, J. P.; Jothi, P. R.; Encinas, A.; Fokwa, B. P. T. Graphene-and Phosphorene-like Boron Layers with Contrasting Activities in Highly Active Mo₂B₄ for Hydrogen Evolution. *J. Am. Chem. Soc.* **2017**, *139*, 12915–12918.

(13) Gupta, S.; Patel, M. K.; Miotello, A.; Patel, N. Metal Boride-Based Catalysts for Electrochemical Water-Splitting: A Review. *Adv. Funct. Mater.* **2020**, *30*, 1906481.

(14) Saglik, K.; Mete, B.; Terzi, I.; Candolfi, C.; Aydemir, U. Thermoelectric Borides: Review and Future Perspectives. *Adv. Physics Res.* **2023**, *2*, 2300010.

(15) Sun, Y.; Zhang, Z.; Porter, A. P.; Kovnir, K.; Ho, K. M.; Antropov, V. Prediction of Van Hove Singularity Systems in Ternary Borides. *Npj Comput. Mater.* **2023**, *9*, 204.

(16) Zhang, Z.; Porter, A. P.; Sun, Y.; Belashchenko, K. D.; Viswanathan, G.; Sarkar, A.; Gamage, E. H.; Kovnir, K.; Ho, K. M.; Antropov, V. Unveiling a Family of Dimerized Quantum Magnets, Conventional Antiferromagnets, and Nonmagnets in Ternary Metal Borides. *J. Am. Chem. Soc.* **2024**, *146*, 16878–16891.

(17) Zhang, B.; Zhou, J.; Sun, Z. MBenes: Progress, Challenges and Future. *J. Mater. Chem. A* **2022**, *10*, 15865–15880.

(18) Kota, S.; Sokol, M.; Barsoum, M. W. A Progress Report on the MAB Phases: Atomically Laminated, Ternary Transition Metal Borides. *Int. Mater. Rev.* **2020**, *65*, 226–255.

(19) Gvozdetskyi, V.; Bhaskar, G.; Batuk, M.; Zhao, X.; Wang, R.; Carnahan, S. L.; Hanrahan, M. P.; Ribeiro, R. A.; Canfield, P. C.; Rossini, A. J.; Wang, C. Z.; Ho, K. M.; Hadermann, J.; Zaikina, J. V. Computationally Driven Discovery of a Family of Layered LiNiB Polymorphs. *Angew. Chem., Int. Ed.* **2019**, *58*, 15855–15862.

(20) Zagorac, D.; Muller, H.; Ruehl, S.; Zagorac, J.; Rehme, S. Recent Developments in the Inorganic Crystal Structure Database: Theoretical Crystal Structure Data and Related Features. *J. Appl. Crystallogr.* **2019**, *52*, 918–925.

(21) Gutfleisch, O.; Willard, M. A.; Brück, E.; Chen, C. H.; Sankar, S. G.; Liu, J. P. Magnetic Materials and Devices for the 21st Century: Stronger, Lighter, and More Energy Efficient. *Adv. Mater.* **2011**, *23*, 821–842.

(22) Xia, W.; Sakurai, M.; Balasubramanian, B.; Liao, T.; Wang, R.; Zhang, C.; Sun, H.; Ho, K. M.; Chelikowsky, J. R.; Sellmyer, D. J.; Wang, C. Z. Accelerating the Discovery of Novel Magnetic Materials Using Machine Learning—Guided Adaptive Feedback. *Proc. Natl. Acad. Sci. U.S.A.* **2022**, *119*, No. e2204485119.

(23) Jain, A.; Ong, S. P.; Hautier, G.; Chen, W.; Richards, W. D.; Dacek, S.; Cholia, S.; Gunter, D.; Skinner, D.; Ceder, G.; Persson, K. A. Commentary: The Materials Project: A Materials Genome Approach to Accelerating Materials Innovation. *APL Mater.* **2013**, *1*, No. 011002.

- (24) Kirklin, S.; Saal, J. E.; Meredig, B.; Thompson, A.; Doak, J. W.; Aykol, M.; Rühl, S.; Wolverton, C. The Open Quantum Materials Database (OQMD): Assessing the Accuracy of DFT Formation Energies. *Npj Comput. Mater.* **2015**, *1*, 15010.
- (25) Kuzma, Y. B. Crystal Structure of the YCrB_4 Compound and Its Analogs. *Kristallografiya* **1970**, *15*, 312–314.
- (26) Nayeb-Hashemi, A. A.; Clark, J. B. *Phase Diagrams of Binary Magnesium Alloys*; ASM International: Metals Park, 1988.
- (27) Wang, R.; Sun, Y.; Gvozdetskyi, V.; Zhao, X.; Zhang, F.; Xu, L. H.; Zaikina, J. V.; Lin, Z.; Wang, C. Z.; Ho, K. M. Theoretical Search for Possible Li-Ni-B Crystal Structures Using an Adaptive Genetic Algorithm. *J. Appl. Phys.* **2020**, *127*, 94902.
- (28) Wang, R.; Xia, W.; Slade, T. J.; Fan, X.; Dong, H.; Ho, K. M.; Canfield, P. C.; Wang, C. Z. Machine Learning Guided Discovery of Ternary Compounds Involving La and Immiscible Co and Pb Elements. *Npj Comput. Mater.* **2022**, *8*, 258.
- (29) Canfield, P. C. *New Materials Physics. Rep. Prog. Phys.* **2020**, *83*, No. 016501.
- (30) Bonnick, P.; Muldoon, J. A Trip to Oz and a Peak Behind the Curtain of Magnesium Batteries. *Adv. Funct. Mater.* **2020**, *30*, 1910510.
- (31) Zhao, X.; Nguyen, M. C.; Zhang, W. Y.; Wang, C. Z.; Kramer, M. J.; Sellmyer, D. J.; Li, X. Z.; Zhang, F.; Ke, L. Q.; Antropov, V. P.; Ho, K. M. Exploring the Structural Complexity of Intermetallic Compounds by an Adaptive Genetic Algorithm. *Phys. Rev. Lett.* **2014**, *112*, No. 045502.
- (32) Griesemer, S. D.; Ward, L.; Wolverton, C. High-Throughput Crystal Structure Solution Using Prototypes. *Phys. Rev. Mater.* **2021**, *5*, No. 105003.
- (33) Kuzma, Y. B.; Svarichevskaya, S. I. Crystal Structure of Y_2ReB_6 and Its Analogs. *Sov. Phys. Crystallogr.* **1972**, *17*, 569–571.
- (34) Szymanski, N. J.; Zeng, Y.; Bennett, T.; Patil, S.; Keum, J. K.; Self, E. C.; Bai, J.; Cai, Z.; Giovine, R.; Ouyang, B.; Wang, F.; Bartel, C. J.; Clément, R. J.; Tong, W.; Nanda, J.; Ceder, G. Understanding the Fluorination of Disordered Rocksalt Cathodes through Rational Exploration of Synthesis Pathways. *Chem. Mater.* **2022**, *34*, 7015–7028.
- (35) Bianchini, M.; Wang, J.; Clément, R. J.; Ouyang, B.; Xiao, P.; Kitchev, D.; Shi, T.; Zhang, Y.; Wang, Y.; Kim, H.; Zhang, M.; Bai, J.; Wang, F.; Sun, W.; Ceder, G. The Interplay between Thermodynamics and Kinetics in the Solid-State Synthesis of Layered Oxides. *Nat. Mater.* **2020**, *19*, 1088–1095.
- (36) Bhaskar, G.; Gvozdetskyi, V.; Batuk, M.; Wiaderek, K. M.; Sun, Y.; Wang, R.; Zhang, C.; Carnahan, S. L.; Wu, X.; Ribeiro, R. A.; Bud'ko, S. L.; Canfield, P. C.; Huang, W.; Rossini, A. J.; Wang, C. Z.; Ho, K. M.; Hadermann, J.; Zaikina, J. V. Topochemical Deintercalation of Li from Layered LiNiB: Toward 2D MBene. *J. Am. Chem. Soc.* **2021**, *143*, 4213–4223.
- (37) Sun, W.; Dacek, S. T.; Ong, S. P.; Hautier, G.; Jain, A.; Richards, W. D.; Gamst, A. C.; Persson, K. A.; Ceder, G. The Thermodynamic Scale of Inorganic Crystalline Metastability. *Sci. Adv.* **2016**, *2*, No. e1600225.
- (38) Opahle, I.; Parma, A.; McEniry, E. J.; Drautz, R.; H Madsen, G. K. High-Throughput Study of the Structural Stability and Thermoelectric Properties of Transition Metal Silicides. *New J. Phys.* **2013**, *15*, No. 105010.
- (39) Balluff, J.; Diekmann, K.; Reiss, G.; Meinert, M. High-Throughput Screening for Antiferromagnetic Heusler Compounds Using Density Functional Theory. *Phys. Rev. Mater.* **2017**, *1*, No. 034404.
- (40) Singh, H. K.; Zhang, Z.; Opahle, I.; Ohmer, D.; Yao, Y.; Zhang, H. High-Throughput Screening of Magnetic Antiperovskites. *Chem. Mater.* **2018**, *30*, 6983–6991.
- (41) Rogl, P.; Nowotny, H. Ternäre Komplexboride Mit ThMoB_4 -Typ. *Monatsh. Chem.* **1974**, *105*, 1082–1098.
- (42) Givord, D.; Tenaud, P.; Moreau, J. M. Refinement of the Crystal Structure of $\text{R}_{1+\epsilon}\text{Fe}_4\text{B}_4$ Compounds ($\text{R} \equiv \text{Nd}, \text{Gd}$). *J. Less-Common Met.* **1986**, *123*, 109–116.
- (43) Givord, D.; Moreau, J. M.; Tenaud, P. $\text{Nd}_5\text{Fe}_{18}\text{B}_{18}$ ($\text{Nd}_{1.11}\text{Fe}_4\text{B}_4$), a New Nowotny-like Phase. Structural and Magnetic Properties. *Solid State Commun.* **1985**, *55*, 303–306.
- (44) Bocelli, G.; Calestani, G.; Leccabue, F. Structural Investigation of Incommensurate $\text{Nd}_{1+\epsilon}\text{Fe}_4\text{B}_4$ Phase. *Solid State Commun.* **1988**, *65*, 1301–1305.
- (45) Zavalii, P. Y.; Kuzma, Y. B.; Zavalii, L. V. $\text{Sm}_{11}(\text{Co}_4\text{B}_4)_{10}$ —a New Member of the Family of Incommensurate Structures. *Kristallografiya* **1990**, *35*, 638–641.
- (46) Chaban, N. F.; Akselrud, L. G.; Bruskov, V. A.; Kuz'ma, Y. B. Crystal Structure of the New Boride Er_3CrB_7 . *Kristallografiya* **1985**, *30*, 187–189.
- (47) Konrad, T.; Jeitschko, W. $\text{U}_3\text{Mo}_{10}\text{B}_{24}$, a Boride Containing Three Different Kinds of Boron Polyanions. *J. Alloys Compd.* **1996**, *233*, L3–L7.
- (48) Kotzott, D.; Ade, M.; Hillebrecht, H. Single Crystal Studies on Boron-Rich τ -Borides $\text{Ni}_{23-x}\text{M}_x\text{B}_6$ ($\text{M} = \text{Zn}, \text{Ga}, \text{In}, \text{Sn}, \text{Ir}$)—The Surprising Occurrence of B_4 -Tetraheda as a Normal Case? *J. Solid State Chem.* **2010**, *183*, 2281–2289.
- (49) Stadelmaier, H. H.; Lee, F. M. Nickelecke Des Dreistoffsysteems Nickel-Germanium-Bor. *Metall* **1964**, *18*, 111–113.
- (50) Hillebrecht, H.; Ade, M. B_4 Tetrahedra for Aluminum Atoms—A Surprising Substitution in τ -Borides $\text{Ni}_{20}\text{Al}_3\text{B}_6$ and $\text{Ni}_{20}\text{AlB}_{14}$. *Angew. Chem., Int. Ed.* **1998**, *37*, 935–938.
- (51) Artini, C.; Muolo, M. L.; Passerone, A.; Valenza, F.; Manfrinetti, P.; Cacciamani, G. Experimental Investigations and Thermodynamic Modeling in the ZrB_2 –Ni Section of the B–Ni–Zr System. *J. Alloys Compd.* **2014**, *592*, 115–120.
- (52) Artini, C.; Provino, A.; Valenza, F.; Pani, M.; Cacciamani, G. Stability and Crystal Chemistry of the Ternary Borides $\text{M}_2(\text{Ni}_{21-x}\text{M}_x)\text{B}_6$ ($\text{M} \equiv \text{Ti}, \text{Zr}, \text{Hf}$). *Solid State Sci.* **2016**, *51*, 40–50.
- (53) Fiedler, M.-L.; Stadelmaier, H. H.; Snipes, E. B. The Ternary System Cobalt-Gallium-Boron. *Int. J. Mater. Res.* **1977**, *68*, 765–767.
- (54) Kuzma, Y. B.; Babizhetskyi, V.; Veremchuk, I.; Chaban, N. New Borides $\text{Er}_{0.917}\text{Ni}_{4.09}\text{B}$ and ErNi_7B_3 and Their Crystal Structures. *J. Solid State Chem.* **2004**, *177*, 425–430.
- (55) Karpinski, J.; Zhigadlo, N. D.; Katrych, S.; Rogacki, K.; Batlogg, B.; Tortello, M.; Puzniak, R. MgB_2 Single Crystals Substituted with Li and with Li-C: Structural and Superconducting Properties. *Phys. Rev. B* **2008**, *77*, No. 214507.
- (56) Tan, X.; Chai, P.; Thompson, C. M.; Shatruk, M. Magnetocaloric Effect in AlFe_2B_2 : Toward Magnetic Refrigerants from Earth-Abundant Elements. *J. Am. Chem. Soc.* **2013**, *135*, 9553–9557.
- (57) Kuz'ma, Y. B.; Byilonyzhko, N. S. Crystal Structure of the NdCo_4B_4 Compound and Its Analogues. *Dopov. Akad. Nauk Ukr. RSR, Ser. A: Fiz.-Tekh. Mat. Nauki* **1976**, *39*, 275–277.
- (58) Rogl, P. Ternary Metal Borides [La,Ce,Pr,Nd,Sm] Os_4B_4 and [$\text{Y,La,Ce,Pr,Nd,Sm,Gd,Tb}$] Ir_4B_4 with NdCo_4B_4 -Type Structure. *Monatsh. Chem.* **1979**, *110*, 235–243.
- (59) Grüttner, A.; Yvon, K. Lanthanum Ruthenium Boride, LaRu_4B_4 . *Acta Crystallogr.* **1979**, *35*, 451–453.
- (60) Chaban, N. F.; Kuz'ma, Y. B.; Bilonizhko, N. S.; Kachmar, O. O.; Petriv, N. B. Ternary (Nd, Sm, Gd) - Fe - B Systems. *Dopov. Akad. Nauk Ukr. RSR, Ser. A: Fiz.-Tekh. Mat. Nauki* **1979**, *41*, 875–877.
- (61) Kuz'ma, Y. B. Crystalline Structures of the Compounds NbNiB and TaNiB . *Sov. Phys. Crystallogr.* **1969**, *13*, 597–598.
- (62) Ade, M.; Kotzott, D.; Hillebrecht, H. Synthesis and Crystal Structures of the New Metal-Rich Ternary Borides $\text{Ni}_{12}\text{AlB}_8$, $\text{Ni}_{12}\text{GaB}_8$ and $\text{Ni}_{10.6}\text{Ga}_{0.4}\text{B}_6$ —Examples for the First B_5 Zig-Zag Chain Fragment. *J. Solid State Chem.* **2010**, *183*, 1790–1797.
- (63) Manfrinetti, P.; Pani, M.; Dhar, S. K.; Kulkarni, R. Structure, Transport and Magnetic Properties of MgNi_3B_2 . *J. Alloys Compd.* **2007**, *428*, 94–98.
- (64) Gross, K. J.; Züttel, A.; Schlapbach, L. On the Possibility of Metal Hydride Formation: Part I. The Synthesis of MgNi_3B_2 by Mechanical Milling and Sintering. *J. Alloys Compd.* **1998**, *274*, 234–238.

- (65) Voroshilov, Y. V.; Krypyakevych, P. I.; Kuz'ma, Y. B. Crystal Structures of $ZrCo_3B_2$ and $HfCo_3B_2$. *Sov. Phys. Crystallogr.* **1970**, *15*, 813–816.
- (66) Wu, S. Q.; Ji, M.; Wang, C. Z.; Nguyen, M. C.; Zhao, X.; Umemoto, K.; Wentzcovitch, R. M.; Ho, K. M. An Adaptive Genetic Algorithm for Crystal Structure Prediction. *J. Phys.: Condens. Matter* **2014**, *26*, No. 035402.
- (67) Hart, G. L. W.; Forcade, R. W. Generating Derivative Structures from Multilattices: Algorithm and Application to Hcp Alloys. *Phys. Rev. B* **2009**, *80*, No. 014120.
- (68) Szymanski, N. J.; Rendy, B.; Fei, Y.; Kumar, R. E.; He, T.; Milsted, D.; McDermott, M. J.; Gallant, M.; Cubuk, E. D.; Merchant, A.; Kim, H.; Jain, A.; Bartel, C. J.; Persson, K.; Zeng, Y.; Ceder, G. An Autonomous Laboratory for the Accelerated Synthesis of Novel Materials. *Nature* **2023**, *624*, 86–91.
- (69) Leeman, J.; Liu, Y.; Stiles, J.; Lee, S. B.; Bhatt, P.; Schoop, L. M.; Palgrave, R. G. Challenges in High-Throughput Inorganic Materials Prediction and Autonomous Synthesis. *PRX Energy* **2024**, *3*, No. 011002.
- (70) Racoppi, S.; De la Roza, A. O.; Hajinazar, S.; Zurek, E. Powder X-Ray Diffraction Assisted Evolutionary Algorithm for Crystal Structure Prediction. *arXiv* **2024**, arXiv:2407.05394. <https://www.arxiv.org/abs/2407.05394>.
- (71) Putz, H. *Match!-Phase Analysis Using Powder Diffraction*. Crystal Impact: Bonn 2024. <https://www.crystalimpact.de/match>.
- (72) Deaven, D. M.; Ho, K. M. Molecular Geometry Optimization with a Genetic Algorithm. *Phys. Rev. Lett.* **1995**, *75*, 288.
- (73) Lu, G.; Lee, S.; Lin, J.; You, L.; Sun, J.; Schmidt, J. T. RuGa_xSn_w Nowotny Chimney Ladder Phases and the 14-Electron Rule. *J. Solid State Chem.* **2002**, *164*, 210–219.
- (74) Leong, K. W.; Pan, W.; Wang, Y.; Luo, S.; Zhao, X.; Leung, D. Y. C. Reversibility of a High-Voltage, Cl⁻-Regulated, Aqueous Mg Metal Battery Enabled by a Water-in-Salt Electrolyte. *ACS Energy Lett.* **2022**, *7*, 2657–2666.
- (75) Chen, L.; Bao, J. L.; Dong, X.; Truhlar, D. G.; Wang, Y.; Wang, C.; Xia, Y. Aqueous Mg-Ion Battery Based on Polyimide Anode and Prussian Blue Cathode. *ACS Energy Lett.* **2017**, *2*, 1115–1121.
- (76) Zhang, H.; Ye, K.; Zhu, K.; Cang, R.; Yan, J.; Cheng, K.; Wang, G.; Cao, D. High-Energy-Density Aqueous Magnesium-Ion Battery Based on a Carbon-Coated FeVO₄ Anode and a Mg-OMS-1 Cathode. *Chem.—Eur. J.* **2017**, *23*, 17118–17126.
- (77) Liu, F.; Liu, Y.; Zhao, X.; Liu, X.; Fan, L. Z. Pursuit of a High-Capacity and Long-Life Mg-Storage Cathode by Tailoring Sandwich-Structured MXene@carbon Nanosphere Composites. *J. Mater. Chem. A* **2019**, *7*, 16712–16719.
- (78) Bančić, T.; Bitenc, J.; Pirnat, K.; Kopač Lautar, A.; Grdadolnik, J.; Randon Vitanova, A.; Dominko, R. Electrochemical Performance and Redox Mechanism of Naphthalene-Hydrazine Diimide Polymer as a Cathode in Magnesium Battery. *J. Power Sources* **2018**, *395*, 25–30.
- (79) Wang, F.; Fan, X.; Gao, T.; Sun, W.; Ma, Z.; Yang, C.; Han, F.; Xu, K.; Wang, C. High-Voltage Aqueous Magnesium Ion Batteries. *ACS Cent. Sci.* **2017**, *3*, 1121–1128.
- (80) Son, S. B.; Gao, T.; Harvey, S. P.; Steirer, K. X.; Stokes, A.; Norman, A.; Wang, C.; Cresce, A.; Xu, K.; Ban, C. An Artificial Interphase Enables Reversible Magnesium Chemistry in Carbonate Electrolytes. *Nat. Chem.* **2018**, *10*, 532–539.
- (81) Pagot, G.; Vezzù, K.; Nale, A.; Fauri, M.; Migliori, A.; Morandi, V.; Negro, E.; Di Noto, V. Chrysalis-Like Graphene Oxide Decorated Vanadium-Based Nanoparticles: An Extremely High-Power Cathode for Magnesium Secondary Batteries. *J. Electrochem. Soc.* **2020**, *167*, No. 070547.
- (82) Li, Z.; Vinayan, B. P.; Jankowski, P.; Njel, C.; Roy, A.; Vegge, T.; Maibach, J.; Lastra, J. M. G.; Fichtner, M.; Zhao-Karger, Z. Multi-Electron Reactions Enabled by Anion-Based Redox Chemistry for High-Energy Multivalent Rechargeable Batteries. *Angew. Chem., Int. Ed.* **2020**, *59*, 11483–11490.
- (83) Dong, H.; Liang, Y.; Tutusaus, O.; Mohtadi, R.; Zhang, Y.; Hao, F.; Yao, Y. Directing Mg-Storage Chemistry in Organic Polymers toward High-Energy Mg Batteries. *Joule* **2019**, *3*, 782–793.
- (84) Sun, T.; Du, H.; Zheng, S.; Tao, Z. Inverse-Spinel Mg₂MnO₄ Material as Cathode for High-Performance Aqueous Magnesium-Ion Battery. *J. Power Sources* **2021**, *515*, No. 230643.
- (85) Ruiz, R.; Pérez-Vicente, C.; Rubio, S.; Stoyanova, R.; Zuo, W.; Yang, Y.; Ortiz, G. F. A Cubic Mg₂MnO₄ Cathode for Non-Aqueous Magnesium Batteries. *Energy Storage Mater.* **2022**, *48*, 12–19.
- (86) Yang, J.; Li, J.; Gong, W.; Geng, F. Genuine Divalent Magnesium-Ion Storage and Fast Diffusion Kinetics in Metal Oxides at Room Temperature. *Proc. Natl. Acad. Sci. U.S.A.* **2021**, *118*, No. e2111549118.
- (87) Sun, X.; Bonnick, P.; Duffort, V.; Liu, M.; Rong, Z.; Persson, K. A.; Ceder, G.; Nazar, L. F. A High Capacity Thiospinel Cathode for Mg Batteries. *Energy Environ. Sci.* **2016**, *9*, 2273–2277.
- (88) Levi, M. D.; Lancrey, E.; Gizbar, H.; Gofer, Y.; Levi, E.; Aurbach, D. Phase Transitions and Diffusion Kinetics during Mg²⁺- and Li⁺-Ion Insertions into the Mo₆S₈ Chevrel Phase Compound Studied by PITT. *Electrochim. Acta* **2004**, *49*, 3201–3209.
- (89) Koketsu, T.; Ma, J.; Morgan, B. J.; Body, M.; Legein, C.; Dachraoui, W.; Giannini, M.; Demortière, A.; Salanne, M.; Dardoize, F.; Groult, H.; Borkiewicz, O. J.; Chapman, K. W.; Strasser, P.; Dambournet, D. Reversible Magnesium and Aluminium Ions Insertion in Cation-Deficient Anatase TiO₂. *Nat. Mater.* **2017**, *16*, 1142–1148.
- (90) Chen, C.; Wang, J.; Zhao, Q.; Wang, Y.; Chen, J. Layered Na₂Ti₃O₇/MgNaTi₃O₇/Mg_{0.5}Ti₃O₇ Nanoribbons as High-Performance Anode of Rechargeable Mg-Ion Batteries. *ACS Energy Lett.* **2016**, *1*, 1165–1172.
- (91) Liu, Q.; Su, X.; Lei, D.; Qin, Y.; Wen, J.; Guo, F.; Wu, Y. A.; Rong, Y.; Kou, R.; Xiao, X.; Aguesse, F.; Bareño, J.; Ren, Y.; Lu, W.; Li, Y. Approaching the Capacity Limit of Lithium Cobalt Oxide in Lithium Ion Batteries via Lanthanum and Aluminium Doping. *Nat. Energy* **2018**, *3*, 936–943.
- (92) Yang, S.; Wang, X.; Yang, X.; Bai, Y.; Liu, Z.; Shu, H.; Wei, Q. Determination of the Chemical Diffusion Coefficient of Lithium Ions in Spherical Li[Ni_{0.5}Mn_{0.3}Co_{0.2}]O₂. *Electrochim. Acta* **2012**, *66*, 88–93.
- (93) Montoro, L. A.; Rosolen, J. M. The Role of Structural and Electronic Alterations on the Lithium Diffusion in Li_xCo_{0.5}Ni_{0.5}O₂. *Electrochim. Acta* **2004**, *49*, 3243–3249.
- (94) Rui, X. H.; Ding, N.; Liu, J.; Li, C.; Chen, C. H. Analysis of the Chemical Diffusion Coefficient of Lithium Ions in Li₃V₂(PO₄)₃ Cathode Material. *Electrochim. Acta* **2010**, *55*, 2384–2390.
- (95) Gao, Y.; Nolan, A. M.; Du, P.; Wu, Y.; Yang, C.; Chen, Q.; Mo, Y.; Bo, S. H. Classical and Emerging Characterization Techniques for Investigation of Ion Transport Mechanisms in Crystalline Fast Ionic Conductors. *Chem. Rev.* **2020**, *120*, 5954–6008.
- (96) He, X.; Zhu, Y.; Mo, Y. Origin of Fast Ion Diffusion in SuperIonic Conductors. *Nat. Commun.* **2017**, *8*, 15893.
- (97) Canepa, P.; Bo, S. H.; Sai Gautam, G.; Key, B.; Richards, W. D.; Shi, T.; Tian, Y.; Wang, Y.; Li, J.; Ceder, G. High Magnesium Mobility in Ternary Spinel Chalcogenides. *Nat. Commun.* **2017**, *8*, 1759.
- (98) Kamaya, N.; Homma, K.; Yamakawa, Y.; Hirayama, M.; Kanno, R.; Yonemura, M.; Kamiyama, T.; Kato, Y.; Hama, S.; Kawamoto, K.; Mitsui, A. A Lithium Superionic Conductor. *Nat. Mater.* **2011**, *10*, 682–686.
- (99) Murugan, R.; Thangadurai, V.; Weppner, W. Fast Lithium Ion Conduction in Garnet-Type Li₇La₃Zr₂O₁₂. *Angew. Chem., Int. Ed.* **2007**, *46*, 7778–7781.
- (100) Li, Y.; Han, J. T.; Wang, C. A.; Vogel, S. C.; Xie, H.; Xu, M.; Goodenough, J. B. Ionic Distribution and Conductivity in Lithium Garnet Li₇La₃Zr₂O₁₂. *J. Power Sources* **2012**, *209*, 278–281.
- (101) Dumon, A.; Huang, M.; Shen, Y.; Nan, C. W. High Li Ion Conductivity in Strontium Doped Li₇La₃Zr₂O₁₂ Garnet. *Solid State Ion.* **2013**, *243*, 36–41.

- (102) Aono, H.; Sugimoto, E.; Sadaoka, Y.; Imanaka, N.; Adachi, G. ya. Ionic Conductivity and Sinterability of Lithium Titanium Phosphate System. *Solid State Ion.* **1990**, *40–41*, 38–42.
- (103) Arbi, K.; Mandal, S.; Rojo, J. M.; Sanz, J. Dependence of Ionic Conductivity on Composition of Fast Ionic Conductors $\text{Li}_{1+x}\text{Ti}_{2-x}\text{Al}_x(\text{PO}_4)_3$, $0 \leq x \leq 0.7$. A Parallel NMR and Electric Impedance Study. *Chem. Mater.* **2002**, *14*, 1091–1097.
- (104) Arbi, K.; Lazarraga, M. G.; Chehimi, D. B. H.; Ayadi-Trabelsi, M.; Rojo, J. M.; Sanz, J. Lithium Mobility in $\text{Li}_{1.2}\text{Ti}_{1.8}\text{R}_{0.2}(\text{PO}_4)_3$ Compounds ($\text{R} = \text{Al, Ga, Sc, In}$) as Followed by NMR and Impedance Spectroscopy. *Chem. Mater.* **2004**, *16*, 255–262.
- (105) Malik, Z. P.; Sologub, O.; Grytsiv, A.; Giester, G.; Rogl, P. F. Crystal Structure of Novel Ni-Zn Borides: First Observation of a Boron-Metal Nested Cage Unit: B_{20}Ni_6 . *Inorg. Chem.* **2011**, *50*, 7669–7675.
- (106) Kuzma, Y. B.; Kripyakevich, P. I.; Bilonizhko, N. S. Crystal Structure of CeCo_3B_2 and Analogous Compounds. *Dopov. Akad. Nauk Ukr. RSR* **1969**, *31*, 939–941.
- (107) Telegus, V. S.; Kuzma, Y. B. X-Ray Investigation of the Rhenium-Manganese-Boron System. *Dopov. Akad. Nauk Ukr. RSR Ser. A* **1969**, *1969*, 945–948.
- (108) Balents, L. Spin Liquids in Frustrated Magnets. *Nature* **2010**, *464*, 199–208.
- (109) Jovanovic, M.; Schoop, L. M. Simple Chemical Rules for Predicting Band Structures of Kagome Materials. *J. Am. Chem. Soc.* **2022**, *144*, 10978–10991.
- (110) Yakel, H. L. Atom Distributions in Tau-Carbide Phases: Fe and Cr Distributions in $(\text{Cr}_{23-x}\text{Fe}_x)\text{C}_6$ with $x = 0, 0.7_4, 1.7_0, 4.1_3$ and 7.3_6 . *Acta Crystallogr.* **1987**, *B43*, 230–238.
- (111) Idzikowski, B.; Szajek, A.; Greneche, J. M.; Kovač, J. Nanogranular $\text{Fe}_x\text{Ni}_{23-x}\text{B}_6$ Phase Formation during Devitrification of Nickel-Rich $\text{Ni}_{64}\text{Fe}_{16}\text{Zr}_7\text{B}_{12}\text{Au}_1$ Amorphous Alloy. *Appl. Phys. Lett.* **2004**, *85*, 1392–1394.
- (112) Hirata, A.; Hirotsu, Y.; Amiya, K.; Nishiyama, N.; Inoue, A. Nanocrystallization of Complex Fe_{23}B_6 -Type Structure in Glassy Fe–Co–B–Si–Nb Alloy. *Intermetallics* **2008**, *16*, 491–497.
- (113) Kapfenberger, C.; Albert, B.; Pöttgen, R.; Huppertz, H. Structure Refinements of Iron Borides Fe_2B and FeB . *Z. Kristallogr. Cryst. Mater.* **2006**, *221*, 477–481.
- (114) Barinov, V. A.; Dorofeev, G. A.; Ovechkin, L. V.; Elsukov, E. P.; Ermakov, A. E. Structure and Magnetic Properties of the α -FeB Phase Obtained by Mechanical Working. *Phys. Status Solidi A* **1991**, *123*, 527–534.
- (115) Kolmogorov, A. N.; Shah, S.; Margine, E. R.; Bialon, A. F.; Hammerschmidt, T.; Drautz, R. New Superconducting and Semiconducting Fe-B Compounds Predicted with an Ab Initio Evolutionary Search. *Phys. Rev. Lett.* **2010**, *105*, No. 217003.
- (116) Jones, M. E.; Marsh, R. E. The Preparation and Structure of Magnesium Boride, MgB_2 . *J. Am. Chem. Soc.* **1954**, *76*, 1434–1436.
- (117) Galy, J.; Guette, A.; Naslain, R. Structure Cristalline de Tetraborure de Magnesium. *C. R. Hebd. Séances Acad. Sci., Ser. C* **1972**, *275*, 41–44.
- (118) Pediaditakis, A.; Schroeder, M.; Sagawe, V.; Ludwig, T.; Hillebrecht, H. Binary Boron-Rich Borides of Magnesium: Single-Crystal Investigations and Properties of MgB_7 and the New Boride $\text{Mg}_{\sim 5}\text{B}_{44}$. *Inorg. Chem.* **2010**, *49*, 10882–10893.
- (119) Ong, S. P.; Richards, W. D.; Jain, A.; Hautier, G.; Kocher, M.; Cholia, S.; Gunter, D.; Chevrier, V. L.; Persson, K. A.; Ceder, G. Python Materials Genomics (Pymatgen): A Robust, Open-Source Python Library for Materials Analysis. *Comput. Mater. Sci.* **2013**, *68*, 314–319.
- (120) Li, R.; Yang, J.; Wang, Y.; Huang, G.; Li, S.; Wang, Z.; Jia, H.; Wang, J.; Pan, F. Interlayer Regulatory Engineering of NiO_2 by Introducing H^+ for High-Rate Mg Ion Storage. *ACS Appl. Energy Mater.* **2024**, *7*, 5811–5821.

Supporting Information

Accelerated Exploration of Empty Material Compositional Space: Mg-Fe-B Ternary Metal Borides

Zhen Zhang^{1,†}, Shiya Chen^{2,†}, Feng Zheng^{3,†}, Vladimir Antropov^{1,4}, Yang Sun^{2,*}, and Kai-Ming Ho¹

¹Department of Physics and Astronomy, Iowa State University, Ames, IA 50011, USA

²Department of Physics, Xiamen University, Xiamen 361005, China

³School of Science, Jimei University, Xiamen, 361021, China

⁴Ames National Laboratory, U.S. Department of Energy, Ames, IA 50011, USA

†Equal contribution

*Email: yangsun@xmu.edu.cn (Yang Sun)

Contents

Figure S1. Simulated single-crystal diffraction with view direction along [001].	S2
Figure S2. Simulated single-crystal diffraction with view direction along [100].	S3
Figure S3. Simulated single-crystal diffraction with view direction along [110].	S4
Figure S4. Comparisons of simulated single-crystal diffraction among the channeled phases. .	S5
Figure S5. Electronic band structures of MgFe ₄ B ₄	S6
Figure S6. Electronic band structures of ZrCo ₃ B ₂ -type MgFe ₃ B ₂	S6
Figure S7. Mean square displacement (MSD) of Mg in the Mg ₂ Fe ₇ B ₇ at 300 K.	S7
Table S1. The proposed structural model Mg ₇ Fe ₂₄ B ₂₄	S8
Table S2. Materials inventory of the 1D channeled structure.	S9
Table S3. Categorization of 1466 ternary borides into 275 structural prototypes.	S10

[001]

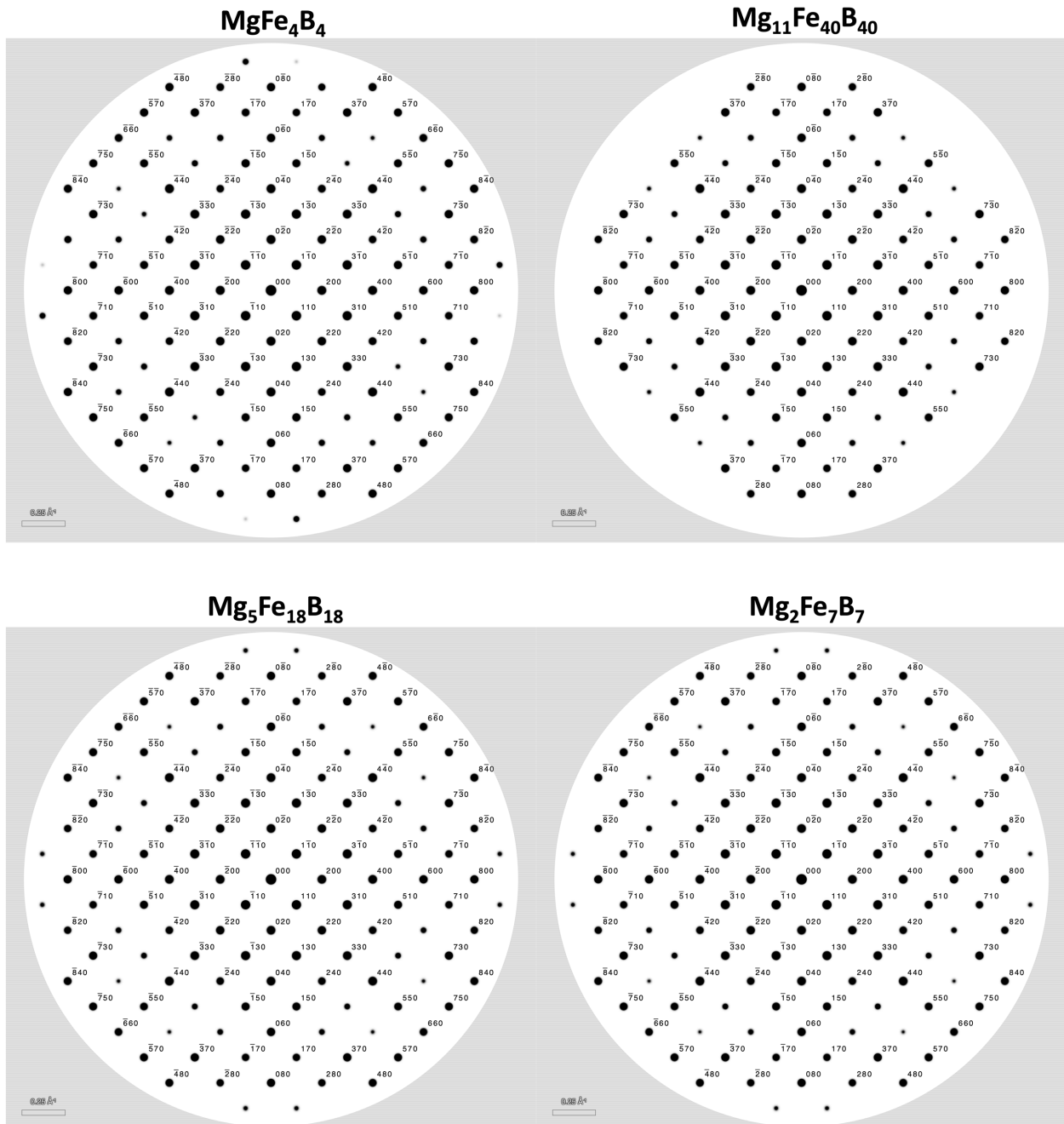


Figure S1. Simulated single-crystal diffraction for MgFe_4B_4 , $\text{Mg}_{11}\text{Fe}_{40}\text{B}_{40}$, $\text{Mg}_5\text{Fe}_{18}\text{B}_{18}$, and $\text{Mg}_2\text{Fe}_7\text{B}_7$. The view direction is along [001]. Instrument: Transmission electron microscopy (TEM) diffraction, $\lambda = 0.037 \text{ \AA}$.

[100]

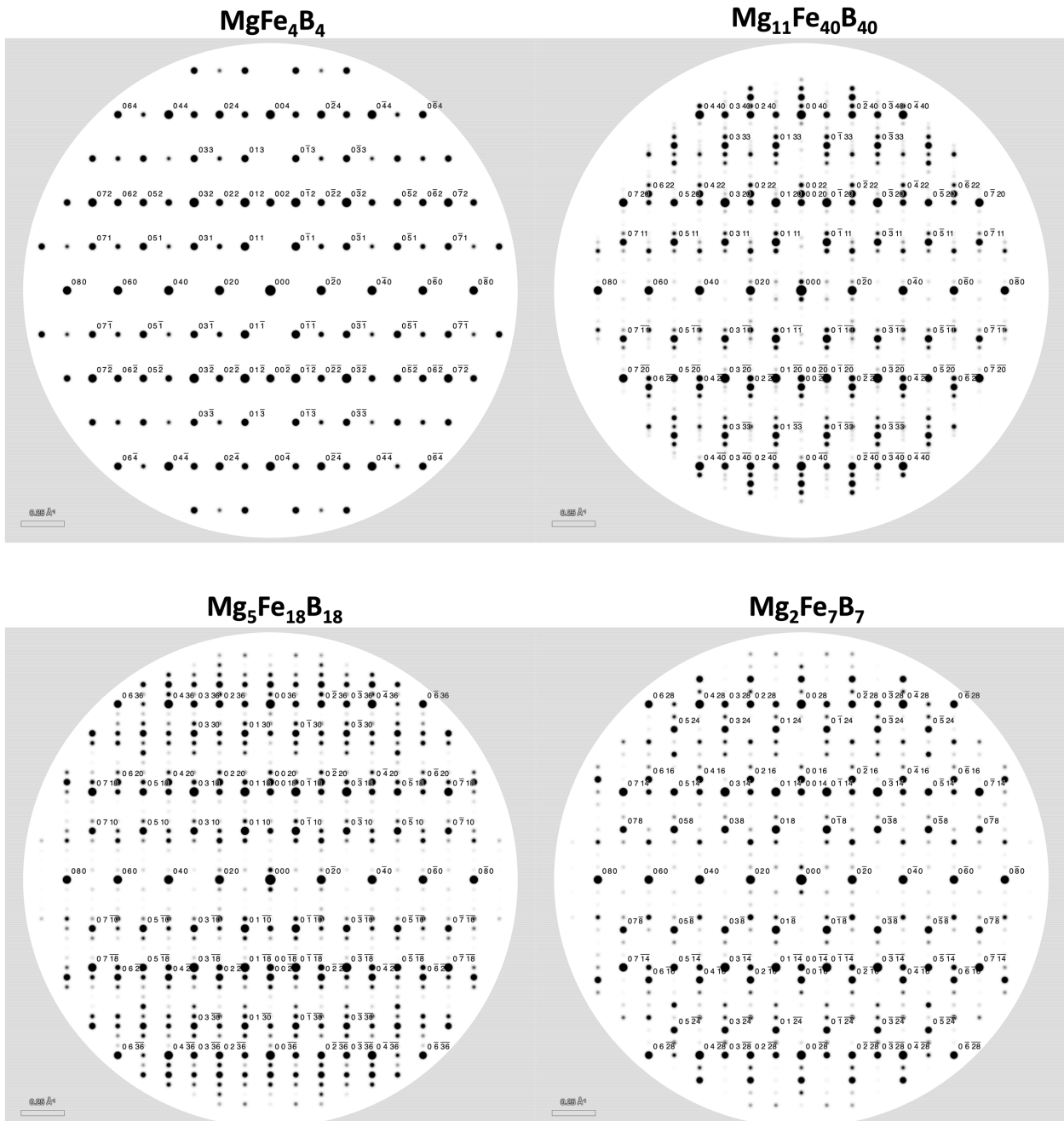


Figure S2. Simulated single-crystal diffraction for MgFe₄B₄, Mg₁₁Fe₄₀B₄₀, Mg₅Fe₁₈B₁₈, and Mg₂Fe₇B₇. The view direction is along [100]. Instrument: Transmission electron microscopy (TEM) diffraction, $\lambda = 0.037 \text{ \AA}$.

[110]

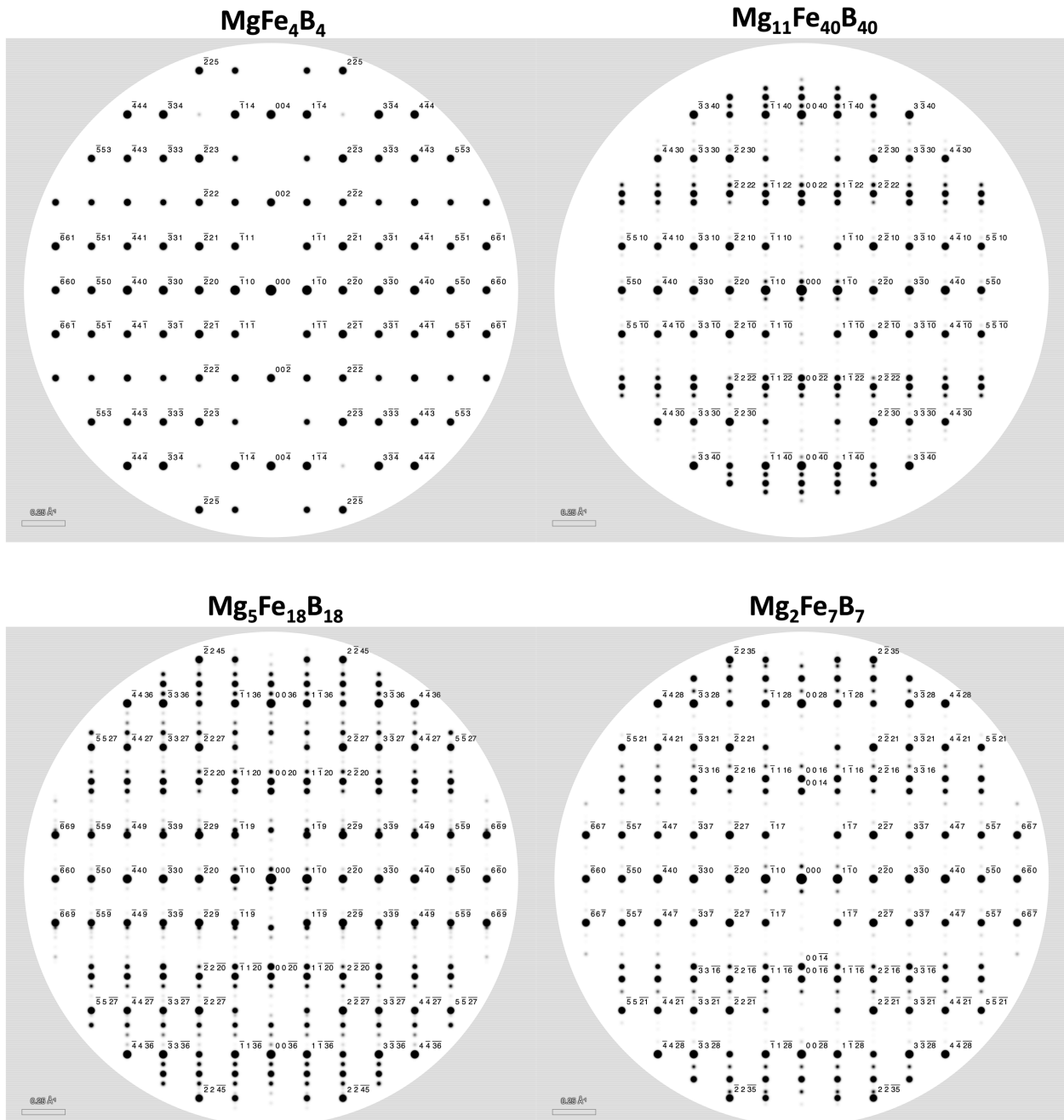


Figure S3. Simulated single-crystal diffraction for MgFe₄B₄, Mg₁₁Fe₄₀B₄₀, Mg₅Fe₁₈B₁₈, and Mg₂Fe₇B₇. The view direction is along [110]. Instrument: Transmission electron microscopy (TEM) diffraction, $\lambda = 0.037 \text{ \AA}$.

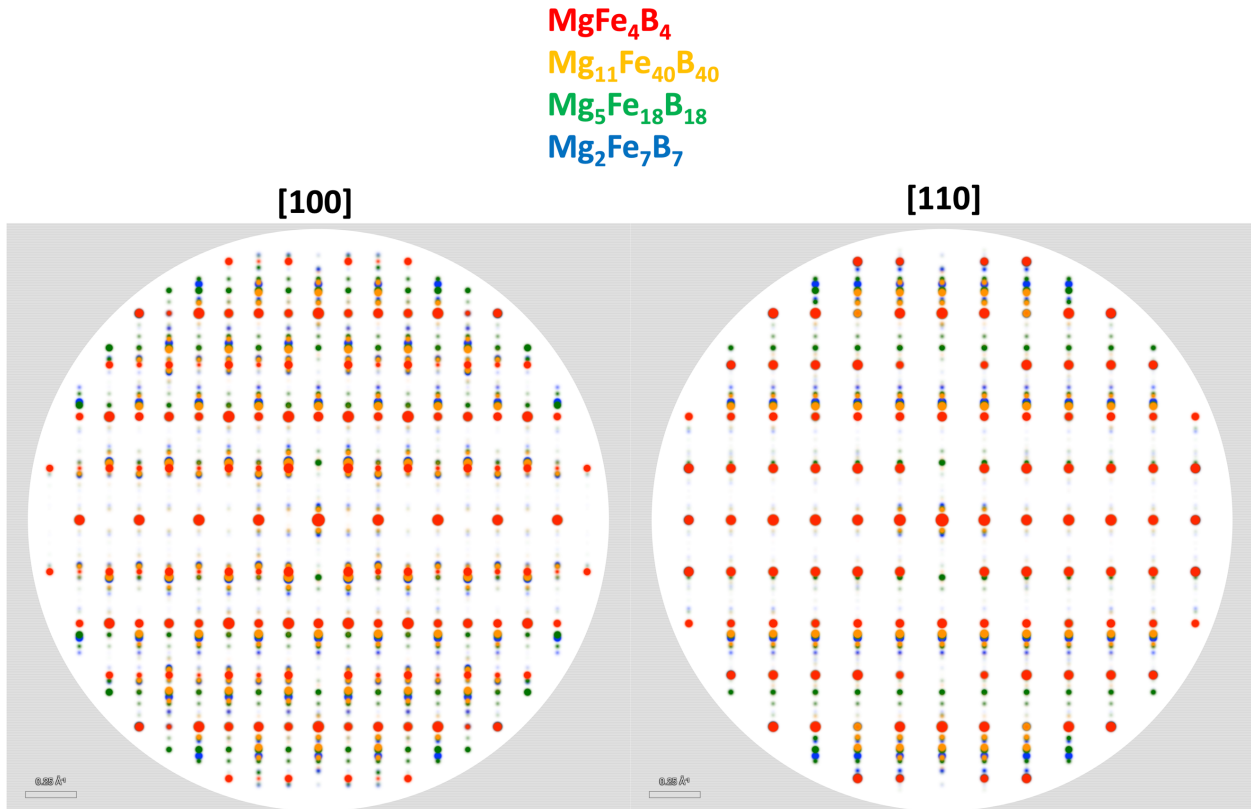


Figure S4. Comparisons of simulated single-crystal diffraction among MgFe_4B_4 (red), $\text{Mg}_{11}\text{Fe}_{40}\text{B}_{40}$ (orange), $\text{Mg}_5\text{Fe}_{18}\text{B}_{18}$ (green), and $\text{Mg}_2\text{Fe}_7\text{B}_7$ (blue). The view directions are along $[100]$ (left) and $[110]$ (right), respectively. Instrument: Transmission electron microscopy (TEM) diffraction, $\lambda = 0.037 \text{ \AA}$.

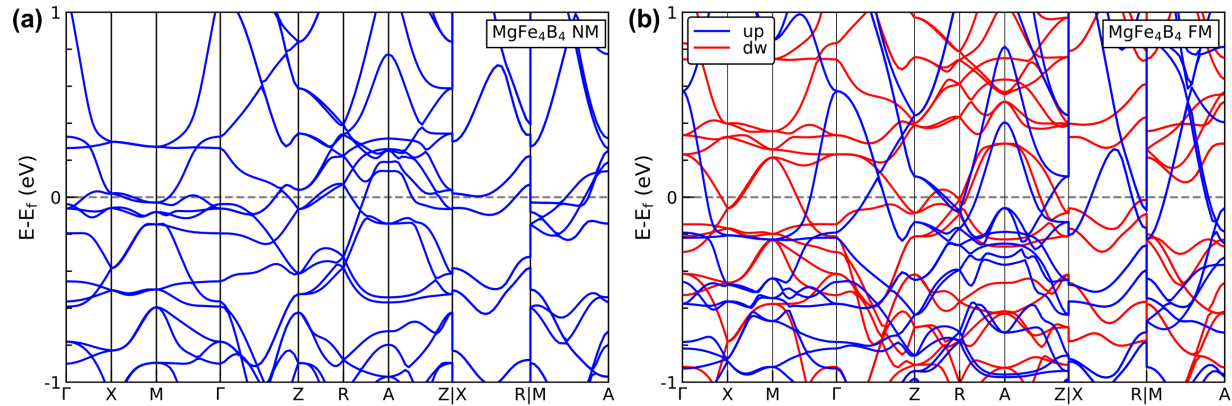


Figure S5. (a) Non-spin-polarized and (b) spin-polarized electronic band structures of MgFe_4B_4 , both of which show metallic nature.

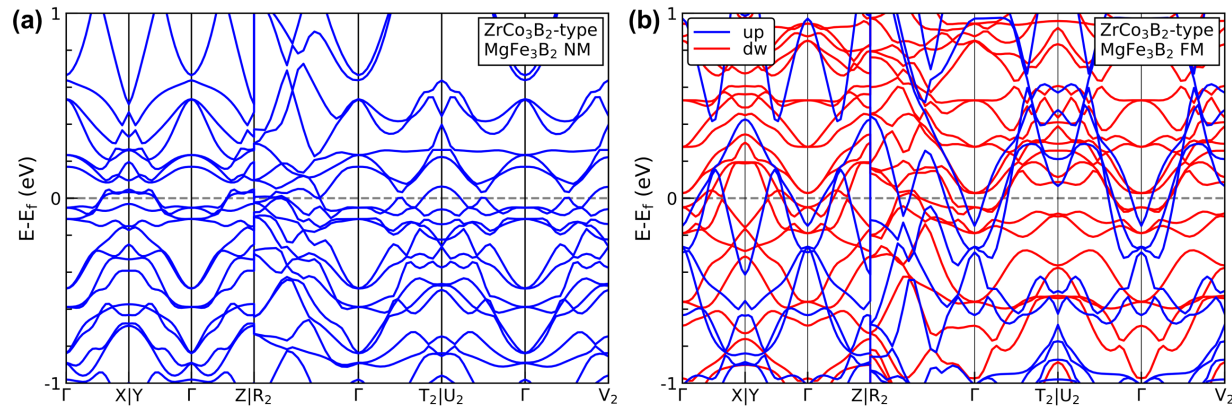


Figure S6. (a) Non-spin-polarized and (b) spin-polarized electronic band structures of ZrCo_3B_2 -type MgFe_3B_2 , both of which show metallic nature.

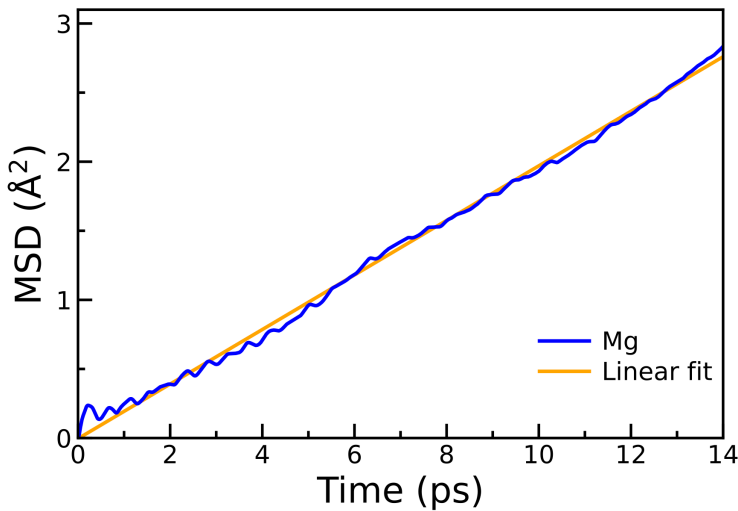


Figure S7. Mean square displacement (MSD) of Mg in the AIMD simulations for the 128-atom $\text{Mg}_2\text{Fe}_7\text{B}_7$ at 300 K (blue) and its linear fit (orange).

Table S1. DFT-relaxed structure in CIF file format for the proposed structural model, Mg₇Fe₂₄B₂₄, in the $P\bar{4}2_1c$ space group.

```
#
# CRYSTAL DATA
#
data_VESTA_phase_1

_chemical_name_common      'Mg7Fe24B24'
_cell_length_a            6.755000
_cell_length_b            6.755000
_cell_length_c            23.528999
_cell_angle_alpha         90.000000
_cell_angle_beta          90.000000
_cell_angle_gamma         90.000000
_cell_volume              1073.628864
_space_group_name_H-M_alt 'P -4 21 c'
_space_group_IT_number    114

loop_
_atom_site_label
_atom_site_occularity
_atom_site_fract_x
_atom_site_fract_y
_atom_site_fract_z
_atom_site_adp_type
_atom_site_U_iso_or_equiv
_atom_site_type_symbol

Mg1   1.0  0.000000  0.000000  0.429280  Uiso ? Mg
Mg2   1.0  0.000000  0.000000  0.286060  Uiso ? Mg
Mg3   1.0  0.000000  0.000000  0.142000  Uiso ? Mg
Mg4   1.0  0.000000  0.000000  0.000000  Uiso ? Mg
Fe1   1.0  0.132110  0.374910  0.146630  Uiso ? Fe
Fe2   1.0  0.130130  0.373360  0.313220  Uiso ? Fe
Fe3   1.0  0.126710  0.369730  0.479990  Uiso ? Fe
Fe4   1.0  0.371650  0.128400  0.103400  Uiso ? Fe
Fe5   1.0  0.374500  0.131480  0.270100  Uiso ? Fe
Fe6   1.0  0.374510  0.131700  0.436660  Uiso ? Fe
B1    1.0  0.175340  0.317250  0.064410  Uiso ? B
B2    1.0  0.176290  0.318340  0.231070  Uiso ? B
B3    1.0  0.179220  0.322180  0.397710  Uiso ? B
B4    1.0  0.323860  0.181240  0.018940  Uiso ? B
B5    1.0  0.320180  0.177530  0.185620  Uiso ? B
B6    1.0  0.317170  0.175490  0.352250  Uiso ? B
```

Table S2. Materials inventory from the Materials Project¹ of the 1D channelled structure shown in Fig. 2 of the main text, most of which involve rare earths.

Compounds	Materials Project ID
$\text{Y}(\text{BIr})_4$	mp-981396
$\text{La}(\text{CoB})_4$	mp-1189727
$\text{La}(\text{BRu})_4$	mp-7347
$\text{La}(\text{BOs})_4$	mp-1188221
$\text{La}(\text{BIr})_4$	mp-9596
$\text{Ce}(\text{FeB})_4$	mp-1006322
$\text{Ce}(\text{BOs})_4$	mp-1188930
$\text{Ce}(\text{BIr})_4$	mp-1190481
$\text{Pr}(\text{FeB})_4$	mp-1188734
$\text{Pr}(\text{CoB})_4$	mp-975663
$\text{Pr}(\text{BOs})_4$	mp-1188588
$\text{Pr}(\text{BIr})_4$	mp-1189206
$\text{Nd}(\text{FeB})_4$	mp-1106404
$\text{Nd}_5(\text{FeB})_{18}$	mp-650968
$\text{Nd}(\text{CoB})_4$	mp-581471
$\text{Nd}(\text{BOs})_4$	mp-15323
$\text{Nd}(\text{BIr})_4$	mp-9584
$\text{Sm}(\text{CoB})_4$	mp-1105839
$\text{Sm}_{11}(\text{CoB})_{40}$	mp-649331
$\text{Sm}(\text{BOs})_4$	mp-1189226
$\text{Sm}(\text{BIr})_4$	mp-1188143
$\text{Eu}(\text{BOs})_4$	mp-1189309
$\text{Eu}(\text{BIr})_4$	mp-20578
$\text{Gd}_2(\text{FeB})_7$	mp-680207
$\text{Gd}(\text{BIr})_4$	mp-1106191
$\text{Tb}(\text{BIr})_4$	mp-978921
$\text{Th}(\text{BOs})_4$	mp-1179056
$\text{Th}(\text{BIr})_4$	mp-1106302
$\text{Pu}(\text{BIr})_4$	mp-1188783

Table S3. Categorization of 1466 ternary borides from the Materials Project¹ into 275 structural prototypes. By convention, prototypes are the most well-known crystal structures or structural types used in materials databases such as ICSD² and OQMD³. However, many structural types are not well-known, and the prototype names can vary. The purpose of this table is to inform researchers of all known compounds of the same structural type. Within each structural type, using any one of the structures to do elemental substitutions, run DFT calculations, and explore unexplored ternary phase diagrams is equivalent. The DFT relaxed structures can then be used for structural refinements with respect to the measurements. The chemical formulas in this table are in accord with those in the Materials Project. If one is not sure about the chemical formulas that the Materials Project uses, simply go to its website (<https://next-gen.materialsproject.org/materials>) and use the search box, which accepts free format.

No. of structural prototypes	Compounds [Materials Project ID]
1	YHgB [mp-1100402] BeGeB [mp-631541] ZrAgB [mp-961701] CrCuB [mp-1100441] MgScB [mp-1100394] SiBPb [mp-631526] HfAgB [mp-1100399] AlAgB [mp-631568] LiSnB [mp-1100396] YCdB [mp-1100401] BeReB [mp-631537] MgBeB [mp-1221963] LaReB [mp-631508] AlInB [mp-631543] BaSiB [mp-631544] NiBTe [mp-631540] TiCuB [mp-1100413] BaTaB [mp-631570] CaBiB [mp-631550] NbBW [mp-631531] BeAlB [mp-4262] ZrCuB [mp-1100435] LiSiB [mp-1100392] SrBiB [mp-631552] NiBiB [mp-631538] BiBTe [mp-631511] SiBAu [mp-631562] ZrBTe [mp-631518]
2	LaBPt ₄ [mp-1211262] LuFe ₄ B [mp-1101759] TmNi ₄ B [mp-10129] DyNi ₄ B [mp-1102346] ErFe ₄ B [mp-3045] GdCo ₄ B [mp-13268] CeCo ₄ B [mp-21878] PrNi ₄ B [mp-1101772] TmCo ₄ B [mp-1102752] TbNi ₄ B [mp-12964] EuNi ₄ B [mp-1103796] LaNi ₄ B [mp-4634] SmNi ₄ B [mp-1102220] GdFe ₄ B [mp-1102349] UCo ₄ B [mp-1103581] SmCo ₄ B [mp-1102597] ErNi ₄ B [mp-12965] EuBPt ₄ [mp-1103637] DyCo ₄ B [mp-1103593] YNi ₄ B [mp-7559] LaCo ₄ B [mp-1095566] CeNi ₄ B [mp-1095459] ErCo ₄ B [mp-1103089] NdNi ₄ B [mp-8048] YCo ₄ B [mp-10463] PrBPt ₄ [mp-13483] CaNi ₄ B [mp-8307] PrCo ₄ B [mp-11610] NdCo ₄ B [mp-3689] TbCo ₄ B [mp-1102265] HoCo ₄ B [mp-1103652] GdNi ₄ B [mp-1102948] LuNi ₄ B [mp-1101842] TmFe ₄ B [mp-1102205] LuCo ₄ B [mp-1210782] HoNi ₄ B [mp-10398] UFe ₄ B [mp-1207921] CeBPt ₄ [mp-20051] NdBPt ₄ [mp-1209829]

	Mg ₁₄ CuB [mp-1026874] Mg ₁₄ AlB [mp-1028227] Mg ₁₄ FeB [mp-1027782] YMg ₁₄ B [mp-1027937] LaMg ₁₄ B [mp-1026743] KMg ₁₄ B [mp-1026827] Mg ₁₄ SiB [mp-1026687] CsMg ₁₄ B [mp-1026562] Mg ₁₄ ZrB [mp-1027866] Mg ₁₄ TiB [mp-1026386] Mg ₁₄ ZnB [mp-1027886] Mg ₁₄ SnB [mp-1026588] HfMg ₁₄ B [mp-1026427] SrMg ₁₄ B [mp-1026560] Mg ₁₄ CrB [mp-1026505] CeMg ₁₄ B [mp-1026810] Mg ₁₄ NbB [mp-1026514] CaMg ₁₄ B [mp-1028118] Mg ₁₄ BMo [mp-1026474] Mg ₁₄ GaB [mp-1026430] Mg ₁₄ VB [mp-1028283] Mg ₁₄ CoB [mp-1028392] RbMg ₁₄ B [mp-1026624] Mg ₁₄ MnB [mp-1028067] BaMg ₁₄ B [mp-1026509] Mg ₁₄ CdB [mp-1026485] Mg ₁₄ BW [mp-1026451] Mg ₁₄ BiB [mp-1026431] Mg ₁₄ NiB [mp-1028348] LiMg ₁₄ B [mp-1026801] NaMg ₁₄ B [mp-1026657] Mg ₁₄ BSb [mp-1026429]
3	ZrBeB [mp-1215258] TiBeB [mp-1217018] NbFeB [mp-7705] TaBeB [mp-1217960]
4	LiMg ₆ B [mp-1021306] Mg ₆ FeB [mp-1022325] Mg ₆ NbB [mp-1016585] Mg ₆ ZrB [mp-1022468] Mg ₆ BW [mp-1017057] Mg ₆ TiB [mp-1021319] Mg ₆ BMo [mp-1016648] Mg ₆ TiB [mp-1021314] Mg ₆ NbB [mp-1016598] HfMg ₆ B [mp-1017247] Mg ₆ BSb [mp-1017263] Mg ₆ CuB [mp-1022085] Mg ₆ CrB [mp-1016662] KMg ₆ B [mp-1021406] YMg ₆ B [mp-1022631] Mg ₆ CdB [mp-1017053] Mg ₆ BW [mp-1017056] KMg ₆ B [mp-1021467] Mg ₆ NiB [mp-1021796] NaMg ₆ B [mp-1017341] Mg ₆ VB [mp-1021696] Mg ₆ CoB [mp-1022088] HfMg ₆ B [mp-1017272] Mg ₆ MnB [mp-1022889] Mg ₆ BiB [mp-1017258] Mg ₆ SnB [mp-1021448] CsMg ₆ B [mp-1016422] LiMg ₆ B [mp-1021285] Mg ₆ FeB [mp-1022181] Mg ₆ AlB [mp-1023310] YMg ₆ B [mp-1022629] Mg ₆ MnB [mp-1022952] Mg ₆ CrB [mp-1016621] Mg ₆ CoB [mp-1022057] Mg ₆ BMo [mp-1016669] Mg ₆ AlB [mp-1023279]
5	Tb ₅ Ge ₃ B [mp-1190063] Nb ₅ Ge ₃ B [mp-1105818] Dy ₅ Si ₃ B [mp-13237] Dy ₅ Ge ₃ B [mp-1181755] Zr ₅ Sn ₃ B [mp-1188408] Ta ₅ Ge ₃ B [mp-1189895] Er ₅ Si ₃ B [mp-1213244] La ₅ BPb ₃ [mp-1105575] V ₅ Si ₃ B [mp-1188823] Lu ₅ Si ₃ B [mp-13234] V ₅ Ge ₃ B [mp-1106398] Nb ₅ Si ₃ B [mp-1106165] Nd ₅ Si ₃ B [mp-1209928] Tb ₅ Si ₃ B [mp-1189409] Ta ₅ Ga ₃ B [mp-1208348] Cr ₅ Si ₃ B [mp-1189692] Ho ₅ Si ₃ B [mp-13235]
6	LaBPt ₂ [mp-31052] LuBPt ₂ [mp-1095320] YBPt ₂ [mp-5971] PrBPt ₂ [mp-1209526] TmBPt ₂ [mp-1103146] CeBPt ₂ [mp-10468] NdBPt ₂ [mp-569341]
7	YBPd ₃ [mp-1018643] PrBPd ₃ [mp-2976] LaBRh ₃ [mp-3088] TmBPd ₃ [mp-10134] Sc ₃ InB [mp-19726] ErBPd ₃ [mp-10061] HoBPd ₃ [mp-3693] CeBRh ₃ [mp-510376] Sc ₃ BPb [mp-10133] AlFe ₃ B [mp-1206715] TmBRh ₃ [mp-5438] DyBRh ₃ [mp-3183] ScBRh ₃ [mp-569875] HfBRh ₃ [mp-1017578] LaBPd ₃ [mp-3846] Sc ₃ TlB [mp-10140] YBPt ₃ [mp-1018644] HoBRh ₃ [mp-3710] TbBRh ₃ [mp-3869] GdBRh ₃ [mp-19840]

	EuBPd ₃ [mp-20040] DyBPd ₃ [mp-10060] ScBIr ₃ [mp-10113] SmBRh ₃ [mp-4982] ZrBRh ₃ [mp-1068661] UBRh ₃ [mp-1069774] YBRh ₃ [mp-29725] ThBRh ₃ [mp-1206772] LaBPt ₃ [mp-1018633] CaBPd ₃ [mp-1206909] GdBPD ₃ [mp-20967] CeBPd ₃ [mp-19948] MgNi ₃ B [mp-1206415] ScBPd ₃ [mp-1017631] La ₃ InB [mp-20590] EuBRh ₃ [mp-510377] NbBRh ₃ [mp-1206988] ZrBRh ₃ [mp-1207063] PrBRh ₃ [mp-5200] Sc ₃ SnB [mp-10139] LuBPd ₃ [mp-3105] NdBRh ₃ [mp-3591] LuBRh ₃ [mp-3717] NdBPd ₃ [mp-10120] ScBPt ₃ [mp-1018627] TbBPd ₃ [mp-3022] ErBRh ₃ [mp-3769] SmBPd ₃ [mp-3428]
9	LaMg ₆ B [mp-1099318] CeMg ₆ B [mp-1098076] BaMg ₆ B [mp-1016576] Mg ₆ GaB [mp-1098205] Mg ₆ SiB [mp-1017377] Mg ₆ BSb [mp-1100151] LaMg ₆ B [mp-1099317] SrMg ₆ B [mp-1016334] CsMg ₆ B [mp-1016304] Mg ₆ ZnB [mp-1022672] CaMg ₆ B [mp-1023215] SrMg ₆ B [mp-1016337] Mg ₆ CuB [mp-1022116] Mg ₆ NiB [mp-1099294] CaMg ₆ B [mp-1023213] RbMg ₆ B [mp-1017387] Mg ₆ GaB [mp-1017241] Mg ₆ SnB [mp-1099300] Mg ₆ SiB [mp-1017427] RbMg ₆ B [mp-1100164] Mg ₆ VB [mp-1021779] Mg ₆ BiB [mp-1017230] Mg ₆ ZrB [mp-1022493] Mg ₆ CdB [mp-1100160] CeMg ₆ B [mp-1017491] Mg ₆ ZnB [mp-1022656] BaMg ₆ B [mp-1016647]
10	In ₂ ReB [mp-631547] In ₂ GeB [mp-631527] Sn ₂ BSe [mp-631557] Ga ₂ BSb [mp-631553] KBIr ₂ [mp-631536] BTe ₂ As [mp-631524]
11	ZnBSe ₂ [mp-631528] BaGe ₂ B [mp-631556] Tl ₁ BiTe ₂ [mp-631520] Y ₂ FeB [mp-631661] Hf ₂ BiB [mp-631558] KHg ₂ B [mp-631525] MgBe ₂ B [mp-631564] AlB ₂ Pb [mp-631514] HfGeB ₂ [mp-631549]
12	Zr ₉ BW ₄ [mp-1445845]
13	Mg ₁₄ CdB [mp-1026566] CsMg ₁₄ B [mp-1026611] Mg ₁₄ BMo [mp-1026484] HfMg ₁₄ B [mp-1026463] LiMg ₁₄ B [mp-1026806] Mg ₁₄ SiB [mp-1026711] Mg ₁₄ BSb [mp-1026462] Mg ₁₄ BW [mp-1026491] KMg ₁₄ B [mp-1026871] NaMg ₁₄ B [mp-1099094] Mg ₁₄ CoB [mp-1028436] Mg ₁₄ MnB [mp-1028127] Mg ₁₄ NbB [mp-1026525] Mg ₁₄ GaB [mp-1026500] Mg ₁₄ SnB [mp-1026690] Mg ₁₄ FeB [mp-1028228] CaMg ₁₄ B [mp-1028149] LaMg ₁₄ B [mp-1026772] Mg ₁₄ CrB [mp-1026516] Mg ₁₄ TiB [mp-1026415] YMg ₁₄ B [mp-1027987] SrMg ₁₄ B [mp-1026709] Mg ₁₄ CuB [mp-1026902] CeMg ₁₄ B [mp-1027162] BaMg ₁₄ B [mp-1026603] Mg ₁₄ AlB [mp-1028230] Mg ₁₄ BiB [mp-1026519] Mg ₁₄ ZrB [mp-1099082] RbMg ₁₄ B [mp-1026664] Mg ₁₄ ZnB [mp-1027954] Mg ₁₄ VB [mp-1028307] Mg ₁₄ NiB [mp-1028354]
14	Eu ₄ BPd ₁₂ [mp-1225374]
15	FeBW [mp-1103093] CoBW [mp-22759] CoBMo [mp-21347] CoReB [mp-21464]
16	LaNi ₃ B [mp-1203921] LaNi ₃ B [mp-1201689]

17	Rb ₃ BAs ₂ [mp-9718] K ₃ BAs ₂ [mp-9665] Cs ₃ BAs ₂ [mp-573658]
18	Zr ₉ Re ₄ B [mp-1193442] Hf ₉ Re ₄ B [mp-1193562] Hf ₉ BW ₄ [mp-1212438] Zr ₉ BW ₄ [mp-1192767] Hf ₉ BMo ₄ [mp-18024] Zr ₉ BMo ₄ [mp-1192463] Hf ₉ BOs ₄ [mp-1193665]
19	TaFeB [mp-1080089] NbFeB [mp-1205377] NbFeB [mp-1080817]
20	Er ₂ BPt ₆ [mp-1225050] Hf ₂ Blr ₆ [mp-1223830] Er ₂ BPD ₆ [mp-1225046] Eu ₂ BPD ₆ [mp-1225365] Zr ₂ Blr ₆ [mp-1215493] Ce ₂ BPD ₆ [mp-1226779]
21	TaNiB [mp-1076987] NbNiB [mp-9985] AlBW [mp-1070916] AlBMo [mp-7574]
22	ReBMo [mp-1219525] ReBW [mp-1219534] MnFeB [mp-1221654] CrBW [mp-1226225] MnCoB [mp-1221661] BMoW [mp-1228637] FeReB [mp-1224854] FeNiB [mp-1224960] FeCoB [mp-1224984] CrCoB [mp-1226217]
23	Ti ₂ BRh ₆ [mp-571126] Zr ₂ Blr ₆ [mp-1078623]
24	LiBeB [mp-1102755]
25	Fe ₂ NiB [mp-1105860] FeCo ₂ B [mp-1188282] DyB ₂ Ru [mp-1189977] PuB ₂ Ru [mp-1189387] ErB ₂ Ru [mp-1181423] YB ₂ Os [mp-1106229] LuB ₂ Ru [mp-29239] ScB ₂ Os [mp-1189073] NbNiB ₂ [mp-1188857] HoB ₂ Os [mp-1189925] PuB ₂ Os [mp-1188931] GdB ₂ Os [mp-1188331] TbB ₂ Os [mp-1189495] TbB ₂ Ru [mp-1188601] TmB ₂ Ru [mp-1188615] TaCoB ₂ [mp-1189690] TaNiB ₂ [mp-22709] CeB ₂ Ru [mp-1188136] TmB ₂ Os [mp-1188249] HoB ₂ Ru [mp-1181033] ErB ₂ Os [mp-1189333] LuB ₂ Os [mp-1189270] YB ₂ Ru [mp-1188195] DyB ₂ Os [mp-1189918] PuReB ₂ [mp-1106002] NbCoB ₂ [mp-20877] PuTcB ₂ [mp-1188688]
26	Th ₂ Fe ₁₄ B [mp-1198402] Gd ₂ Fe ₁₄ B [mp-1198327] Dy ₂ Fe ₁₄ B [mp-4023] Nd ₂ Fe ₁₄ B [mp-616958] Nd ₂ Fe ₁₄ B [mp-5182] Ce ₂ Fe ₁₄ B [mp-4459] Pr ₂ Fe ₁₄ B [mp-569428] Sm ₂ Co ₁₄ B [mp-1195895] Er ₂ Fe ₁₄ B [mp-3680] La ₂ Fe ₁₄ B [mp-1198085] Tb ₂ Co ₁₄ B [mp-1196092] Y ₂ Fe ₁₄ B [mp-5434] Sm ₂ Fe ₁₄ B [mp-1196306] Tm ₂ Fe ₁₄ B [mp-5861] Ho ₂ Fe ₁₄ B [mp-14698] Pr ₂ Fe ₁₄ B [mp-683944] Y ₂ Co ₁₄ B [mp-1200125] Tb ₂ Fe ₁₄ B [mp-5759] La ₂ Co ₁₄ B [mp-1197631] Nd ₂ Co ₁₄ B [mp-4164] Pr ₂ Co ₁₄ B [mp-1197003] Lu ₂ Fe ₁₄ B [mp-4214]
27	NbBRu [mp-1105360] TaBRu [mp-1205358]
28	Mg ₈ BPt ₄ [mp-568681] Mg ₈ BRh ₄ [mp-568621]
29	Y ₁₀ Si ₆ B [mp-1216165] Ta ₁₀ Al ₆ B [mp-1217788] V ₁₀ Si ₆ B [mp-1216643]
30	BlrPd [mp-28897] CuBlr [mp-28896]
31	CeBPt ₃ [mp-22435] NdBPt ₃ [mp-11597] PrBPt ₃ [mp-11596]
32	Hf ₂₀ Si ₁₂ B [mp-1224515]

33	Mn ₅ BPd ₁₅ [mp-1221871] Sc ₅ BRh ₁₅ [mp-1219416]
34	BeCo ₂ B [mp-1096558] BeBPt ₂ [mp-1096043] BeBIr ₂ [mp-1095722]
35	NaBPt ₃ [mp-28614]
36	RbBSe ₃ [mp-10552] CsBSe ₃ [mp-573358]
37	YCo ₄ B [mp-1216046] B ₄ MoIr [mp-1228634] B ₄ OsW [mp-1228631] VB ₄ Os [mp-1216395]
38	LiBeB [mp-1018783]
39	Li ₂ BPd ₃ [mp-20657] Li ₂ B ₂ Pt ₃ [mp-20234]
40	Tl ₃ BSe ₃ [mp-28490]
41	Al ₄ Re ₁₂ B [mp-1215160]
42	TaCoB [mp-1193187]
43	TlBSe ₃ [mp-29959]
44	LiBeB [mp-1103047]
45	Ga ₈ BIr ₄ [mp-28924]
46	V ₅ Si ₂ B [mp-1188856] Nb ₅ Ge ₂ B [mp-1189789] Ta ₅ Ge ₂ B [mp-1218007] Fe ₅ Si ₂ B [mp-1188610] SiB ₂ Mo ₅ [mp-4984] Nb ₅ SiB ₂ [mp-1209930] Fe ₅ SiB ₂ [mp-1105372] V ₅ SiB ₂ [mp-10126] Mn ₅ SiB ₂ [mp-1189157] Ta ₅ GeB ₂ [mp-1105309]
47	Fe ₆ SiB [mp-1225187]
48	TaBRu [mp-1195237] NbBOs [mp-1195339]
49	SrBPd ₄ [mp-1191090] BaBPd ₄ [mp-1191182]
50	Si ₂ Ni ₆ B [mp-4720] Ni ₆ Ge ₂ B [mp-1078540] Ti ₆ Ge ₂ B [mp-1080829] Ti ₆ Si ₂ B [mp-11750]
51	U ₄ Be ₅₁ B [mp-1216800]
52	Ta ₄ BT ₈ [mp-505499]
53	LaNi ₃ B [mp-1205795]
54	LiSi ₂ B [mp-1198027]
55	LiBIr [mp-3348]
56	CuBSe ₂ [mp-983565]
57	Fe ₂ NiB [mp-1184343]
58	Zn ₂ BIr ₂ [mp-28787]
59	Al ₂ Re ₃ B [mp-18503]
60	LiBPt ₃ [mp-28613]
61	In ₂ Ni ₇ B [mp-1224457]
62	NdNi ₄ B [mp-680551]

63	MgB _{Ir} [mp-569048]
64	Sn ₄ BRh ₆ [mp-30061]
65	Tb ₃ Ni ₁₃ B ₂ [mp-541883] Nd ₃ Co ₁₃ B ₂ [mp-4603] La ₃ Ni ₁₃ B ₂ [mp-1190121] Pr ₃ Co ₁₃ B ₂ [mp-1209806] Ho ₃ Ni ₁₃ B ₂ [mp-1105707] Y ₃ Ni ₁₃ B ₂ [mp-567863] Pr ₃ Ni ₁₃ B ₂ [mp-1188184] Ce ₃ Ni ₁₃ B ₂ [mp-1106339] Tm ₃ Ni ₁₃ B ₂ [mp-1188278] Er ₃ Ni ₁₃ B ₂ [mp-1188616] Dy ₃ Ni ₁₃ B ₂ [mp-542729] Y ₃ Co ₁₃ B ₂ [mp-1106148] Sm ₃ Ni ₁₃ B ₂ [mp-1189146] Nd ₃ Ni ₁₃ B ₂ [mp-3071]
66	DyB ₂ Ru ₃ [mp-3092] HoCo ₃ B ₂ [mp-5313] LuB ₂ Rh ₃ [mp-1025024] TmB ₂ Ir ₃ [mp-1077393] HfCo ₃ B ₂ [mp-7804] SmB ₂ Ir ₃ [mp-1080381] NdB ₂ Rh ₃ [mp-3055] PrB ₂ Ir ₃ [mp-11594] UB ₂ Os ₃ [mp-10132] UB ₂ Ru ₃ [mp-10137] TbB ₂ Ir ₃ [mp-1025075] EuB ₂ Rh ₃ [mp-21127] PuB ₂ Os ₃ [mp-1077278] ThB ₂ Ir ₃ [mp-10115] GdB ₂ Ru ₃ [mp-22335] ScB ₂ Ir ₃ [mp-1077776] SmB ₂ Ru ₃ [mp-3467] LaB ₂ Ir ₃ [mp-10112] TmB ₂ Ru ₃ [mp-5620] ZrCo ₃ B ₂ [mp-10059] ErCo ₃ B ₂ [mp-5353] TbB ₂ Rh ₃ [mp-1072051] PuB ₂ Ru ₃ [mp-1072629] HoB ₂ Rh ₃ [mp-1025027] UFe ₃ B ₂ [mp-10065] CeB ₂ Ru ₃ [mp-5940] YB ₂ Ir ₃ [mp-31098] UB ₂ Ir ₃ [mp-10116] ErB ₂ Ru ₃ [mp-3093] CeB ₂ Rh ₃ [mp-5757] LaB ₂ Ru ₃ [mp-29723] SmCo ₃ B ₂ [mp-5410] ErB ₂ Rh ₃ [mp-5678] LuB ₂ Ir ₃ [mp-1024990] YCo ₃ B ₂ [mp-5019] LaB ₂ Rh ₃ [mp-3465] CeB ₂ Ir ₃ [mp-11593] YB ₂ Rh ₃ [mp-1024941] LuB ₂ Ru ₃ [mp-5578] GdCo ₃ B ₂ [mp-21252] DyCo ₃ B ₂ [mp-20193] ScCo ₃ B ₂ [mp-4938] LuB ₂ Os ₃ [mp-2880] GdB ₂ Ir ₃ [mp-1077270] PuB ₂ Ir ₃ [mp-1072199] YB ₂ Ru ₃ [mp-4382] NdB ₂ Ru ₃ [mp-7099] TbB ₂ Ru ₃ [mp-3186] PrB ₂ Ru ₃ [mp-5939] DyB ₂ Ir ₃ [mp-1024993] PuB ₂ Rh ₃ [mp-1024968] UCo ₃ B ₂ [mp-10056] TmB ₂ Rh ₃ [mp-1076960] SmB ₂ Rh ₃ [mp-2947] CaB ₂ Rh ₃ [mp-28705] GdB ₂ Rh ₃ [mp-22117] ThB ₂ Ru ₃ [mp-3223] LuCo ₃ B ₂ [mp-15709] TmCo ₃ B ₂ [mp-5714] HoB ₂ Ir ₃ [mp-1072182] NdB ₂ Ir ₃ [mp-1025068] HoB ₂ Ru ₃ [mp-2985] PrB ₂ Rh ₃ [mp-5369] ErB ₂ Ir ₃ [mp-5197] CeCo ₃ B ₂ [mp-4454] TbCo ₃ B ₂ [mp-3040] DyB ₂ Rh ₃ [mp-1025143]
67	Gd(BOs) ₂ [mp-1079837] Dy(BIr) ₂ [mp-1095029] Eu(BIr) ₂ [mp-20976] Ca(BRh) ₂ [mp-8431] Nd(BIr) ₂ [mp-1078948] La(BOs) ₂ [mp-1095136] Tb(BIr) ₂ [mp-1079255] Ce(BRu) ₂ [mp-15588] Nd(BRu) ₂ [mp-1079388] Pr(BIr) ₂ [mp-1080104] Th(BRu) ₂ [mp-1080672] Sm(BRu) ₂ [mp-978771] Gd(BRu) ₂ [mp-1095164] Pr(BRu) ₂ [mp-975729] Th(BOs) ₂ [mp-1079803] Pr(BOs) ₂ [mp-975738] Sr(BRh) ₂ [mp-7348] Y(BIr) ₂ [mp-14622] Sr(BIr) ₂ [mp-6939] Ce(BIr) ₂ [mp-8680] Ce(BOs) ₂ [mp-1080734] Nd(BOs) ₂ [mp-1080515] Sm(BOs) ₂ [mp-978678] Ca(BIr) ₂ [mp-14445] Sm(BIr) ₂ [mp-1079428]

68	Er(FeB) ₂ [mp-3190] La(CoB) ₂ [mp-2967] Dy(FeB) ₂ [mp-568725] Ba(BIr) ₂ [mp-12073] Y(NiB) ₂ [mp-1206929] Nd(CoB) ₂ [mp-5553] Ba(BRh) ₂ [mp-7349] Gd(CoB) ₂ [mp-610530] Y(CoB) ₂ [mp-3515] Lu(FeB) ₂ [mp-12061] Y(FeB) ₂ [mp-12077] Ho(FeB) ₂ [mp-571500] Zn(BIr) ₂ [mp-28786] Tb(CoB) ₂ [mp-3893] Tm(FeB) ₂ [mp-12076] Sm(CoB) ₂ [mp-4073] Ho(CoB) ₂ [mp-573995] Dy(CoB) ₂ [mp-5135] Pr(CoB) ₂ [mp-4322] Tb(FeB) ₂ [mp-12075] Er(CoB) ₂ [mp-568509]
69	Si ₄ Ni ₉ B ₂ [mp-1219289]
70	Nb ₂ B ₂ Mo [mp-1206490] Nb(BMo) ₂ [mp-1079120] Nb ₂ CrB ₂ [mp-1079560] Fe(BW) ₂ [mp-613327] Mn(BMo) ₂ [mp-1092278] Fe(BMo) ₂ [mp-1078299] Cr(BMo) ₂ [mp-1206931] Mn(BW) ₂ [mp-19789] Ta ₂ CrB ₂ [mp-1080757] Ti ₂ ReB ₂ [mp-10136] Ta ₂ FeB ₂ [mp-1095076] Nb ₂ FeB ₂ [mp-1086660] Fe(BMo) ₂ [mp-20278] Ta(BMo) ₂ [mp-1079659]
71	B ₂ Mo ₂ Ru [mp-1190254] B ₂ Mo ₂ Ir [mp-20391] Sr(NiB) ₂ [mp-1238027] B ₂ OsW ₂ [mp-1188234] V ₂ B ₂ Ir [mp-1189371] Ba(NiB) ₂ [mp-1237990] B ₂ Mo ₂ Os [mp-1188450] Cr ₂ B ₂ Ir [mp-1188995]
72	CrFe ₃ B ₂ [mp-1226213]
73	ZnNi ₃ B ₂ [mp-1103182]
74	Co(BW) ₂ [mp-7573] Ni(BW) ₂ [mp-1070761] Ni(BMo) ₂ [mp-9999] Co(BMo) ₂ [mp-1069105] Fe(BW) ₂ [mp-1068296]
75	MnCoB ₂ [mp-1221680] B ₂ RuW [mp-1228657] CrB ₂ Ru [mp-1226273] FeCoB ₂ [mp-1224999] B ₂ MoRu [mp-1228661] VB ₂ Ru [mp-1216407] CrFeB ₂ [mp-1226310] MnReB ₂ [mp-1221600]
76	Pr(BIr) ₂ [mp-1209703] Tb(BIr) ₂ [mp-1208492] Nd(BIr) ₂ [mp-1210266] Sm(BIr) ₂ [mp-1209561] Dy(BIr) ₂ [mp-1213456] La(BIr) ₂ [mp-1211813]
77	Hf ₉ B ₂ W ₃ [mp-1224535] Hf ₉ B ₂ Mo ₃ [mp-1224546]
78	Dy ₃ Ni ₇ B ₂ [mp-18399] Tb ₃ Ni ₇ B ₂ [mp-1191556] Tm ₃ Ni ₇ B ₂ [mp-1005955] Y ₃ Ni ₇ B ₂ [mp-1192116] Gd ₃ Ni ₇ B ₂ [mp-1192940] Lu ₃ Ni ₇ B ₂ [mp-865190] Er ₃ Ni ₇ B ₂ [mp-17168] Sm ₃ Ni ₇ B ₂ [mp-973241] Ho ₃ Ni ₇ B ₂ [mp-1192069] U ₃ Co ₇ B ₂ [mp-505344]
79	Ce ₂ Co ₅ B ₂ [mp-574273] Pr ₂ Co ₅ B ₂ [mp-1200180] Sm ₂ Co ₅ B ₂ [mp-1196408] Nd ₂ Co ₅ B ₂ [mp-1198836]
80	Nd(BRu) ₂ [mp-1212619] Th(BRu) ₂ [mp-1211309] Ho(BRu) ₂ [mp-1213627] U(BRu) ₂ [mp-1208853]
81	Eu ₃ Ni ₇ B ₂ [mp-1225962] Sm ₃ Ni ₇ B ₂ [mp-1219363]

	MnCrB ₂ [mp-1221636] YB ₂ Mo [mp-1215920] VCrB ₂ [mp-1216398] NbB ₂ W [mp-1220349] HfTaB ₂ [mp-1224291] TiB ₂ W [mp-1217023] ZrNbB ₂ [mp-1215223]
82	TaB ₂ Mo [mp-1217965] CrB ₂ W [mp-1226242] HfNbB ₂ [mp-1224347] TiNbB ₂ [mp-1216709] CrB ₂ Mo [mp-1226228] TiB ₂ Mo [mp-1217028]
83	Th(BOs) ₂ [mp-1210637] Tb(BIr) ₂ [mp-1209570]
84	Sc ₃ B ₂ Rh ₅ [mp-542020] Hf ₃ B ₂ Ir ₅ [mp-22409] Sc ₃ B ₂ Ir ₅ [mp-1209011] Ti ₃ Co ₅ B ₂ [mp-504617] Ta ₃ Co ₅ B ₂ [mp-1189575] Nb ₃ Co ₅ B ₂ [mp-1209993] Ta ₃ B ₂ Ru ₅ [mp-1188194] Nb ₃ B ₂ Ru ₅ [mp-1189385] Mg ₃ B ₂ Rh ₅ [mp-1210641]
85	Sn ₅ (BIr ₃) ₂ [mp-28998] Sn ₅ (BRh ₃) ₂ [mp-30060]
86	Mn ₂ AlB ₂ [mp-7892] Al(CrB) ₂ [mp-7692] Al(FeB) ₂ [mp-3805]
87	Rb ₂ B ₂ Se ₇ [mp-16184] K ₂ B ₂ Se ₇ [mp-542637] Na ₂ B ₂ Se ₇ [mp-5004] Tl ₂ B ₂ Se ₇ [mp-16183]
88	Eu ₃ B ₂ Pt ₇ [mp-1102298] Ca ₃ Ni ₇ B ₂ [mp-8308]
89	MgNi ₃ B ₂ [mp-571428]
90	Sr(NiB) ₂ [mp-1189312]
91	Dy(NiB) ₂ [mp-1079900] Y(NiB) ₂ [mp-1079994] Sm(NiB) ₂ [mp-1078891] Ho(NiB) ₂ [mp-31009] Er(NiB) ₂ [mp-1079335] Tb(NiB) ₂ [mp-30333]
92	Sm ₄ (CoB ₂) ₃ [mp-1103681] Pr ₄ (FeB ₂) ₃ [mp-1104305] Tb ₄ (FeB ₂) ₃ [mp-1104685] Y ₄ (FeB ₂) ₃ [mp-1104580] Y ₄ (CoB ₂) ₃ [mp-1104597] Nd ₄ (FeB ₂) ₃ [mp-1104491] Ho ₄ (CoB ₂) ₃ [mp-1103959] Pr ₄ (CoB ₂) ₃ [mp-1105066] Dy ₄ (CoB ₂) ₃ [mp-1104444] Er ₄ (CoB ₂) ₃ [mp-1105098] Sm ₄ (FeB ₂) ₃ [mp-1104274] Ce ₄ (CoB ₂) ₃ [mp-1103972] Ce ₄ (FeB ₂) ₃ [mp-1104452] La ₄ (CoB ₂) ₃ [mp-1104122] Dy ₄ (FeB ₂) ₃ [mp-1105065]
93	Nd ₅ (FeB ₃) ₂ [mp-8793] Ce ₅ (FeB ₃) ₂ [mp-1105171] Pr ₅ (CoB ₃) ₂ [mp-7735] Dy ₅ (CoB ₃) ₂ [mp-1105042] Nd ₅ (MnB ₃) ₂ [mp-1104018]
94	Er(Co ₂ B) ₆ [mp-1188589] La(Co ₂ B) ₆ [mp-1106274] Nd(Fe ₂ B) ₆ [mp-641957] Ba(Ni ₂ B) ₆ [mp-17236] Sr(Ni ₂ B) ₆ [mp-16830] Tb(Ni ₂ B) ₆ [mp-1106328] Tm(Co ₂ B) ₆ [mp-1205300] Pr(Co ₂ B) ₆ [mp-1105562] Nd(Co ₂ B) ₆ [mp-1105815] La(Fe ₂ B) ₆ [mp-1188975] Sm(Co ₂ B) ₆ [mp-1105798] Ho(Co ₂ B) ₆ [mp-1105128] Y(Co ₂ B) ₆ [mp-1188251] Tb(Co ₂ B) ₆ [mp-1188842] Y(Ni ₂ B) ₆ [mp-1106267] Gd(Co ₂ B) ₆ [mp-645286] Eu(Ni ₂ B) ₆ [mp-580731] Gd(Ni ₂ B) ₆ [mp-1106171] Dy(Co ₂ B) ₆ [mp-1106057] Ce(Co ₂ B) ₆ [mp-1205398] Ca(Ni ₂ B) ₆ [mp-21312] Dy(Ni ₂ B) ₆ [mp-1105834]
95	Ga ₂ (Co ₇ B ₂) ₃ [mp-1194289] Hf ₂ (Ni ₇ B ₂) ₃ [mp-1194313] Ni ₂₁ (B ₃ Sb) ₂ [mp-10123] Lu ₂ (Ni ₇ B ₂) ₃ [mp-1193129] In ₂ (Co ₇ B ₂) ₃ [mp-1194164] Ca ₂ (Ni ₇ B ₂) ₃ [mp-1193221] Ta ₂ (Ni ₇ B ₂) ₃ [mp-1192512] Ti ₂ (Co ₇ B ₂) ₃ [mp-1193707] Ni ₂₁ (GeB ₃) ₂ [mp-1209988]

	Nb ₂ (Co ₇ B ₂) ₃ [mp-1192832] Nd ₂ (Fe ₇ B ₂) ₃ [mp-1210236] U ₂ (Fe ₇ B ₂) ₃ [mp-1208129] Ni ₂₁ (SnB ₃) ₂ [mp-21573] Ti ₂ (Ni ₇ B ₂) ₃ [mp-1193180] V ₂ (Co ₇ B ₂) ₃ [mp-1193908] Ce ₂ (Ni ₇ B ₂) ₃ [mp-541851] V ₂ (Ni ₇ B ₂) ₃ [mp-1207902] Mn ₂ (Ni ₇ B ₂) ₃ [mp-1193061] Sc ₂ (Ni ₇ B ₂) ₃ [mp-647205] Cr ₂ (Co ₇ B ₂) ₃ [mp-542727]	Er ₂ (Ni ₇ B ₂) ₃ [mp-1193830] U ₂ (Ni ₇ B ₂) ₃ [mp-10130] Zr ₂ (Ni ₇ B ₂) ₃ [mp-5172] Co ₂₁ (B ₃ W) ₂ [mp-672221] Co ₂₁ (B ₃ Mo) ₂ [mp-542728] Nb ₂ (Ni ₇ B ₂) ₃ [mp-1210179] Mn ₂ (Co ₇ B ₂) ₃ [mp-1194187] Co ₂₁ (ReB ₃) ₂ [mp-541852] In ₂ (Ni ₇ B ₂) ₃ [mp-21551] U ₂ (Co ₇ B ₂) ₃ [mp-541853]	Ga ₂ (Ni ₇ B ₂) ₃ [mp-1193255] Co ₂₁ (SnB ₃) ₂ [mp-542739] Co ₂₁ (GeB ₃) ₂ [mp-1193515] Tm ₂ (Ni ₇ B ₂) ₃ [mp-21608] Ta ₂ (Co ₇ B ₂) ₃ [mp-1193985] Sc ₂ (Co ₇ B ₂) ₃ [mp-1193429] Co ₂₁ (B ₃ Sb) ₂ [mp-505544] Al ₂ (Ni ₇ B ₂) ₃ [mp-1214897] Zr ₂ (Co ₇ B ₂) ₃ [mp-541854] Hf ₂ (Co ₇ B ₂) ₃ [mp-1194066]
96	Pr(Ni ₂ B) ₆ [mp-1201639] Nd(Ni ₂ B) ₆ [mp-1202698] [mp-1204079] Y(Ni ₂ B) ₆ [mp-1202784]	Dy(Ni ₂ B) ₆ [mp-1202380] La(Ni ₂ B) ₆ [mp-14325] Tb(Ni ₂ B) ₆ [mp-10124] Gd(Ni ₂ B) ₆ [mp-21695] Ho(Ni ₂ B) ₆ [mp-1212548] Ce(Ni ₂ B) ₆ [mp-21695]	Sm(Ni ₂ B) ₆ [mp-1205147]
97	Pr ₅ Co ₁₉ B ₆ [mp-542034]	Nd ₅ Co ₁₉ B ₆ [mp-569415]	Lu ₅ Ni ₁₉ B ₆ [mp-8531]
98	Ho ₂ (Ni ₅ B ₂) ₃ [mp-567285]		
99	Ga ₃ (Ni ₁₀ B ₃) ₂ [mp-977324] V ₃ (Ni ₁₀ B ₃) ₂ [mp-1192799] Hf ₃ (Ni ₁₀ B ₃) ₂ [mp-1193581] Nb ₃ (Fe ₁₀ B ₃) ₂ [mp-21666] In ₃ (Co ₁₀ B ₃) ₂ [mp-1193971] Ti ₂₀ (CoB ₂) ₃ [mp-1208329] Al ₃ (Ni ₁₀ B ₃) ₂ [mp-505472] Mg ₃ (Ni ₁₀ B ₃) ₂ [mp-10117]	Ni ₂₀ (SnB ₂) ₃ [mp-29724] Sc ₃ (Ni ₁₀ B ₃) ₂ [mp-1194311] Nb ₃ (Ni ₁₀ B ₃) ₂ [mp-1210153] Zn ₃ (Ni ₁₀ B ₃) ₂ [mp-10131] Fe ₃ (Ni ₁₀ B ₃) ₂ [mp-1193589] Ta ₃ (Ni ₁₀ B ₃) ₂ [mp-1194177] Mn ₃ (Ni ₁₀ B ₃) ₂ [mp-1194237]	Al ₂₀ (CoB ₂) ₃ [mp-1214905] Mn ₃ (Co ₁₀ B ₃) ₂ [mp-1193450] Zr ₃ (Ni ₁₀ B ₃) ₂ [mp-1193952] Al ₃ (Co ₁₀ B ₃) ₂ [mp-505537] Ti ₃ (Ni ₁₀ B ₃) ₂ [mp-1193912] V ₃ (Co ₁₀ B ₃) ₂ [mp-1193521] Ti ₃ (Co ₁₀ B ₃) ₂ [mp-1193476]
100	Tm ₂ (B ₂ Rh ₃) ₃ [mp-1216756] Ho ₂ (B ₂ Rh ₃) ₃ [mp-1224217] Ce ₂ (B ₂ Rh ₃) ₃ [mp-1227070]	Er ₂ (B ₂ Rh ₃) ₃ [mp-1225103] Dy ₂ (B ₂ Rh ₃) ₃ [mp-1225361] Y ₂ (B ₂ Rh ₃) ₃ [mp-1216181]	Lu ₂ (B ₂ Rh ₃) ₃ [mp-1222515] Tb ₂ (B ₂ Rh ₃) ₃ [mp-1217714] La ₂ (B ₂ Rh ₃) ₃ [mp-1223329]
101	Th(CrB ₃) ₂ [mp-9357] [mp-1095025] Ce(CrB ₃) ₂ [mp-2873]	Sm(CrB ₃) ₂ [mp-1079198] Nd(CrB ₃) ₂ [mp-1078775]	U(FeB ₃) ₂ [mp-1087505] Pr(CrB ₃) ₂
102	CrRe ₁₃ B ₆ [mp-1226393]		
103	Lu ₂ (NiB ₂) ₃ [mp-8771] [mp-1102097] Tm ₂ (NiB ₂) ₃ [mp-1102968]	Er ₂ (NiB ₂) ₃ [mp-4071] Ho ₂ (NiB ₂) ₃ [mp-1095435]	Dy ₂ (NiB ₂) ₃ [mp-1103438] Tb ₂ (NiB ₂) ₃
104	Sr ₃ (B ₃ Rh ₄) ₂ [mp-568771] Ca ₃ (B ₃ Rh ₄) ₂ [mp-569257]	La ₃ (B ₃ Ru ₄) ₂ [mp-4676] Y ₃ (B ₃ Os ₄) ₂ [mp-571209]	Eu ₃ (B ₃ Rh ₄) ₂ [mp-672322]

	Gd ₂ B ₆ Os [mp-1202304] Y ₂ ReB ₆ [mp-504560] Pu ₂ B ₆ Os [mp-1205010] Ho ₂ ReB ₆ [mp-1204735] Er ₂ B ₆ Ru [mp-1198465] Pu ₂ ReB ₆ [mp-1201365] Sc ₂ ReB ₆ [mp-1196116] Pu ₂ B ₆ Ru [mp-1201055] Ho ₂ B ₆ Rh [mp-1212391] Dy ₂ B ₆ Ru [mp-1198707] Dy ₂ B ₆ Os [mp-1198294] Lu ₂ B ₆ Rh [mp-1211036] Pu ₂ TcB ₆ [mp-1197233] Er ₂ B ₆ Os [mp-1198965] U ₂ ReB ₆ [mp-1202234] Lu ₂ B ₆ Ru [mp-1201540] Tb ₂ B ₆ Ru [mp-1200192] Ho ₂ B ₆ Os [mp-1200778] Tm ₂ ReB ₆ [mp-1195760] Er ₂ ReB ₆ [mp-1201657] Tb ₂ B ₆ Os [mp-1200538] Sc ₂ B ₆ Rh [mp-569116] U ₂ B ₆ Mo [mp-1195876] Lu ₂ B ₆ Os [mp-1199915] Sc ₂ B ₆ Ir [mp-1209019] Tm ₂ B ₆ Rh [mp-1208020] Sc ₂ CrB ₆ [mp-510306] U ₂ B ₆ W [mp-1203029] Tm ₂ B ₆ Ru [mp-1196973] Y ₂ B ₆ Os [mp-1201886] Lu ₂ ReB ₆ [mp-1201869] Y ₂ B ₆ Ru [mp-1196778] Er ₂ B ₆ Rh [mp-1212905] Tm ₂ B ₆ Os [mp-1203429] Tb ₂ ReB ₆ [mp-1198929] Lu ₂ FeB ₆ [mp-505545] U ₂ B ₆ Os [mp-1202841] Dy ₂ ReB ₆ [mp-1204645] Ho ₂ B ₆ Ru [mp-1198017] Lu ₂ CoB ₆ [mp-505543]
105	Ce ₂ (ReB ₂) ₃ [mp-1190580] Nd ₂ (ReB ₂) ₃ [mp-1190986] Sm ₂ (ReB ₂) ₃ [mp-979418] Pr ₂ (ReB ₂) ₃ [mp-2933]
106	Cr ₉ FeB ₆ [mp-1226337]
107	Nb ₂ AlB ₆ [mp-1220697]
108	Zn ₆ B ₆ Ir ₁₁ [mp-1178665]
109	In(Ni ₁₁ B ₃) ₂ [mp-1224119] Co ₂₂ B ₆ Sb [mp-1194407] In(Co ₁₁ B ₃) ₂ [mp-1194097]
110	Ba ₂ (Ni ₃ B ₂) ₃ [mp-29219]
111	In(Ni ₁₁ B ₃) ₂ [mp-1224500] Fe ₂₂ B ₆ W [mp-1224794]
112	Cr ₂ (NiB ₂) ₃ [mp-1226092]
113	Cr ₃ NiB ₆ [mp-1226349]
114	Zn ₁₅ B ₆ Rh ₁₇ [mp-1215838]
115	LiSiB ₆ [mp-973391]
116	Tb ₃ FeB ₇ [mp-972235] Er ₃ MnB ₇ [mp-1191003] Y ₃ B ₇ W [mp-14373] Tm ₃ B ₇ W [mp-1191016] Er ₃ CrB ₇ [mp-14503] Dy ₃ ReB ₇ [mp-1190970] Dy ₃ FeB ₇ [mp-1192098] Er ₃ FeB ₇ [mp-1190715] Dy ₃ B ₇ W [mp-1191614] Y ₃ ReB ₇ [mp-569002] Gd ₃ B ₇ W [mp-1190670] Y ₃ MnB ₇ [mp-1192224] Ho ₃ MnB ₇ [mp-1191455] Ho ₃ B ₇ Mo [mp-1212287] Gd ₃ ReB ₇ [mp-1190894] Dy ₃ B ₇ Mo [mp-1213062] Tb ₃ B ₇ Mo [mp-1208474] Ho ₃ CrB ₇ [mp-31046] Y ₃ ReB ₇ [mp-7625] Y ₃ FeB ₇ [mp-14542] Er ₃ B ₇ W [mp-1191731] Er ₃ ReB ₇ [mp-1191966] Tm ₃ ReB ₇ [mp-865404] Tb ₃ MnB ₇ [mp-1190660] Tb ₃ B ₇ W [mp-1191743] Ho ₃ ReB ₇ [mp-973395] Ho ₃ B ₇ W [mp-1191254] Ho ₃ FeB ₇ [mp-1192262] Gd ₃ MnB ₇ [mp-976437] Dy ₃ MnB ₇ [mp-14356] Tb ₃ ReB ₇ [mp-972380]
117	

118	TbB ₇ Mo ₃ [mp-1208351] DyB ₇ Mo ₃ [mp-1212893] TmB ₇ Mo ₃ [mp-1208003] YB ₇ Mo ₃ [mp-504874] HoB ₇ Mo ₃ [mp-504877] ErB ₇ Mo ₃ [mp-1213140]
119	Gd ₂ (FeB) ₇ [mp-680207]
120	AlB ₇ Pd ₁₅ [mp-1195438]
121	La ₂ Re ₃ B ₇ [mp-27894]
122	Nb ₃ Co ₄ B ₇ [mp-4212]
123	Al(Ni ₃ B ₂) ₄ [mp-866315] Ga(Ni ₃ B ₂) ₄ [mp-1213377]
124	AlNi ₉ B ₈ [mp-1194505] GaNi ₉ B ₈ [mp-1194536]
125	V ₃ Cr ₃ B ₈ [mp-1216493] Mn ₃ Cr ₃ B ₈ [mp-1221771] Mn ₃ B ₈ Mo ₃ [mp-1221919]
126	Sm ₅ (SiB ₄) ₂ [mp-1208836] Tb ₅ (SiB ₄) ₂ [mp-1208405] Y ₅ (SiB ₄) ₂ [mp-1207750] Ho ₅ (SiB ₄) ₂ [mp-1212227] Dy ₅ (SiB ₄) ₂ [mp-1212823]
127	Zn ₁₁ (B ₄ Rh ₉) ₂ [mp-1207530]
128	V ₁₁ FeB ₈ [mp-1216907] V ₁₁ ReB ₈ [mp-1216792]
129	YUB ₈ [mp-1215753] LuUB ₈ [mp-1222258] CeThB ₈ [mp-1226547] ThUB ₈ [mp-1217340] CeUB ₈ [mp-1226540]
130	Ta ₃ AlB ₈ [mp-1217997]
131	Nb ₇ (B ₄ Ru ₃) ₂ [mp-1191941] Ta ₇ (B ₄ Ru ₃) ₂ [mp-1191981]
132	Sr ₂ B ₈ Ru ₇ [mp-649084]
133	V ₉ Cr ₃ B ₈ [mp-1216445]
134	Rb ₄ (BSe) ₉ [mp-541818] Cs ₄ (BSe) ₉ [mp-1198415]
135	Tm ₂ (Ni ₅ B ₃) ₃ [mp-1203552] Tb ₂ (Ni ₅ B ₃) ₃ [mp-1199398] Ho ₂ (Ni ₅ B ₃) ₃ [mp-5571] Lu ₂ (Ni ₅ B ₃) ₃ [mp-1201139] Y ₂ (Ni ₅ B ₃) ₃ [mp-1204725] Er ₂ (Ni ₅ B ₃) ₃ [mp-1199522] Dy ₂ (Ni ₅ B ₃) ₃ [mp-1198877]
136	Na ₄ (BSe) ₉ [mp-31229]
137	K ₄ (BSe) ₉ [mp-680747]
138	NaB ₉ Se ₈ [mp-640950]
139	K ₄ (BSe) ₉ [mp-1332293]
140	Mg ₄ AlB ₁₀ [mp-1222150]
141	Ho ₂ NiB ₁₀ [mp-1212324] Ce ₂ NiB ₁₀ [mp-21169] Nd ₂ NiB ₁₀ [mp-22471] Pr ₂ NiB ₁₀ [mp-1209651] Gd ₂ NiB ₁₀ [mp-1212642] Y ₂ NiB ₁₀ [mp-1207701] Th ₂ NiB ₁₀ [mp-20109] Th ₂ CoB ₁₀ [mp-22548] Tb ₂ NiB ₁₀ [mp-1208523] Sm ₂ NiB ₁₀ [mp-1208882] Th ₂ FeB ₁₀ [mp-21902] Dy ₂ NiB ₁₀ [mp-1213050]
142	Tb ₃ Ni ₁₉ B ₁₀ [mp-1197368] Ho ₃ Ni ₁₉ B ₁₀ [mp-28151] Y ₃ Ni ₁₉ B ₁₀ [mp-1199550] Dy ₃ Ni ₁₉ B ₁₀ [mp-1197227] Er ₃ Ni ₁₉ B ₁₀ [mp-1201895] Gd ₃ Ni ₁₉ B ₁₀ [mp-866774]

143	Sr ₅ (B ₅ Rh ₇) ₂ [mp-28706]
144	BaLaB ₁₂ [mp-1227841] CeEuB ₁₂ [mp-1226734] LaGdB ₁₂ [mp-1222806] LaSmB ₁₂ [mp-1222763] CeThB ₁₂ [mp-1226486] SrLaB ₁₂ [mp-1218188] LaCeB ₁₂ [mp-1222912] LaEuB ₁₂ [mp-1222902] PrSmB ₁₂ [mp-1219729] CeSmB ₁₂ [mp-1226503] CaSmB ₁₂ [mp-1227050] SrSmB ₁₂ [mp-1217758] EuTmB ₁₂ [mp-1225132] SmYB ₁₂ [mp-1218969] SmGdB ₁₂ [mp-1218985]
145	NdEuB ₁₂ [mp-1220180] SmThB ₁₂ [mp-1218983] SmEuB ₁₂ [mp-1219071] LaCeB ₁₂ [mp-1222899] LaTmB ₁₂ [mp-1222699] LaSmB ₁₂ [mp-1222703] LaEuB ₁₂ [mp-1222891]
146	Ba ₇ (BIr) ₁₂ [mp-27261]
147	Al ₅ Ni ₄₁ B ₁₂ [mp-1228559] Nb ₅ Ni ₄₁ B ₁₂ [mp-1220806]
148	Ce ₈ Re ₁₃ B ₁₂ [mp-1202101]
149	Co ₃ Re ₂₅ B ₁₂ [mp-1226569]
150	Hf(Nb ₂ B ₃) ₄ [mp-1224510]
151	Mg(SiB ₆) ₂ [mp-567224]
152	Sc ₄ B ₁₂ Rh ₁₇ [mp-1200575]
153	Cr ₃ B ₁₂ Rh ₂₅ [mp-1226568]
154	Ni ₄₃ (GeB ₄) ₃ [mp-1220773]
155	Gd ₄ CoB ₁₃ [mp-1198624] Tb ₄ CoB ₁₃ [mp-22573] Tb ₄ NiB ₁₃ [mp-1202802] Ho ₄ NiB ₁₃ [mp-1202173] Y ₄ CoB ₁₃ [mp-504861] Dy ₄ CoB ₁₃ [mp-1200694] Er ₄ CoB ₁₃ [mp-1202869] Lu ₄ NiB ₁₃ [mp-1200891] Tm ₄ NiB ₁₃ [mp-1203068] Dy ₄ NiB ₁₃ [mp-1203435] Ho ₄ CoB ₁₃ [mp-1202390] Tm ₄ CoB ₁₃ [mp-1201455] Y ₄ NiB ₁₃ [mp-1201729] Er ₄ NiB ₁₃ [mp-504627] Lu ₄ CoB ₁₃ [mp-20518] Gd ₄ NiB ₁₃ [mp-1197241]
156	Al ₂ Cu ₁₁ B ₁₃ [mp-1215060]
157	DyAlB ₁₄ [mp-1201129] NaAlB ₁₄ [mp-34763] LiAlB ₁₄ [mp-8204] ErAlB ₁₄ [mp-1198758] HoAlB ₁₄ [mp-569726] TbAlB ₁₄ [mp-1201619] LuAlB ₁₄ [mp-1197767]
158	Ho ₄ NiB ₁₄ [mp-505720]
159	Y ₃ (Fe ₃₁ B ₇) ₂ [mp-28618]
160	Al(Ni ₁₀ B ₇) ₂ [mp-505473]
161	Ga ₃ Ni ₂₇ B ₁₄ [mp-1204832]
162	Ca ₇ (B ₇ Rh ₁₀) ₂ [mp-568511]
163	Zr ₄ (B ₅ Ir ₄) ₃ [mp-1215396]
164	Mg ₁₀ B ₁₆ Ir ₁₉ [mp-568548]
165	Nd ₅ (FeB) ₁₈ [mp-650968]

166	Na ₆ B ₁₈ Se ₁₇ [mp-1220895]
167	Zr ₈ Ni ₆₁ B ₁₈ [mp-1216773]
168	Ba ₂ SrB ₁₈ [mp-1228370]
169	Lu ₄ V ₅ B ₁₈ [mp-1223330]
170	LiMg ₉ B ₂₀ [mp-35040]
171	Zn ₂ Ni ₂₁ B ₂₀ [mp-1197569]
172	Nb ₄ B ₂₀ Mo ₁₁ [mp-1220650]
173	B ₂₀ Ir ₄ W ₅ [mp-1228750]
174	Ba ₃ NaB ₂₄ [mp-1228056] Na ₃ ThB ₂₄ [mp-1221215] La(CeB ₈) ₃ [mp-1223281] Ba ₃ SmB ₂₄ [mp-1228060]
175	ZrUB ₂₄ [mp-1215198]
176	Pr ₁₆ Re ₂₅ B ₂₄ [mp-1220630]
177	La(CeB ₈) ₃ [mp-1223276]
178	U ₅ (B ₁₂ Mo ₅) ₂ [mp-662590]
179	La(SmB ₈) ₃ [mp-1223255]
180	Mg(AlB ₁₄) ₂ [mp-1222257]
181	Mg(AlB ₁₄) ₂ [mp-531611]
182	Ta ₁₁ (Co ₅₂ B ₁₅) ₂ [mp-1217955]
183	Ca(Er ₂ B ₁₅) ₂ [mp-1227415]
184	Sm ₁₁ (CoB) ₄₀ [mp-649331]
185	Li ₄ Mg ₂₃ B ₅₄ [mp-530613]
186	YB ₂ Pd ₇ [mp-13560]
187	Al ₃ (BRu ₂) ₂ [mp-541849]
188	Ba(BSe ₃) ₂ [mp-570823]
189	Ba(NiB) ₂ [mp-1190153]
190	Li ₂ B ₂ Se ₅ [mp-30100]
191	Ta ₂ B ₂ Os [mp-1189186] Nb ₂ B ₂ Os [mp-1106338]
192	Fe ₃ Co ₃ B ₂ [mp-1225207] Fe ₃ Ni ₃ B ₂ [mp-1224887]
193	Cr ₅ SiB ₂ [mp-2647006]
194	Li ₂ B ₂ Rh ₃ [mp-605839]
195	ZrCo ₃ B ₂ [mp-618324] HfCo ₃ B ₂ [mp-1106407]
196	CrRe ₅ B ₂ [mp-1226226]
197	Al ₂ B ₂ Ru ₃ [mp-29674]

198	Ce ₂ B ₂ Ir ₅ [mp-30898]
199	MnRe ₃ B ₂ [mp-1221607]
200	Y(BRu) ₂ [mp-1208918]
201	Cr ₂ B ₂ Ir [mp-569911]
202	Si ₃ B ₃ W ₁₀ [mp-1219326] Nb ₁₀ (SiB) ₃ [mp-1220752]
203	U ₄ (BRu ₄) ₃ [mp-1216857] Pr ₄ (BRh ₄) ₃ [mp-1219901]
204	Cu ₂ B ₃ Ir ₄ [mp-1225826]
205	Zn ₅ B ₃ Ir ₇ [mp-607369] Zn ₅ B ₃ Ir ₇ [mp-1238725] Zn ₅ B ₃ Rh ₇ [mp-510697] Zn ₅ B ₃ Ir ₇ [mp-1179440]
206	Cr ₂ (BW) ₃ [mp-1226102]
207	Pr ₂ Co ₇ B ₃ [mp-3867] Er ₂ Co ₇ B ₃ [mp-1190704] Sm ₂ Co ₇ B ₃ [mp-505207] Ce ₂ Co ₇ B ₃ [mp-504616] Ho ₂ Co ₇ B ₃ [mp-976597] Y ₂ Co ₇ B ₃ [mp-1190692] Tb ₂ Co ₇ B ₃ [mp-1191177] Tm ₂ Co ₇ B ₃ [mp-1190854] Nd ₂ Co ₇ B ₃ [mp-582394] Dy ₂ Co ₇ B ₃ [mp-569158]
208	Mg ₄ B ₃ Ir ₂ [mp-1222183]
209	CeNi ₂ B ₃ [mp-1226793]
210	ErB ₃ Mo [mp-5426] DyB ₃ Mo [mp-1206856] HoB ₃ Mo [mp-1205558]
211	Fe(BRh ₂) ₃ [mp-1225537] Co(BRh ₂) ₃ [mp-1226641]
212	ErNi ₇ B ₃ [mp-31130]
213	Nd ₂ Co ₂₃ B ₃ [mp-1210590] Nd ₂ Fe ₂₃ B ₃ [mp-568158]
214	Ni(BW) ₃ [mp-1104181] Ni(BMo) ₃ [mp-1105036] Co(BW) ₃ [mp-27768] Co(BMo) ₃ [mp-1104546]
215	Ni ₈ Ge ₂ B ₃ [mp-22703]
216	Sn ₄ B ₃ Ir ₇ [mp-28999]
217	Cr ₂ B ₃ Os [mp-1226478]
218	La ₂ (Ni ₂ B) ₃ [mp-1223681]
219	Tl ₃ B ₃ Se ₁₀ [mp-542058] Cs ₃ B ₃ Se ₁₀ [mp-1196535]
220	ZnB ₃ Ir ₄ [mp-579677]
221	Gd ₂ CoB ₃ [mp-1224781]
222	UReB ₃ [mp-28607]
223	Sm ₂ Fe ₁₇ B ₃ [mp-1190200]
224	VCoB ₃ [mp-10057]
225	ErB ₄ Os [mp-1191929] CeFeB ₄ [mp-1213808] SmMnB ₄ [mp-22785] PrMnB ₄ [mp-1191805] TbCoB ₄ [mp-1208336] SmReB ₄ [mp-1208888] DyReB ₄ [mp-1190368] YB ₄ Ru [mp-1190832] UFeB ₄ [mp-1191051] YB ₄ Mo [mp-7691] PuB ₄ Ru [mp-]

	1191620] YCrB ₄ [mp-20450] DyVB ₄ [mp-1191899] HoB ₄ W [mp-976384] ErNiB ₄ [mp-1192068] YB ₄ Os [mp-980205] ErFeB ₄ [mp-1191434] YB ₄ W [mp-1190755] GdFeB ₄ [mp-866656] DyCoB ₄ [mp-1212868] LuB ₄ Ru [mp-1191771] CeReB ₄ [mp-22361] LuNiB ₄ [mp-865491] LuCoB ₄ [mp-1210846] TmNiB ₄ [mp-1190739] LiAlB ₄ [mp-995282] UB ₄ Mo [mp-1187796] CeCrB ₄ [mp-1191927] ScNiB ₄ [mp-21081] PrCrB ₄ [mp-1191933] ScCoB ₄ [mp-1191630] SmFeB ₄ [mp-20416] GdCoB ₄ [mp-21230] DyFeB ₄ [mp-1191987] ErCrB ₄ [mp-985700] YVB ₄ [mp-1191641] ErCoB ₄ [mp-1213100] DyB ₄ Ru [mp-984836] ErB ₄ W [mp-1192093] NdCrB ₄ [mp-1190818] UCoB ₄ [mp-1191070] YFeB ₄ [mp-1207634] HoB ₄ Ru [mp-974392] UCrB ₄ [mp-1191170] HoAlB ₄ [mp-1212096] HoFeB ₄ [mp-1212115] DyB ₄ Rh [mp-1212866] ErVB ₄ [mp-10983] ErAlB ₄ [mp-1213107] NdMnB ₄ [mp-1191986] DyB ₄ W [mp-1192160] TbReB ₄ [mp-1192121] GdCrB ₄ [mp-1190957] LuFeB ₄ [mp-1191710] YReB ₄ [mp-865727] GdB ₄ Ru [mp-1192291] DyMnB ₄ [mp-1190895] PuReB ₄ [mp-1192270] HoMnB ₄ [mp-978098] DyB ₄ Os [mp-1192250] EuB ₄ Ru [mp-1191457] TbB ₄ Mo [mp-1191349] ErMnB ₄ [mp-1190787] SmCrB ₄ [mp-1191882] UB ₄ W [mp-865423] PuB ₄ Os [mp-1191689] TbB ₄ W [mp-1191902] TmCrB ₄ [mp-1191371] TmCoB ₄ [mp-1207976] UMnB ₄ [mp-1190612] ThCrB ₄ [mp-22528] DyCrB ₄ [mp-1191253] GdVB ₄ [mp-1191160] TbVB ₄ [mp-867309] TmAlB ₄ [mp-1191390] TbMnB ₄ [mp-1191670] ScFeB ₄ [mp-1191106] TmB ₄ Ru [mp-971813] TmB ₄ Rh [mp-13343] UReB ₄ [mp-1187853] HoB ₄ Mo [mp-1191115] PuTcB ₄ [mp-1191553] GdB ₄ Os [mp-1191685] ErB ₄ Ru [mp-1191359] HoCoB ₄ [mp-1212117] UVB ₄ [mp-1191272] TbB ₄ Ru [mp-867230] TmFeB ₄ [mp-1207990] HoReB ₄ [mp-975064] DyB ₄ Mo [mp-864993] LuAlB ₄ [mp-8631] PuB ₄ W [mp-1191218] LuB ₄ Rh [mp-1210888] GdB ₄ Mo [mp-1190272] CeMnB ₄ [mp-1213778] TbCrB ₄ [mp-1190703] HoCrB ₄ [mp-1191543] YMnB ₄ [mp-1191988] YB ₄ Rh [mp-13341] GdMnB ₄ [mp-505546] YCoB ₄ [mp-1207600] TmMnB ₄ [mp-1207706] TbFeB ₄ [mp-1208346] LuB ₄ Os [mp-973529] HoB ₄ Rh [mp-1212116] TmB ₄ Os [mp-982777] HoB ₄ Os [mp-1190601] ErB ₄ Rh [mp-13342] GdReB ₄ [mp-1191130] HoVB ₄ [mp-973524] TbB ₄ Os [mp-1192125] ErB ₄ Mo [mp-1190816] ErReB ₄ [mp-1190444] LuCrB ₄ [mp-1190663] PuB ₄ Mo [mp-1190919]		
226	Nd ₂ Ni ₅ B ₄ [mp-31029] La ₂ Ni ₅ B ₄ [mp-3471] Pr ₂ Ni ₅ B ₄ [mp-1102902] Ce ₂ Ni ₅ B ₄ [mp-1095458]		
227	Sr ₂ B ₄ Rh ₅ [mp-8896] Ca ₂ B ₄ Rh ₅ [mp-8895] La ₂ B ₄ Rh ₅ [mp-14696] Eu ₂ B ₄ Rh ₅ [mp-570529]		

	HfTaB ₄ [mp-1224283] HfNbB ₄ [mp-1224328] TiB ₄ Mo [mp-1217026] ZrNbB ₄ [mp-1215211] TaCrB ₄ [mp-1217958] VCrB ₄ [mp-1216375] TaVB ₄ [mp-1217818] ZrB ₄ Mo [mp-1215250] PuNpB ₄ [mp-1219654] CrB ₄ Mo [mp-1226219] MgAlB ₄ [mp-1207086] ZrTaB ₄ [mp-1215209] TaTiB ₄ [mp-1217898] TiNbB ₄ [mp-1216692] TiCrB ₄ [mp-1216966] NbVB ₄ [mp-1220351] ZrTiB ₄ [mp-1215178] TiVB ₄ [mp-1216667] HfTiB ₄ [mp-1224263]
228	Ga ₃ B ₄ Pt ₉ [mp-28869]
229	
230	La(BIr) ₄ [mp-9596] Y(BIr) ₄ [mp-981396] Pr(FeB) ₄ [mp-1188734] Eu(BIr) ₄ [mp-20578] Sm(BOs) ₄ [mp-1189226] Nd(CoB) ₄ [mp-581471] Eu(BOs) ₄ [mp-1189309] Pu(BIr) ₄ [mp-1188783] Nd(FeB) ₄ [mp-1106404] Sm(CoB) ₄ [mp-1105839] Pr(BIr) ₄ [mp-1189206] La(CoB) ₄ [mp-1189727] Nd(BIr) ₄ [mp-9584] Th(BIr) ₄ [mp-1106302] Ce(BOs) ₄ [mp-1188930] Pr(BOs) ₄ [mp-1188588] La(BOs) ₄ [mp-1188221] Ce(FeB) ₄ [mp-1006322] Nd(BOs) ₄ [mp-15323] Tb(BIr) ₄ [mp-978921] Ce(BIr) ₄ [mp-1190481] Th(BOs) ₄ [mp-1179056] Pr(CoB) ₄ [mp-975663] Sm(BIr) ₄ [mp-1188143] Gd(BIr) ₄ [mp-1106191] La(BRu) ₄ [mp-7347]
231	DyB ₄ Rh ₇ [mp-1225334] LaB ₄ Rh ₇ [mp-1223027] SmB ₄ Rh ₇ [mp-1219077] YB ₄ Rh ₇ [mp-1215999] NdB ₄ Rh ₇ [mp-1220226] HoB ₄ Rh ₇ [mp-1223938] ErB ₄ Rh ₇ [mp-1225583]
232	YB ₄ W ₃ [mp-1215950] TaB ₄ W ₃ [mp-1217974] Ta ₃ TiB ₄ [mp-1217975] MnB ₄ W ₃ [mp-1221699] V ₃ ReB ₄ [mp-1216475]
233	VRe ₁₁ B ₄ [mp-1216295]
234	Tm(BIr) ₄ [mp-1178924] Y(ReB) ₄ [mp-1188833] Gd(CoB) ₄ [mp-1181496] La(ReB) ₄ [mp-1106361] Th(BRh) ₄ [mp-1106347] Ce(CoB) ₄ [mp-22165] Nd(BRh) ₄ [mp-973480] Er(BIr) ₄ [mp-1189046] Y(BRh) ₄ [mp-5984] Tb(BRh) ₄ [mp-1178967] Dy(CoB) ₄ [mp-1189595] Sm(BRh) ₄ [mp-978569] Lu(CoB) ₄ [mp-1189538] Pr(BRh) ₄ [mp-1179918] Ce(BRh) ₄ [mp-1106048] Lu(BRh) ₄ [mp-1188110] Er(CoB) ₄ [mp-1189246] U(CoB) ₄ [mp-505343] Tm(CoB) ₄ [mp-1190291] Er(BRh) ₄ [mp-8408] Ho(BRh) ₄ [mp-1189784] Tm(BRh) ₄ [mp-1105638] Ho(CoB) ₄ [mp-1188650] Y(CoB) ₄ [mp-1105964] Tb(CoB) ₄ [mp-1106036] Gd(BRh) ₄ [mp-1106078] Dy(BRh) ₄ [mp-1105740]
235	Nb ₃ Re ₃ B ₄ [mp-1220688] Ta ₃ Re ₃ B ₄ [mp-1218054] Nb ₃ B ₄ W ₃ [mp-1220641] Ta ₃ B ₄ W ₃ [mp-1217992] Cr ₃ B ₄ Mo ₃ [mp-1226327] Mn ₃ B ₄ Mo ₃ [mp-1221842] Ti ₃ B ₄ Mo ₃ [mp-1217082]
236	DyNiB ₄ [mp-1190599] TbNiB ₄ [mp-972467] GdNiB ₄ [mp-865177] UNiB ₄ [mp-972320] ErNiB ₄ [mp-27895] CeNiB ₄ [mp-1191074] NdNiB ₄ [mp-1191368]

	HoNiB ₄ [mp-1192149] SmNiB ₄ [mp-979948] PrNiB ₄ [mp-861608] YNiB ₄ [mp-1190178]
237	Tm(BRh) ₄ [mp-1204414] Er(BRh) ₄ [mp-1200942] Lu(BRh) ₄ [mp-28001]
238	HfZrB ₄ [mp-1224184]
239	Ca ₅ Ni ₁₅ B ₄ [mp-28170]
240	Lu ₃ Co ₁₁ B ₄ [mp-1188111] Er ₃ Co ₁₁ B ₄ [mp-1181434] Sm ₃ Co ₁₁ B ₄ [mp-1189913] Ho ₃ Co ₁₁ B ₄ [mp-1189174] Gd ₃ Co ₁₁ B ₄ [mp-605854] Dy ₃ Co ₁₁ B ₄ [mp-30907] Nd ₃ Co ₁₁ B ₄ [mp-5568] Tm ₃ Co ₁₁ B ₄ [mp-1188803] Pr ₃ Co ₁₁ B ₄ [mp-5457] Tb ₃ Co ₁₁ B ₄ [mp-1188805] Ce ₃ Co ₁₁ B ₄ [mp-13765]
241	U(BRu) ₄ [mp-15355] Y(BRu) ₄ [mp-10138] Pr(BRu) ₄ [mp-1200756] Sc(BRu) ₄ [mp-1200617] Lu(BRh) ₄ [mp-1006099] Pu(BRu) ₄ [mp-1202529] Eu(BRu) ₄ [mp-1199986] U(BOs) ₄ [mp-1196935] Tm(BRu) ₄ [mp-1197448] Er(BRu) ₄ [mp-1196250] Er(BRh) ₄ [mp-14481] Th(BRu) ₄ [mp-1203781] Sm(BRu) ₄ [mp-1199012] Dy(BRu) ₄ [mp-1202990] Tb(BRu) ₄ [mp-1199943] Lu(BRu) ₄ [mp-568184] Ce(BRu) ₄ [mp-1201565] Nd(BRu) ₄ [mp-1198170] Ho(BRu) ₄ [mp-1204787]
242	Fe ₂ B ₄ Mo [mp-15722] Ta(MnB ₂) ₂ [mp-1077930] B ₄ MoRu ₂ [mp-1228655] Mn ₂ B ₄ W [mp-1077988] Co ₂ B ₄ Mo [mp-10055] Mn ₂ B ₄ Mo [mp-1078108]
243	Sr(B ₂ Pt ₃) ₂ [mp-1218890] Ba(B ₂ Pt ₃) ₂ [mp-1228679] Ca(B ₂ Pt ₃) ₂ [mp-1227448]
244	B ₄ MoRu ₂ [mp-1247817]
245	AlCr ₃ B ₄ [mp-637575]
246	Ba ₇ B ₄ Se ₁₃ [mp-583221]
247	MnB ₄ Mo ₃ [mp-1221732] Mn ₃ B ₄ W [mp-1221797] Co ₃ ReB ₄ [mp-1226435] Ti ₃ B ₄ Mo [mp-1217095]
248	ThVB ₄ [mp-1095627] ThB ₄ Mo [mp-5557] PuB ₄ Ru [mp-1101964] UB ₄ W [mp-1103255] UB ₄ Os [mp-1095488] UB ₄ Mo [mp-1103171] ThB ₄ W [mp-1102822] UB ₄ Ru [mp-1103253] ThReB ₄ [mp-1101769] UReB ₄ [mp-1102585] LuAlB ₄ [mp-973540] PuB ₄ Os [mp-1102201]
249	HfTa ₅ B ₄ [mp-1224295]
250	NbB ₄ Mo ₃ [mp-1220383]
251	NaB ₄ Ir ₃ [mp-1220841]
252	Y ₅ B ₄ Rh ₁₅ [mp-1216199] U ₅ B ₄ Rh ₁₅ [mp-1216968] Lu ₅ B ₄ Rh ₁₅ [mp-1222784] La ₅ B ₄ Rh ₁₅ [mp-1223216] Sm ₅ B ₄ Rh ₁₅ [mp-1219166]
253	Sc ₂ B ₄ Oss [mp-1192274] Sc ₂ B ₄ Ru ₅ [mp-1209048] Mg ₂ B ₄ Ru ₅ [mp-541066]
254	ZrB ₄ Ir ₃ [mp-1190085] HfB ₄ Ir ₃ [mp-13861] ScB ₄ Ir ₃ [mp-10114]

255	Co ₂ Re ₅ B ₄ [mp-1226558]
256	MgB ₄ Os ₃ [mp-10503] ScB ₄ Os ₃ [mp-10504]
257	Zn ₅ (BRh ₂) ₄ [mp-569759]
258	In ₅ B ₄ Ir ₉ [mp-570692]
259	CrB ₄ Mo [mp-1226227] HfNbB ₄ [mp-38818]
260	Co ₁₉ (Si ₂ B) ₄ [mp-1226660]
261	Nd ₅ Co ₂₁ B ₄ [mp-505807]
262	CrRe ₃ B ₄ [mp-1226262]
263	Ba ₂ B ₄ Se ₁₃ [mp-30105]
264	Fe(B ₂ Mo) ₂ [mp-1225198]
265	Co ₃ (ReB) ₄ [mp-1213771]
266	ZrScB ₄ [mp-1215212]
267	Fe ₉ B ₄ Ir ₃ [mp-1225266] Fe ₉ B ₄ Rh ₃ [mp-1225075]
268	Y ₂ B ₅ Pd ₁₄ [mp-4597]
269	Cu ₃ B ₅ Pt ₉ [mp-1105186]
270	Ho ₂ (Ni ₂ B) ₅ [mp-568440] Tm ₂ (Ni ₂ B) ₅ [mp-1203887] Tb ₂ (Ni ₂ B) ₅ [mp-1201581] Dy ₂ (Ni ₂ B) ₅ [mp-1204635] Er ₂ (Ni ₂ B) ₅ [mp-1197355]
271	Zn ₆ B ₅ Ir ₁₁ [mp-1215752]
272	Eu ₂ B ₅ Os ₃ [mp-582389] Ca ₂ B ₅ Os ₃ [mp-542455]
273	Na ₃ B ₅ Pt ₉ [mp-505055]
274	Na ₃ B ₅ Se ₉ [mp-531600]
275	B ₅ Ir ₃ W ₂ [mp-1228672]

REFERENCES

- (1) Jain, A.; Ong, S. P.; Hautier, G.; Chen, W.; Richards, W. D.; Dacek, S.; Cholia, S.; Gunter, D.; Skinner, D.; Ceder, G.; Persson, K. A. Commentary: The Materials Project: A Materials Genome Approach to Accelerating Materials Innovation. *APL Mater.* **2013**, *1*, 011002. <https://doi.org/10.1063/1.4812323>.
- (2) Zagorac, D.; Muller, H.; Ruehl, S.; Zagorac, J.; Rehme, S. Recent Developments in the Inorganic Crystal Structure Database: Theoretical Crystal Structure Data and Related Features. *J. Appl. Crystallogr.* **2019**, *52*, 918–925. <https://doi.org/10.1107/S160057671900997X>.
- (3) Kirklin, S.; Saal, J. E.; Meredig, B.; Thompson, A.; Doak, J. W.; Aykol, M.; Rühl, S.; Wolverton, C. The Open Quantum Materials Database (OQMD): Assessing the Accuracy of DFT Formation Energies. *Npj Comput. Mater.* **2015**, *1*, 15010. <https://doi.org/10.1038/npjcompumats.2015.10>.